AERODYNAMIC AND AEROACOUSTIC INVESTIGATION OF SCISSORS TAIL ROTOR CONFIGURATION FOR A UTILITY-CLASS HELICOPTER

A THESIS SUBMITTED TO
THE GRADUATE SCHOOL OF NATURAL AND APPLIED SCIENCES
OF
MIDDLE EAST TECHNICAL UNIVERSITY

BY

MEHMET MELIH ATALAY

IN PARTIAL FULFILLMENT OF THE REQUIREMENTS
FOR
THE DEGREE OF MASTER OF SCIENCE
IN
AEROSPACE ENGINEERING

FEBRUARY 2021

Approval of the thesis:

AERODYNAMIC AND AEROACOUSTIC INVESTIGATION OF SCISSORS TAIL ROTOR CONFIGURATION FOR A UTILITY-CLASS HELICOPTER

submitted by **MEHMET MELIH ATALAY** in partial fulfillment of the requirements for the degree of **Master of Science in Aerospace Engineering Department, Middle East Technical University** by,

Prof. Dr. Halil Kalıpçılar
Dean, Graduate School of **Natural and Applied Sciences** _____

Prof. Dr. İsmail Hakkı Tuncer
Head of Department, **Aerospace Engineering** _____

Prof. Dr. Yusuf Özyörük
Supervisor, **Aerospace Engineering, METU** _____

Examining Committee Members:

Assoc. Prof. Dr. İlkay Yavrucuk
Aerospace Engineering, METU _____

Prof. Dr. Yusuf Özyörük
Aerospace Engineering, METU _____

Assoc. Prof. Dr. Nilay Sezer Uzol
Aerospace Engineering, METU _____

Prof. Dr. Hüseyin Nafiz Alemdaroğlu
School of Civil Aviation, Atılım University _____

Assoc. Prof. Dr. Mustafa Kaya
Aerospace Engineering, Ankara Yıldırım Beyazıt University _____

Date: 04.02.2021

I hereby declare that all information in this document has been obtained and presented in accordance with academic rules and ethical conduct. I also declare that, as required by these rules and conduct, I have fully cited and referenced all material and results that are not original to this work.

Name, Surname: Mehmet Melih Atalay

Signature :

ABSTRACT

AERODYNAMIC AND AEROACOUSTIC INVESTIGATION OF SCISSORS TAIL ROTOR CONFIGURATION FOR A UTILITY-CLASS HELICOPTER

Atalay, Mehmet Melih
M.S., Department of Aerospace Engineering
Supervisor: Prof. Dr. Yusuf Özyörük

February 2021, 108 pages

The noise of the rotorcraft has become nonignorable with their increasing use in daily life. The aerodynamically active components such as the main and tail rotors are the primary sources of noise, and therefore, their evaluation during the design phase must also be carefully included. Pressure variations caused by several aerodynamic mechanisms on the rotor blades are responsible for the generation of the noise, which may be obtained by computational fluid dynamics. Along with rotor locked self pressure fields, the tail rotor being in the main rotor wake and exposed to strongly nonstationary airflow also need attention. Hence, full helicopter modeling is required to have an accurate evaluation on the tail rotor. However, this modeling and solution are costly for computational fluid dynamics. Therefore, an alternative approach for acoustic analysis is developed in this study. Accordingly, the goal of the thesis is to propose a coupling methodology between comprehensive rotorcraft analysis and an aeroacoustic solver, and to implement of the methodology for investigation of scissors tail rotor. Firstly, the comprehensive analysis approach is validated using available required power data and sectional blade airloads. Then, the proposed pres-

sure distribution methodology is implemented to couple comprehensive analysis approach and acoustic solver. A CFD generated airfoil pressure database is used to find pressure distribution over each blade section. Additionally, this coupling is validated using sectional loads and acoustic pressure. Furthermore, aerodynamic and aeroacoustic behavior of the tail rotor are evaluated for isolated and main rotor interacted conventional tail rotor configuration. Finally, effects of vertical distance and scissors angle on aerodynamic and aeroacoustic behavior of the main rotor interacted scissors type tail rotor configuration are investigated. Results indicate that the main rotor wake has a significant impact on the tail rotor at certain flight conditions conditions, and vertical distance and scissors angle changes the oscillatory loads, and there are scissors tail rotor configurations which offers lower noise level than conventional tail rotor.

Keywords: Comprehensive Analysis, Aeroacoustic, Scissors Tail Rotor, Pressure Distribution Methodology

ÖZ

GENEL MAKSAT HELİKOPTERİ İÇİN MAKAS TİPLİ KUYRUK ROTORUNUN AERODİNAMİK VE AEROAKUSTİK İNCELEMESİ

Atalay, Mehmet Melih
Yüksek Lisans, Havacılık ve Uzay Mühendisliği Bölümü
Tez Yöneticisi: Prof. Dr. Yusuf Özyörük

Şubat 2021 , 108 sayfa

Büyüyen helikopter endüstrisi ile birlikte helikopter gürültüsünün gündelik yaşama etkisi göz ardı edilemez hale gelmektedir. Helikopter gürültüsünün ana kaynakları ana ve kuyruk rotorudur ve bu sebeple helikopter tarafından üretilen gürültünün değerlendirmesi tasarım aşamasına dahil edilmelidir. Rotor kanatları üzerindeki çeşitli aerodinamik mekanizmaların neden olduğu basınç değişimleri, hesaplamalı akışkanlar mekaniği ile elde edilebilen, gürültünün oluşumundan sorumludur. Rotorun kendi basınç alanlarının yanı sıra, kuyruk rotorunun ana rotor arka akışında olması ve etkili durağan olmayan hava akışına marız kalması da dikkat gerektirir. Bundan dolayı, kuyruk rotoru üzerinde doğru bir değerlendirme yapmak için tam helikopter modellemesi gereklidir. Bununla birlikte, bu modelleme ve çözüm hesaplamalı akışkanlar dinamiği için maliyetlidir. Dolayısıyla, bu tezin amacı olarak tümleşik döner kanat analizi ile aeroakustik çözücü birleştirilmiş ve bu metoloji makas tipli kuyruk rotorunun incelenmesi için uygulanmıştır. İlk olarak, kapsamlı analiz yaklaşımı mevcut güç verileri ve kanat

kesidi yükleri kullanarak doğrulanmıştır. Bundan sonra, önerilen basınç dağılım metodolojisi kapsamlı analizi yaklaşımını ve aeroakustik çözücüyü birleştirmek için uygulanmıştır ve bu bağlantı mevcut kesitsel yüklerini ve akustik basınçlarını kullanarak doğrulanmıştır. Rotor kanadı üstündeki basınç dağılımını bulmak için HAD analizleri ile elde edilmiş kanat kesidi basınç dağılım veritabanı kullanılmıştır. Ayrıca, geleneksel kuyruk rotorunun aerodinamik ve aeroakustik davranışı izole edilmiş ve ana rotor etkileşimli geleneksel kuyruk rotoru için değerlendirilmiştir. Son olarak, dikey mesafe ve makas açısının ana rotor etkileşimli makas tipli kuyruk rotor konfigürasyonunun aerodinamik ve aeroakustik davranışı üzerindeki etkileri incelenmiştir. Sonuçlar ana rotor arka akışının belirli uçuş koşullarında kuyruk rotoru üzerinde önemli bir etkiye sahip olduğunu, ve dikey mesafe ile makas açısının salınım yükleri değiştirdiğini göstermektedir, ve bazı makas tipi kuyruk rotor konfigürasyonları geleneksel kuyruk rotoruna göre daha düşük gürültü seviyeleri sunmaktadır.

Anahtar Kelimeler: Tümleşik Analiz, Aeroakustik, Makas Tipi Kuyruk Rotoru, Basınç Dağılımı Yöntemi

To my family

ACKNOWLEDGMENTS

The author would like to thank his supervisor, Prof. Dr. Yusuf Özyörük for his guidance, advice, support and valuable feedbacks during the study.

The author is also grateful to Arda Yücekayalı, Murat Şenipek and Harun Tıraş for their helps and feedbacks.

The author would like to acknowledge his coworkers, Pınar Arslan Dülgar, Uğur Kalkan, Fatih Tosun and Yağmur Bulut for their supports.

The author would like to appreciate his mother, father and sister, Gönül, İsmail and Cevşen, for their endless support, faith and lead for finishing this dissertation.

The author would like to thank his company, Turkish Aerospace for supporting and encouraging.

The author is also thankful to Kübra Ünlü, Ozan Akad, Esra Halaçlar and Köksal Mert Danışan for their helps and faiths.

TABLE OF CONTENTS

LIST OF TABLES

TABLES

LIST OF FIGURES

FIGURES

LIST OF ABBREVIATIONS

ABBREVIATIONS

2D	2 Dimensional
3D	3 Dimensional
BVI	Blade Vortex Interaction
CFD	Computational Fluid Dynamics
CHARM	Comprehensive Hierarchical Aeromechanics Rotorcraft Model
CVC	Constant Vorticity Contour
HART	Higher Harmonic Aeroacoustic Rotor Test
HSI	High Speed Impulsive
NoB	Number of Blades
PIV	Particle Image Velocimetry
TACO	Turkish Aerospace Acoustic Code
VLM	Vortex Lattice Method

SYMBOLS

α_s	Shaft tilt angle (Pitch-up positive)
C_T	Thrust Coefficient
C_Q	Power Coefficient
σ	Solidity
r_c	Vortex Core Radius
Γ	Vortex Strength
μ	Advance Ratio
r	Radial Distance
c	Speed of Sound

p'	Pressure Fluctuation
ρ	Density
v_i	Velocity of Surface
u_i	Velocity of Fluid
$\delta(f)$	Dirac Delta Function
δ_{ij}	Kronecker Delta Function
τ_{ij}	Viscous Stress Tensor
$H(f)$	Heaviside Function
T_{ij}	Lighthill Stress Tensor
Ω	Angular Velocity
M_r	Radial Mach Number
T	Thrust
L	Lift Force
N	Normal Force
D	Drag Force
θ	Pitch Angle
ψ	Azimuth Angle
α	Angle of Attack
ϕ	Angle of Velocity Vector
$C_N M^2$	Nondimensional Normal Force
P_L	Loading Acoustic Pressure
P_T	Thickness Acoustic Pressure
P_Tot	Total Acoustic Pressure
P'_{rms}	Root Mean Square of Sound Pressure
P_{ref}	Reference Pressure
δh	Vertical Distance
Δ	Scissors Angle

CHAPTER 1

INTRODUCTION

1.1 Motivation of the Study

Helicopter noise has become a significant problem with the growth of the rotorcraft industry, and increased rotorcraft operations near the public areas day to day. Therefore, several operational restrictions such as frequency of operations, flight path utilization, and types of rotorcraft flow, are imposed. In addition, more stringent noise specifications are imposed to certifications of rotorcraft. Therefore, alternative design and operative configurations on rotorcraft are required to generate a lower noise level.

1.2 Objective of the Study

This study aims to introduce a fast noise calculation methodology for rotorcraft that can be employed in their design phase. The methodology couples comprehensive analysis approach and aeroacoustic solver with pressure distribution approach, and is based on a series of rotor dynamic, aerodynamic, and aeroacoustic analysis. In the thesis, its application is carried out for the investigation of aerodynamic and aeroacoustic behavior of both conventional and scissors tail rotors.

1.3 Literature Review

1.3.1 Helicopter Main Rotor and Tail Rotor Aerodynamics

A helicopter is an aircraft that travels in any direction and can hover in the air. Conventional helicopters have one main rotor which generates main portion of the lift and a tail rotor which is required for acting as an anti-torque generator against the main rotor torque. Due to their rotation, aerodynamics over the main and tail rotors are quite complicated. The impact of the main rotor on air is significant. On the other hand, tail rotor has a smaller effect on air comparing to main rotor. However, the tail rotor is located downstream on conventional helicopters and therefore disturbed by the main rotor wakes. In many flight conditions, this interaction is quite significant. The main rotor wake carries momentum flow and trailing vortex of the main rotor through downstream. This phenomenon changes the flow behavior that encounters the tail rotor, and this is illustrated in Figure 1.1.

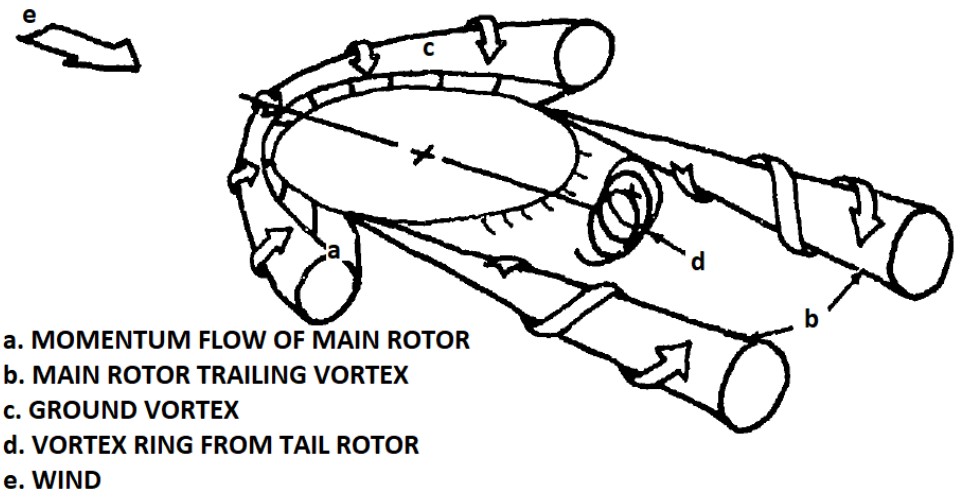

Figure 1.1: Flow Environment of Tail Rotor [1]

The main rotor wake impacts the tail rotor, and this generates non-harmonic loads on it. This effect also acts as a source of structural loads, vibration, and noise [2]. The location of the interactions is a function of several parameters, such as the angle between the main rotor plane and tail rotor plane, direction of

the tail rotor rotation, tail rotor geometry and flight conditions [3]. Directions of rotation for the tail rotor which might be named as bottom-forward and top-forward, and schematic of these configurations are shown in Figure 1.2. Bottom-forward is a better option to minimize required collective pitch for a given solidity, tip speed, thrust, and pedal excursions during hover turns [1]. It is also pointed out that bottom-forward configuration has a better directional control capability than top-forward configuration [2]. Bottom-forward reduces the number of interactions, and it leads to less unsteady airloads and less noise [3].

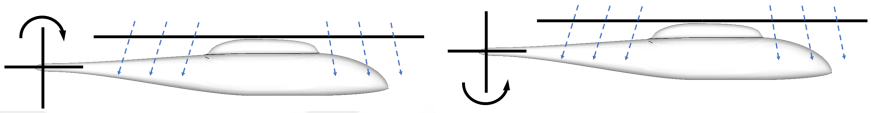

(a) Top-Forward (TF) (b) Bottom-Forward (BF)

Figure 1.2: Tail rotor turn direction

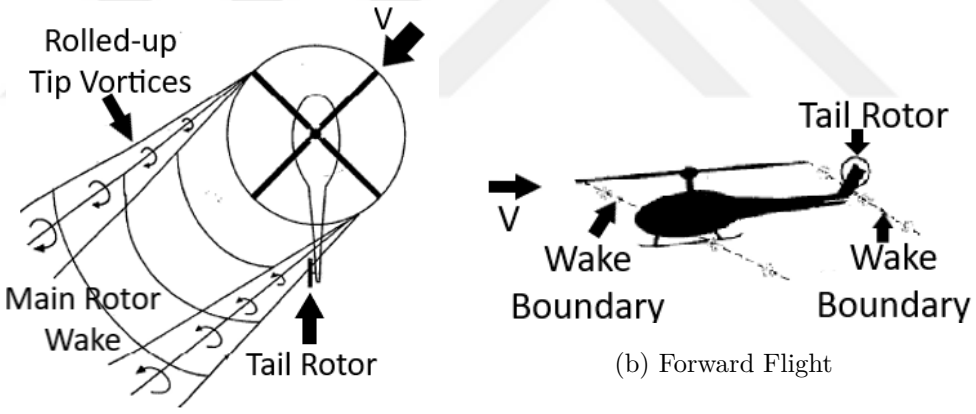

(a) Quartering Flight (b) Forward Flight

Figure 1.3: Main rotor wake on tail rotor in different flight conditions [3]

It is mentioned above that the flight condition has a major effect on the main rotor-tail rotor interaction. Possible flow fields of quartering and low speed forward flight conditions are presented in Figure 1.3. The main results may be summarized below [4].

i. Near hover condition, main rotor wake does not affect the tail rotor significantly.

ii. In low speed forward flight condition, the tail rotor might be influenced by the main rotor wake and the wake generated by itself.

iii. Quartering flight condition, the tail rotor is influenced by the main rotor significantly.

iv. Side and rearwards conditions, main rotor wake does not cut the tail rotor.

Another comprehensive research about tail rotor was done by Wisner [1]. The study indicated that the result of interaction of main rotor has a great influence on the thrust of tail rotor, shown in Figure 1.4.

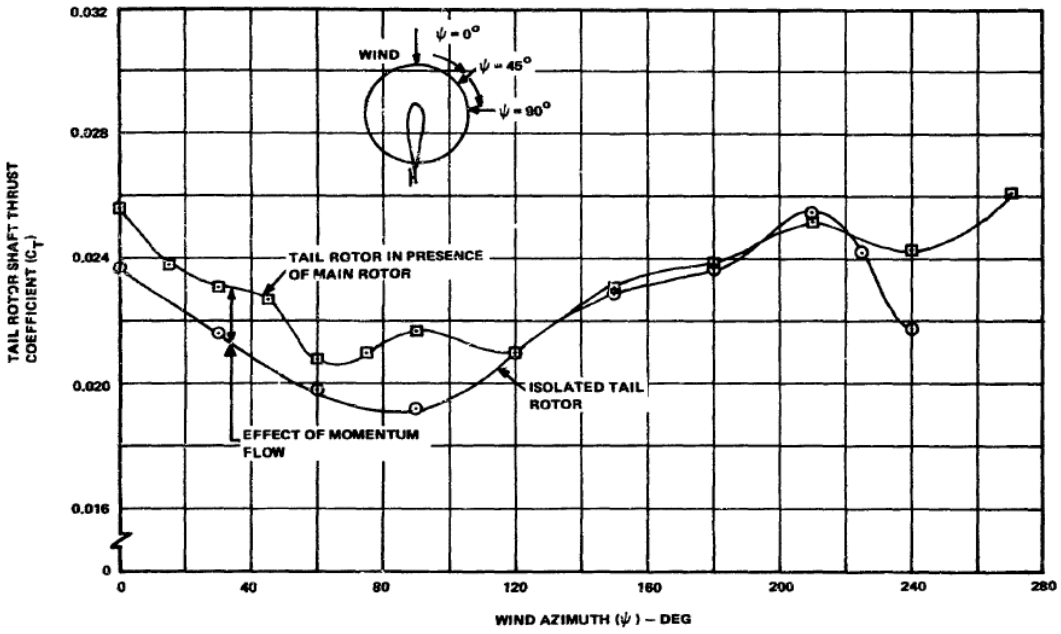

Figure 1.4: Effect of Main Rotor Interaction, V = 36 Knot, BF rotation [1]

1.3.2 Noise Reduction of Helicopter

The growth of the helicopter industry creates a problem, noise. Usage of the helicopter in civil areas such as above city centers is becoming widespread, and noise generated by helicopters is turned to be a problem. This situation brings

a need for noise reduction for helicopters. There are two components as a major noise source in conventional helicopters, the main rotor and tail rotor. Each rotor radiates unique and recognizable noise due to various flight conditions. Typical noise components generated by helicopters is summarized in Figure 1.5. An investigation called SILENT Program has been carried out to decrease noise generated by the main rotor using unequal blade spacing (modulated blade spacing) [5].

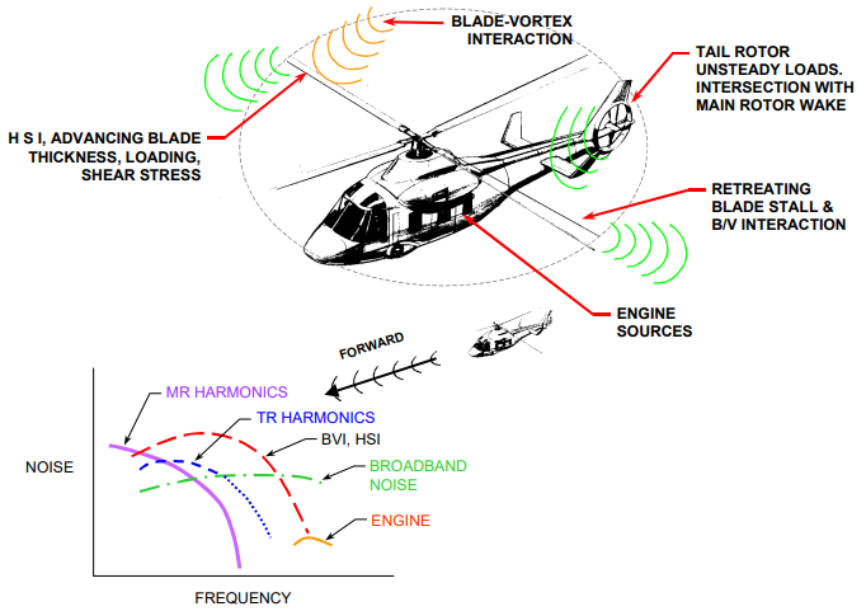

Figure 1.5: Noise Generation Components of Helicopters [5]

In the aforementioned research, several methodologies are discussed in a preliminary assessment below.

i. Modulated blade spacing illustrated in Figure 1.6,

- Potential Blade Vortex Interaction (BVI) noise reduction without changing the performance
- Increasing the complexity of hub manufacturing

ii. X-Force control,

- Potential BVI noise reduction

- Non-standard flight control system

iii. Reduced tip speed design,

- Noise reduction in all noise mechanism
- Increasing on weight due to heavier drive system

iv. Blade tip modification,

- Decreasing BVI and High Speed Impulsive (HSI) noise
- Increasing cost, complexity of manufacturing and possibly profile drag

v. Airfoil tailoring,

- Reduction in HSI
- Increasing cost, profile drag

vi. Active controls,

- Potentially BVI noise reduction
- Possibility of incrementation on vibration, complexity of manufacturing

vii. Variable diameter rotor,

- BVI noise reduction is expected
- Complex and hard to implement

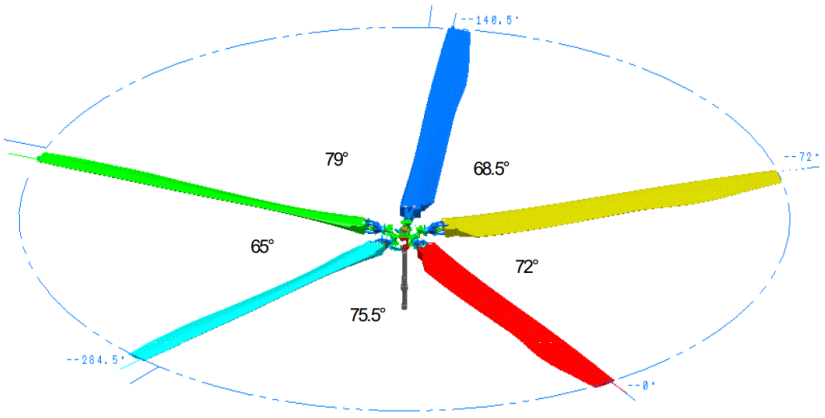

Figure 1.6: Main Rotor Configuration of SILENT Program [5]

Modulated blade spacing is employed on the rotor due to noise reduction without changing on the performance of the rotor. The main idea behind the usage of modulated blade spacing was to spread over the acoustic frequencies. Equal blade spacing generates acoustic frequencies with large amplitude pressures. On the other hand, modulated blade spacing produces acoustic frequencies with small amplitude pressures. As a result of the SILENT Research Program, the modulated blade spacing approach was determined as a promising methodology to reduce helicopter noise.

Additionally, noise signature of coaxial rotor helicopters are investigated experimentally and numerically, and it is found that some of the flight conditions upper rotor is highly interacted with the tail rotor, and it causes strong BVIs [6–8]. Therefore, coaxial rotor helicopter has higher noise signature than a conventional helicopter. On the other hand, due to absence of tail rotor, tail rotor based noise signature vanishes. Another approach for advanced design is fenestron type tail rotors. Fenestron has larger noise level than an conventional tail rotor, however, the noise level is highly directional and is reduced in at azimuth positions near the longitudinal axis of the helicopter [9].

Furthermore, reduction of noise emission from the tail rotor was evaluated theoretically and experimentally. It was found that tail rotor rotation direction, tail rotor position relative to main rotor, and rotation speed affects the noise radiation from the tail rotor significantly [10–12].

In the next part of the literature review, modulated blade spacing implementations on tail rotor is discussed.

1.3.3 Scissors Tail Rotor

Main rotor wake - tail rotor interaction affects the performance and airloads on tail rotor. In addition, this interaction increases noise significantly [13, 14]. The acoustic signature generated by helicopter is a challenging issue for both military and civil helicopters. Even the tail rotor has smaller dimensions than the main rotor, and it might radiate more noise than main rotor in some of the

flight conditions [15].

One of the possible proposed methods to reduce to noise generated by the tail rotor is to design a modulated blade spacing tail rotor, called scissors tail rotor [16]. An application of the scissors tail rotor configuration has been made onto AH-64 Apache attack helicopter and Mi-28 Havoc shown in Figure 1.7.

(a) AH64 (b) Mi-28 Havoc

Figure 1.7: Example helicopters using scissors type tail rotor

Scissors tail rotors are produced by two rotors with two blades, and their hub centers are attached by a space, which is called vertical distance. Additionally, attached rotors may have an azimuthwise offset angle that is called scissors angle. Therefore, design of the scissors tail rotor has two design parameters, vertical distance and scissors angle, as illustrated in Figure 1.8.

i. Scissors angle: the angle between two rotors

ii. Vertical distance: the distance between two rotors

Preliminary research on scissors tail rotor is held with a full-scale tail rotor in a whirl tower that corresponds to hovering flight condition [17]. The test is conducted by different scissors angle and vertical spacings. It was shown that scissors tail rotor reduces the noise and has a better performance comparing to conventional tail rotor in some configurations.

Lately, experimental studies are carried out on an isolated tail rotor configuration by the National Key Laboratory of Science and Technology on Rotorcraft Aeromechanics [18–20]. The results of conducted investigations show that,

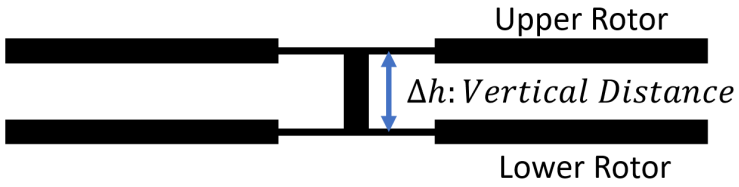

(a) Vertical Distance

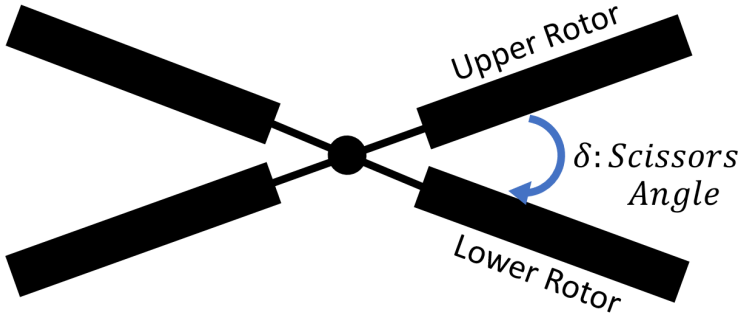

(b) Scissors Angle

Figure 1.8: Schematic of scissors tail rotor

i. Scissors rotor suffers from the BVI phenomenon, and this phenomenon occurs at some scissors configuration.

ii. Upper rotor system interacts strongly on lower rotor system.

The numerical studies were performed by CFD tools coupled with numerical integrations of the Ffowcs Williams Hawkings (FW-H) noise equation on an isolated scissors tail rotor [21–23]. The studies focused on understanding the effects of flight conditions such as hover and forward flight and effects of scissors tail rotor configuration on the emitted noise. The results showed that,

i. Noise characteristic of scissors tail rotor is different than conventional tail rotor.

ii. Scissors angle has a significant influence on noise generated by tail rotor.

iii. Noise level of scissors tail rotor is not always lower than conventional tail rotor. Therefore, selection of scissors angle and scissors vertical space is essential to reduce noise level.

Scissors tail rotors were investigated in the literature using CFD tools without the main rotor effects. On the other hand, the scissors tail rotor is investigated via comprehensive analysis including the main rotor effects and its coupling with an aeroacoustic solver in the present study. A brief explanation of this analysis tool is given in the next section.

1.4 Comprehensive Analysis

Helicopter is inherently complex and multidisciplinary, hence helicopter analysis is driven by the comprehensive analysis. Comprehensive analysis is an analyzing method that solves aerodynamics, dynamics, and structural analysis for rotary wing technologies. Design and development of a rotary wing need capability of calculation of the loads and performance. This calculation might be done by the comprehensive analysis tool calculating the aeromechanical behavior and solving aerodynamics, elasticity of rotor blades, nonlinear dynamics, and more. This kind of tool is a well suited and fast way of computing vibration, aeroelastic stability, and flight dynamics. Each comprehensive analysis program has a unique capability. While one calculates performance and loads with low fidelity, another program calculates performance and loads with high fidelity. While one might use freewake methodology to find induced velocity on the rotor, another might use inflow models to predict induced velocity on the rotor.

In this study, pressure distribution over rotor blades has an essential role in investigating oscillatory loads and noise. Therefore, a high fidelity methodology is required to predict induced velocity over rotor and rotor blades. Freewake is one of the high fidelity methodology to predict induced velocity and airflows around rotor. Thus, a comprehensive analysis tool is used which operates with freewake methodology, which is called the Comprehensive Hierarchical Aeromechanics Rotorcraft Model (CHARM) gives fast and accurate prediction of rotor blade loads, rotor wake, and rotor dynamics for a comprehensive rotorcraft analysis [24, 25]. The aerodynamic model has a combination of Constant Vorticity Contour (CVC) free-vortex wake model with a vortex lattice and lifting surface panel model to give an intensive capability for modeling rotorcrafts. CHARM

can reconstruct wake with higher resolution, and this ability helps to catch blade-vortex interaction loads successfully. It is also a highly used comprehensive tool for the noise analysis of rotorcrafts [13, 26–31].

CHARM has a couple of input files to have an analysis. These files contain information about the blade geometry, blade dynamics, rotor-wake dynamics, and airfoil look-up table. Such as twist angle, length of the blade, sweep angle and chord length chord length are given in blade geometry file. Blade dynamics file contains such as weight of the blade, elastic modeling and hinge locations. Rotor incidence angles, rotation speed, number of blades and vortex modeling are given in rotor-wake dynamics file. Airfoil properties such as lift, drag and pitching moment coefficients are given in airfoil look-up table. Several outputs are provided from CHARM. Wake geometry, aerodynamic properties, induced velocity, airloads and distributed performance etc.

1.4.1 Blade Aerodynamics

The solution of sectional aerodynamics in CHARM is performed typically using a vortex lattice method (VLM). In addition to that, 2-D airfoil data lookup table is used to give detailed information about the profile drag, compressibility, stall characteristics and pitching moment. VLM is an approach that covers 3D effects, localizing the effect of blade-vortex interactions and prediction of tip loading with implementation of real blade geometry.

1.4.2 Rotor Wake

CHARM uses a CVC free wake method that is a variation of the model developed under NASA sponsorship [32, 33]. This model uses curved vortex filaments released by the span of the each blade representing constant-strength contours of vorticity in the trailing vortex sheet. The advantages of this technique are listed below.

i. Rollup process of each blade is calculated directly.

ii. Tip vortex core radius is calculated directly.

iii. Rollup process of rotational environment is calculated directly instead of using empirical model.

iv. Positive and negative tip vortex interactions are captured during blade-vortex interactions.

v. Curved vortex elements provide more accurate predictions.

1.5 The Outline of the Thesis

Chapter 1 involves the objective of the study and literature review. Studies on air flow over tail rotor, tail rotor rotation configurations, main rotor-tail rotor interaction, noise reduction methodologies and scissors tail rotor are briefly reviewed and explained. At the end of the chapter, one of the comprehensive analysis tool in rotorcraft industry, CHARM, is introduced which is used in this study.

Chapter 2 includes discussion of comprehensive analysis modeling studies using rotor performance and sectional blade loads using CHARM.

The coupling strategy between the comprehensive rotorcraft analysis and the aeroacoustic solver is introduced and discussed in Chapter 3. Validation of the critical phase that transfers aerodynamic loads resulted from the rotorcraft dynamic and aerodynamic analysis to the aeroacoustic solver is performed for the HART-II case [34].

Chapter 4 presents results from a comprehensive application of the coupled analysis approach. Several design parameters are studied for the tail rotor configuration taking into account of both aerodynamic and aeroacoustic considerations. The interaction of the main rotor wake with the tail rotor is included. The rotor vertical distance and scissors angle parameters are evaluated at several flight conditions.

Finally chapter 5 summarizes the overall study.

CHAPTER 2

COMPREHENSIVE ANALYSIS MODELING

This chapter carries out a comprehensive analysis modeling study for the aerodynamic and mathematical model that is used in future investigations. In the first section, the required power of the isolated rotor configuration of the S76 helicopter is validated. Additionally, results from various vortex core models to generate the required aerodynamic data are compared with experimental data. In the following section, the required power data for the full AH64-D helicopter configuration is computed and compared with available data. In the last section, several sectional blade loads of UH60-A are compared with the wind tunnel test data to validate the overall mathematical and aerodynamic model.

2.1 Isolated Rotor Validation

Generally, designing a helicopter starts with the design of the main rotor. Therefore, the first aim is to find required power for different configuration options of the main rotor in the early stage of the helicopter design. Wind tunnel testing is generally applied to the main rotor to validate analysis or create more accurate mathematical models. In this section, a full scale wind tunnel test, namely Sikorsky S-76 Full Scale Rotor Performance Test [35], is modeled using CHARM employing freewake methodology. In this test, the full-scale main rotor of S-76 is tested at different shaft angles, different speeds, and various thrust levels to cover all possible flight regimes. Solid body modeling of vortex core, diffusion model of the vortex core, and numerical solution procedures are obtained to validate S-76 mathematical and aerodynamic model. In the validation, hover and forward flight power curves are used [35, 36].

2.1.1 Mathematical & Aerodynamic Model

The main rotor of S-76 is a 4-bladed rotor with 22ft radius and -10 degree linear twist. One blade of this rotor is depicted in Figure 2.1, and the modeling parameters are summarized in Table 2.1.

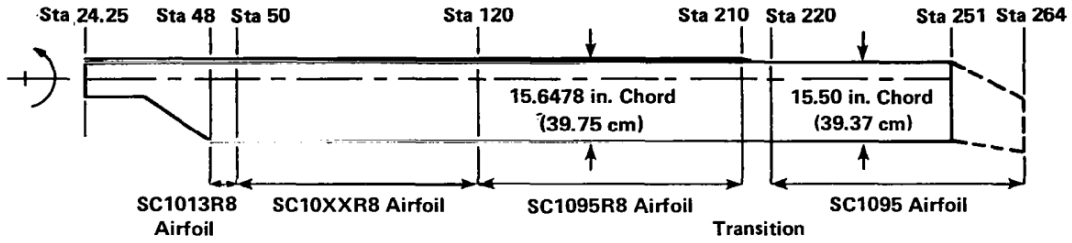

Figure 2.1: S-76 main rotor schematic [36]

Table 2.1: S-76 main rotor parameters [35]

Parameter	Value	Unit
Radius	22	ft
Nominal Chord	15.5	in
Nominal Twist	-10	deg
Number of Blades	4	-
Flapping Hinge	3.70%	Radius
σ	0.0748	-
100% RPM	293	-
Airfoils	SC1095 & SC1095R8	-

A challenging part of modeling a helicopter for comprehensive analysis is to generate a proper aerodynamic model for free-wake analysis. Free-wake methodology calculates the location of the vortices generated by the rotors. This methodology requires the vortex core to be modeled and calculated along with the resultant locations of the vortex filaments. Additionally, the vortex core dimension helps to define the structure and evolution of tip vortices. A vortex core may be modeled with a solid body rotation approach. Vortices generated by a rotor

blade is shown in Figure 2.2.

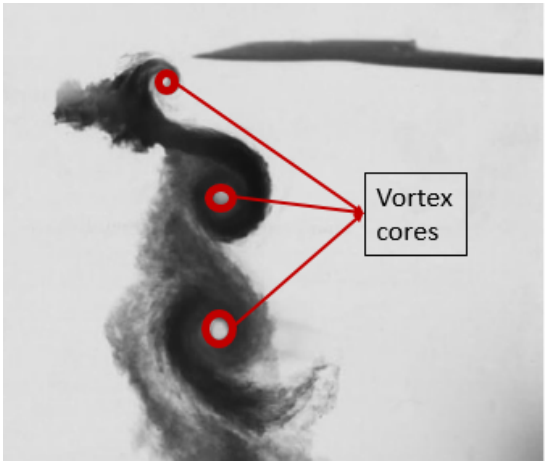

Figure 2.2: Vortices generated by a rotor blade [2]

Different models of vortex core are investigated using the tangential velocity values and compared with experimental data.

Tangential velocity of vortex along radial distance by potential flow is given in Eq. 2.1.

$$V = \frac{\Gamma}{2\pi r} \tag{2.1}$$

Rankine vortex core is a modeling of pure solid body rotation, and is formulated as in Eq. 2.2.

$$V = \frac{\Gamma}{2\pi r_c} \begin{cases} r/r_c & r \leq r_c \\ \dfrac{1}{r/r_c} & r > r_c \end{cases} \tag{2.2}$$

Lamb-Oseen vortex core [37] is obtained from the solution of Navier-Stokes equation for decay of a laminar vortex.

$$V = \frac{\Gamma}{2\pi r_c}(1 - e^{1.2567 r^2/r_c^2}) \tag{2.3}$$

Another vortex core model is called as power or Vatistas core model [38].

$$V = \frac{\Gamma}{2\pi r_c} \frac{r^2}{(r^{2n} + r_c^{2n})^{1/2n}} \qquad \text{n=0, 1, 2 ...} \tag{2.4}$$

In Eq. 2.4, when n equals to 1 then Vatistas vortex core model simplifies to Scully vortex core model [39].
Tangential velocities are nondimensionalized by $\Gamma/2\pi r_c$ and the comparison of the nondimensional tangential velocities of these vortex core models with experimental data [40] is illustrated in Figure 2.3.

It appears from the nondimensional tangential velocity comparsion that Vatistas $n = 2$ vortex model is closest to experimental data. Therefore, Vatistas $n = 2$ is used for the vortex core models in this study. Following this, a diffusion model for the wake is needed. This model is selected as a linear one, starting after $\frac{360[deg]}{NoB}$. This means that the following blade passes through the position of vortex creation [3].

Generated vortex core and diffusion model are used in all investigations through this study.

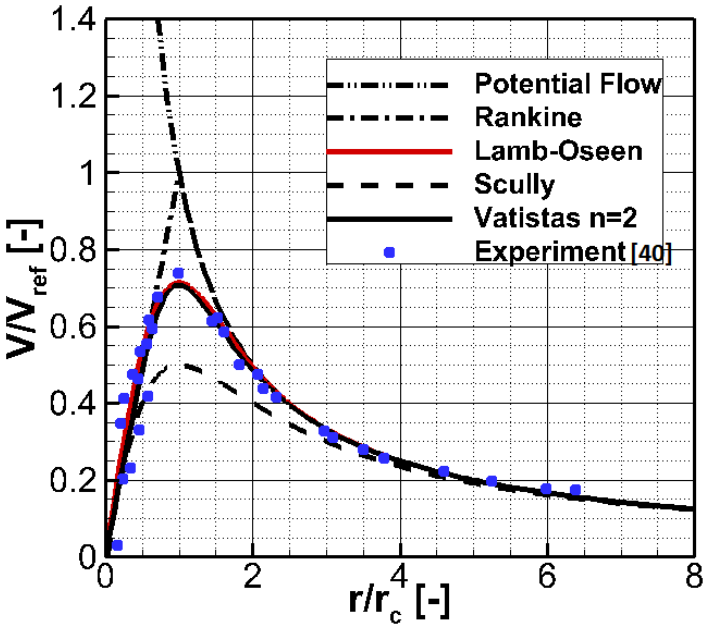

Figure 2.3: Non-dimensional tangential velocity comparison of different vortex core models with experimental data [40]

2.1.2 Validation

The computed thrust coefficient by Eq. 2.5 and power coefficient by Eq. 2.6 are compared for hover condition with the data of Sikorsky Whirl Tower Test [36] in Figure 2.4. In the some of the comparisons coefficients are divided by solidity, the ratio of total blade area to the disk area. The comparison shows that the analysis results and test data are highly correlated for this case. The predicted required power values are in line with the whirl tower test data at the same thrust.

$$C_T = \frac{T}{\rho\pi R^2(\Omega R)^2} \tag{2.5}$$

$$C_Q = \frac{Q}{\rho\pi R^3(\Omega R)^2} \tag{2.6}$$

Further investigation on the isolated rotor is performed in terms of the power-velocity relation. Figure 2.5 shows the predicted power coefficient advance ratio relation at different shaft tilt angles in comparison with the AMES 80x120 wind tunnel test results [35]. Above the 0.05 advance ratio, the test and analysis results agree highly. However, the results deviate from each other below 0.05 which is mainly due to wall effect in wind tunnel test.

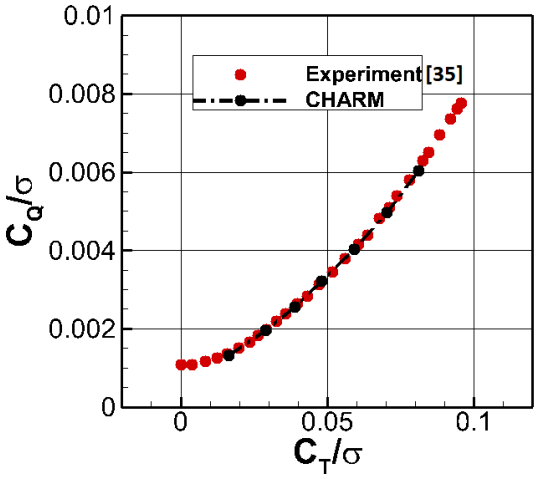

Figure 2.4: S-76 main rotor thrust and power coefficient comparison ($\alpha_s = 0°$) with test data [35]

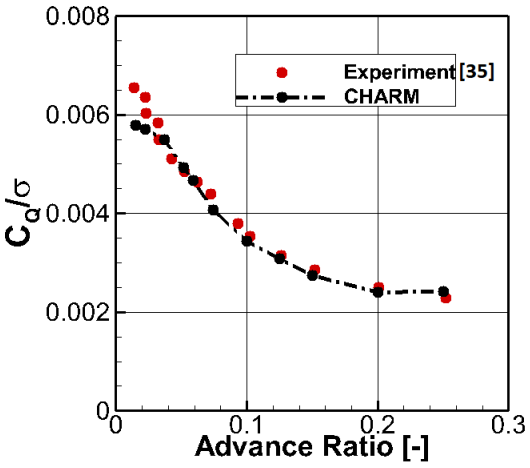

(a) $\alpha_s = 0°$, $C_T/\sigma = 0.080$

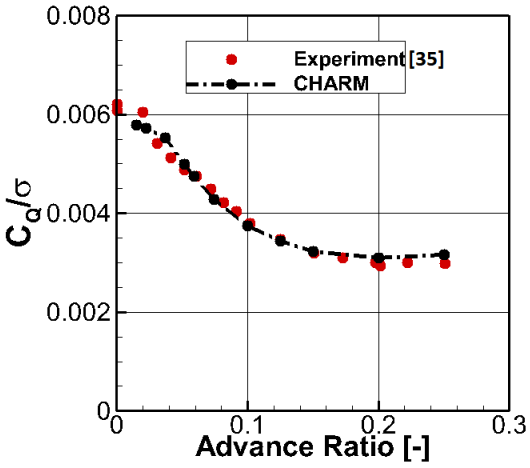

(b) $\alpha_s = -2°$, $C_T/\sigma = 0.080$

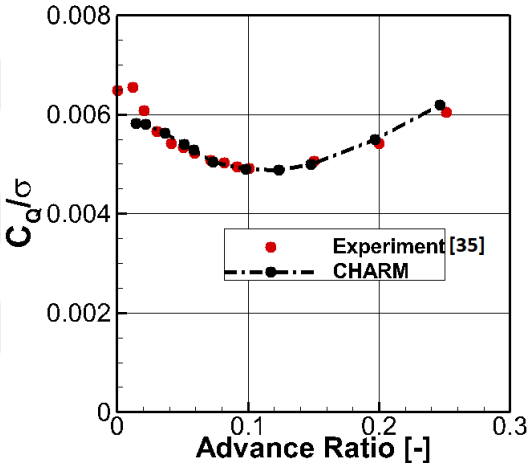

(c) $\alpha_s = -10°$, $C_T/\sigma = 0.080$

Figure 2.5: Advance ratio and S-76 main rotor power coefficient comparison with test data [35]

2.2 Full Helicopter Validation

One way to show the capability of an analysis program in the rotorcraft industry is to perform full helicopter trim and its required power data validation. For this section, AH64-D is modeled in CHARM with its main rotor, tail rotor, as well as proper fuselage aerodynamic database. Required power from the analysis results are compared with the data given in Technical Manuel of AH64-D [41]. Since

this power value corresponds to engine torque percentage, scaling is performed. One percent torque corresponds to 28.56 horsepower, when interpolated from the transmission limit of 2856 horsepower for 100% torque [42].

2.2.1 Mathematical Model

The main rotor of AH64-D Apache Longbow is a 4-bladed rotor with 24ft radius and -9 degree linear twist. One blade of this rotor is illustrated in Figure 2.6.

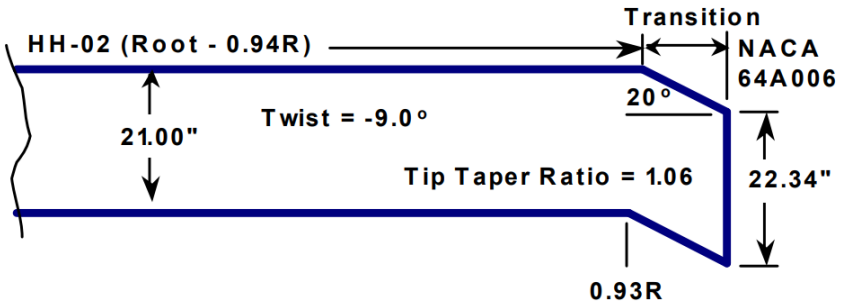

Figure 2.6: AH64-D Apache Longbow Helicopter Main Rotor Blade [42]

The model is implemented in CHARM using the full helicopter trim option and free-wake with various forward flight speeds to generate the power curve. The properties of the main rotor is given in 2.2.

Table 2.2: AH64-D Helicopter Properties [42, 43]

Parameter	Value	Unit
MR Number of Blades	4	-
MR Radius	24	ft
MR Blade Chord	21.00	in
MR Equivalent Linear Twist	-9	deg
MR Blade Tip Sweep/Aft	20	deg
MR Rotational Speed	30.6	rad/s
MR Airfoils	HH-02/NACA-64A006	-

2.2.2 Validation

The required total power values from the analysis for various forward flight speeds are compared with the available required power data from technical manual [41] and shown in Figure 2.7. In the analysis a gross weight of 19000 and sea level with +20C^{o} conditions were used.

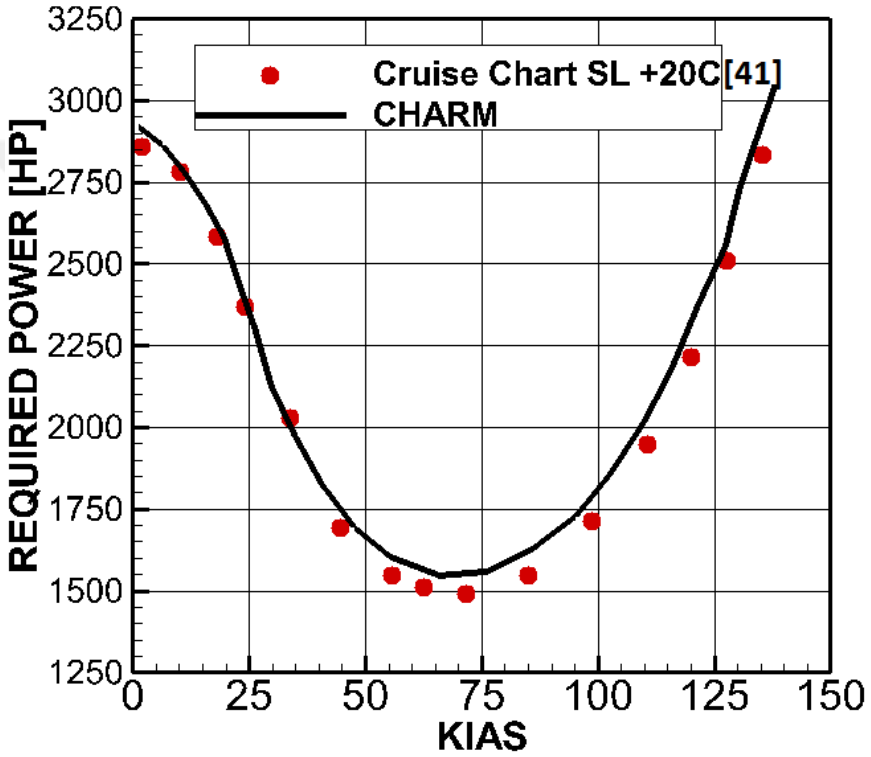

Figure 2.7: Full helicopter required power comparison with data from technical manual [41]

The differences observed between the computed and technical manual data arise mainly from the uncertainty of the modeling of the helicopter. Nevertheless, a good correlation between the two sets of data is apparent. The next section involves an intensive investigation and validation of the aerodynamic model with airloads comparison.

2.3 Airloads Validation

The validated required power gives a general idea about the accuracy of the computed results and confidence level in the mathematical model. However, to explore the confidence levels further on the aerodynamic model, airloads validation is essential. This section includes the validation of sectional airloads of Full-Scale Wind Tunnel Test of UH60-A [44]. This test was performed in "the U.S. Air Force National Full-Scale Complex 40 by 80 Foot Wind Tunnel" using a Sikorsky Aircraft UH60-A rotor system, and the rotor system in wind tunnel is shown in Figure 2.8. The purpose of the test is to understand the underlying

Figure 2.8: UH60-A Rotor System in Wind Tunnel [44]

complexity of the dynamics and aerodynamic of the rotating system. This test provides a comprehensive set of validation data for modeling and simulation tools. Therefore, tests are performed for several conditions. Some of them are listed below.

i. 1-g level flight sweeps

ii. Airloads flight test simulation

iii. PIV testing

2.3.1 Mathematical Model

The test is performed with a full-scale rotor system of UH60-A. Therefore, a representative mathematical model is required for CHARM, which is given in Table 2.3.

Table 2.3: UH60-A Rotor Properties [44, 45]

Parameter	Value	Unit
Number of Blades	4	-
Rotor Radius	26.83	ft
Blade Chord	20.76	in
Equivalent Linear Twist	-18	deg
Blade Tip Sweep/Aft	20	deg
Geometric Solidity	0.0826	-
Root Cutout	2.951	ft
Rotational Speed	27	rad/s
Airfoils	SC1095/SC1095R8	-

It is aimed that how accurate the sectional airloads may be predicted. Therefore, some of the airloads flight test cases are simulated, and simulated conditions are listed in Table 2.4. These test conditions are implemented in CHARM using thrust and moment trim.

Table 2.4: UH60-A Test Conditions [45]

Parameter	One	Two	Three
Advance Ratio [-]	0.2	0.3	0.4
Thrust Coefficient [-]	0.0075	0.0075	0.0075
Corrected Shaft Tilt [deg]	-0.31	-3.40	-7.60
Rolling Moment Coefficient [-]	0	0	0
Pitching Moment Coefficient [-]	0	0	0

2.3.2 Validation

This section represents the validation results of sectional airloads at station 92% of the radius is used and illustrated in Figure 2.9. The results of CHARM are compared with related test results, CAMRAD II, and CAMRAD II-OVERFLOW 2 coupling results [46].

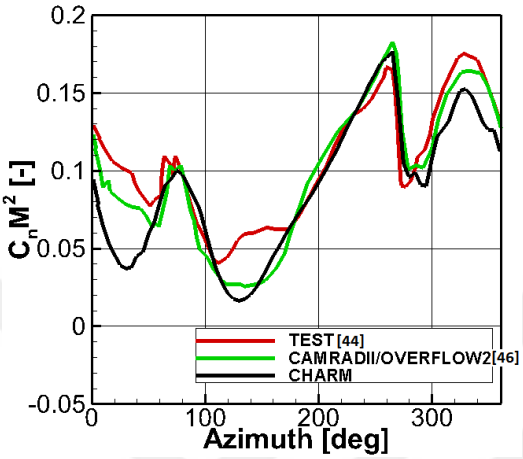

(a) 92% R, $\mu = 0.20$

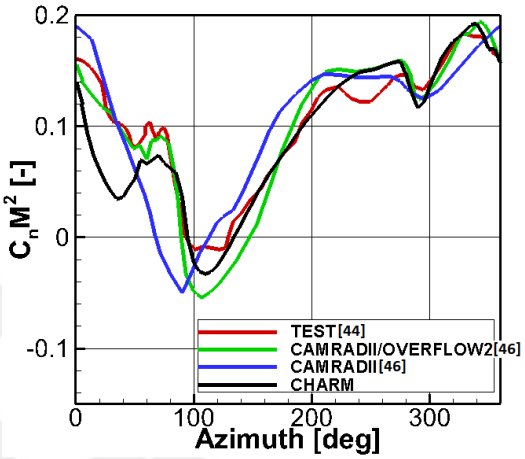

(b) 92% R, $\mu = 0.30$

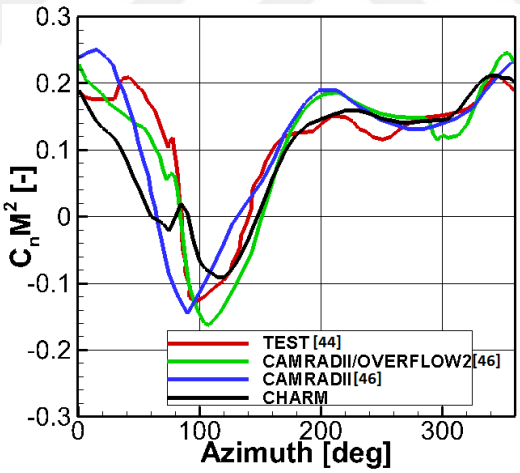

(c) 92% R, $\mu = 0.40$

Figure 2.9: Nondimensional sectional normal force comparison with data from literature [44, 46]

CAMRAD II is another comprehensive analysis tool to analyze rotorcrafts aeromechanism with free-wake. Analysis performed by CAMRAD II involves a dual-peak

wake model except at advance ratio 0.2. OVERFLOW 2 is an overset, structured mesh flow solver developed by NASA. OVERFLOW 2 is coupled with CAMRAD II to analyze UH60-A wind tunnel test conditions [46].

CHARM and CAMRAD II have lower fidelity in aerodynamic modeling than current CFD tools. However, these comprehensive tools have the capability to model aeromechanics of rotorcraft and to perform trim analysis. CHARM predicts the airloads quite accurate comparing to CAMRAD II. In advancing side, CHARM underpredicts the airloads with similar trend of the test results. On the other hand, it predicts more accurately for retreating side. For a general comparison, CHARM gives similar prediction to CAMRAD II, yet slightly worse than CAMRAD II/OVERFLOW 2 coupling. The reason behind of it CHARM uses 2-D lookup tables which contains airfoil lift, drag and moment coefficient. However, OVERFLOW 2 solves the flow around rotor system.

To sum up, CHARM predicts the airloads and performance sufficiently correlated with the test data using lower fidelity aerodynamic model than CFD. On the other hand, it brings several advantages such as capability of modeling rotorcraft dynamics and full helicopter trim methodologies. Therefore, CHARM offers fast, reliable performance and airloads prediction for a full helicopter.

CHAPTER 3

AEROACOUSTIC METHODOLOGY AND VALIDATION

In this chapter, a pressure distribution methodology is introduced to supply the noise prediction phase with the required blade pressure loadings. As aforementioned, CHARM is used as the comprehensive analysis tool for rotor dynamics and aerodynamics. Noise predictions are carried out using the Turkish Aerospace noise prediction tool TACO that was developed by the Middle East Technical University [47].

The proposed coupling methodology initially requires freewake analysis from CHARM with reconstruction option. Next, the developed methodology to find reconstructed angles of attack and Mach numbers is called. After that, a previously generated pressure database of the airfoil is adjusted on the blade for each blade section and azimuth angle. Finally, the pressure distributed blades are provided to TACO for aeroacoustic analysis. The coupling strategy is schematically illustrated in Figure 3.1, and the details of the methodology are given in the following sections. At the end of this chapter, CHARM and TACO are coupled and the coupling methodology is validated using the HART II baseline test case.

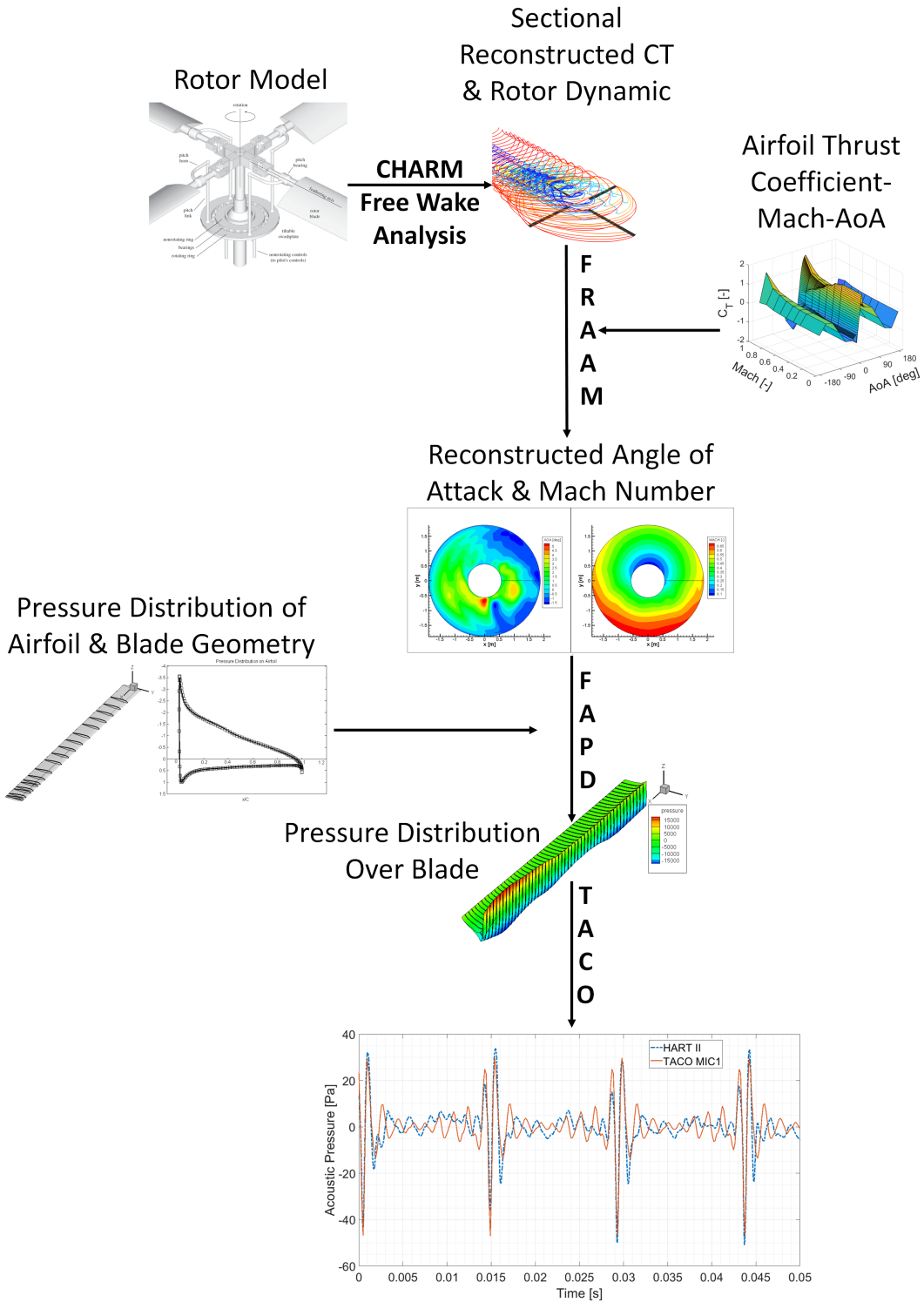

Figure 3.1: Proposed Acoustic Analysis Methodology

3.1 Acoustic Solver: TACO

Turkish Aerospace Acoustic Code (TACO) was developed specifically for helicopter noise predictions within a Turkish Aerospace Industry and Middle East Technical University cooperative program [47]. The code integrates the Ffowcs Williams-Hawkings (FW-H) equation 3.1, given as,

$$\left(\frac{1}{c_0^2}\frac{\partial^2}{\partial t^2} - \nabla^2\right) p' = \frac{\partial}{\partial t}\{[\rho_0 v_i + \rho(u_i - v_i)]n_i\delta(f)\} - \frac{\partial}{\partial x_i}\{[(p - p_0)\delta_{ij} - \tau_{ij} + \rho u_i(u_j - v_j)]n_j\delta(f)\} + \frac{\partial^2}{\partial x_i \partial x_j}[T_{ij}H(f)] \tag{3.1}$$

where c is the speed of sound, p' is pressure fluctuation (deviation from ambient pressure), ρ is density, v_i is velocity of the surface defined implicitly by equation $f = 0$, u_i is fluid velocity, $\delta(f)$ is Dirac delta function, δ_{ij} is Kronecker delta function, τ_{ij} is viscous stress tensor, $H(f)$ is Heaviside function, T_{ij} is the Lighthill stress tensor, and zero subscript represents ambient value of that quantity. Right hand side of the equation has three source term, and these are named monopole, dipole and quadrupole sources, respectively. These sources are produced by volume displacement, loading and turbulence flow, and they may also named as thickness noise, loading noise and turbulence noise, respectively.

TACO integrates the FW-H equation with advanced algorithmic options. The user may choose between retarded and forward time integration approaches, as well as between parallel processing options of splitting either the integration surfaces or integration times over multiple processors for fast computations for multiple observer locations. Also, blade loadings that may be supplied with directly either from unstructured or structured mesh CFD solvers can be handled with ease. In addition, many different flight scenarios such as wind tunnel situations with fixed observer (microphone) locations, steadily moving helicopter with fixed or moving observer locations, as well as maneuvering motions can be handled. The required inputs are the time dependent rotor shaft and relative blade motions with blade mesh pressure distributions. If a steady flight with steady harmonic rotor motion is investigated, data only for one rotor revolution

is sufficient. If a maneuvering situation or rotor motion with multiple harmonics situation is computed, data is needed for higher number of revolutions to sufficiently accumulate the acoustic signals at microphone locations for physically meaningful results.

Some of the algorithmic discussions and validations studies are provided in Ref. [47]. Further validation studies with sensitivity analyses, in hover and forward flight conditions comparing with available test data are given in Refs. [13, 29, 30].

3.2 Axis System

This part explains two different axis systems: a blade attached rotating axis system and a non-rotating hub axis system.

The blade axis is attached to the blade and rotates with the blade. X is positive radially outward, Y is positive towards leading edge, and Z is positive upward as illustrated in Figure 3.2. The origin is fixed at the root of the blade and quarter chord position.

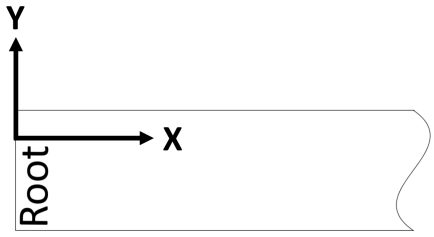

(a) View on XY plane

(b) View on YZ plane

Figure 3.2: View of Blade Axis

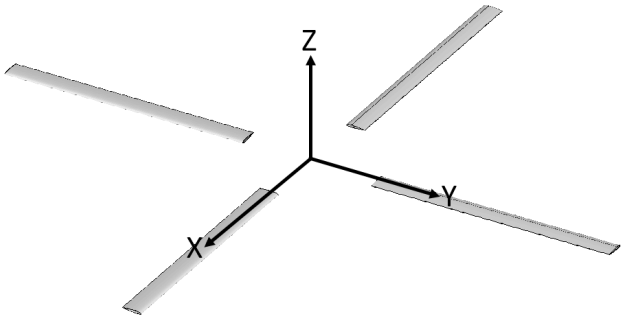

Figure 3.3: Isometric View of Non-rotating Hub Axis

The non-rotating hub axis is attached to the center of the hub and does not rotate. X is positive rearward, Z is positive upward, and Y is positive rightward due to right hand rule shown in Figure 3.3.

3.3 Mathematical Model

In aeroacoustic validation, a very well known and documented test named case 2nd of the Higher Harmonic Control Aeroacoustic Rotor Test (HART II) program is used [34,48]. HART II uses a 40% geometrically, dynamically, and Mach scaled main rotor system of the Bo105 helicopter.

In this part, the baseline configuration of HART II is investigated and validated for sectional aerodynamic loads and aeroacoustics. Test conditions of the baseline configuration and geometric specifications are given in Table 3.1 and Table 3.2, respectively. In addition, the experiment is handled in a wind tunnel. Therefore, the existence of wind tunnel interference is reflected upon the shaft angle of attack with a value of -0.8°. A representative free-wake visualization of the solution is exemplified in Figure 3.4.

The mathematical model is implemented into CHARM, and analyzed with the reconstruction option. In the next section, transformation of the reconstructed data provided by CHARM is explained to distribute pressure over the blade.

Table 3.1: HART II Test Condition [34, 48]

Parameter	Value	Unit
Air Pressure	100.97	kPa
Air Temperature	17.3	°C
Air Density	1.2055	kgm^3
Speed of Sound	341.7	m/s
Rotor Shaft Angle	5.3	deg
Advance Ratio	0.151	-
Thrust Coefficient	0.00457	-

Table 3.2: HART II Model Properties [34, 48]

Parameter	Value	Unit
Rotor Radius	2	m
Blade Chord	0.121	m
Linear Twist	-8	deg
Number of Blades	4	-
Root Cutout	0.44	m
Rotational Speed	109.12	rad/s
Airfoils	NACA23012	-

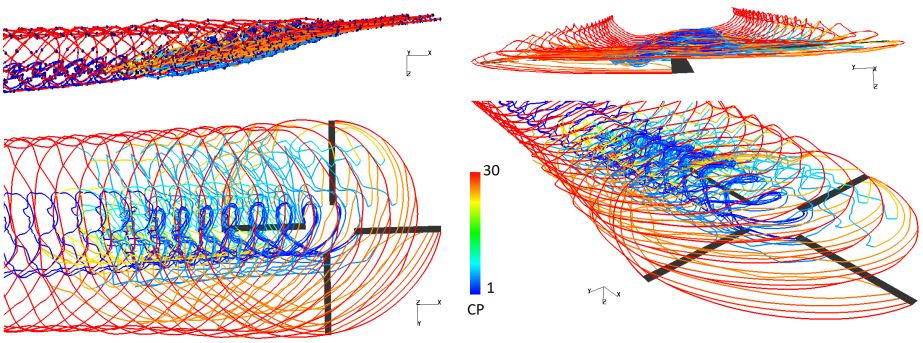

Figure 3.4: HART II Freewake Visualization

3.4 Methodology of Pressure Distribution

Pressure distributions on the blades are essential as inputs to aeroacoustic analysis. Generally, the comprehensive analysis approach calculates the blade loadings from 2-D (M, α) sectional data or simply lift curve slopes that do not contain information of the chordwise aerodynamic distributions. Such is done at various angles of attack and Mach numbers. Besides, post stall behaviors of the chordwise distribution are not accounted for with the lift curve slope-based formulations. However, chordwise pressure distributions might be generated by the VLM surfaces in CHARM. The provided pressure distributions by CHARM are on sheet panels. Therefore, it was advised that a new methodology that generates pressure distributions on the real geometry of the rotor blades, and several sensitivity investigations of this methodology are performed [30]. The recommended method uses sectional angles of attack and Mach numbers as inputs to the pressure distributions of 2-D airfoil database with regular azimuth steps. In this study, the suggested methodology is improved by a high resolution solution.

Vortex lattice quadrilaterals are used to model bound circulation that satisfies the flow tangency at the collocation points in CHARM. That approach provides the lift on each blade section, and this information is used as input to 2-D look-up tables to find the corresponding angle of attack and drag coefficient at each blade section. However, the regular solution is provided at maximum 240 azimuth steps with increasing computation time. CHARM has an analysis option called reconstruction that captures BVI. This mode increases the azimuthal resolution of the analysis on the regular solution. However, when reconstruction is activated, CHARM does not provide reconstructed angles of attack and Mach numbers, except reconstructed local thrust coefficient. In this study, 36 azimuth steps are used for regular solution and 360 azimuth steps are used for reconstructed solution. Furthermore, 40x100 (chordwise x spanwise)grid blade is used for the pressure distribution due to not lose the fidelity of BVI related change in angle of attack [30].

The approach is introduced in Section 3.4.1 to find reconstructed angles of attack

and Mach numbers, and the methodology of pressure distribution on rotor blades is explained in Section 3.4.2.

3.4.1 Method of Finding Reconstructed Angles of Attack and Mach Numbers, FRAAM

In this section, an approach is explained to find reconstructed angles of attack and Mach numbers from reconstructed thrust coefficients. Thrust coefficient values of desired blade sections are provided by CHARM, and the formulation is given in Equation 3.2.

$$\frac{dc_T}{dr} = \frac{dT}{dr}\frac{2}{\rho(\Omega R)^2 c} \tag{3.2}$$

However, it is required to find angle of attack and Mach values of each blade section to be able to distribute pressure over blade geometry. Firstly, Mach number of each blade section is found by Equation 3.3.

$$M_r = \frac{1}{c_\infty}(\Omega r + V_\infty sin(\psi)) \tag{3.3}$$

2D look-up table of airfoil database takes angles of attack and Mach numbers to provide lift coefficient and drag coefficient. In this reverse problem, it is aimed to get angle of attack by providing Mach number, lift and drag coefficient to 2D look-up table. A combination of lift and drag coefficient provides thrust coefficient and Mach number of desired blade section is found. The combination of lift and drag is illustrated in Figure 3.5 to find thrust and normal force on airfoil.

The thrust and normal force values are found by Equations 3.4 and 3.6, respectively.

$$T = Lcos(\phi) - Dsin(\phi) \tag{3.4}$$

$$c_T = c_L cos(\phi) - c_D sin(\phi) \tag{3.5}$$

$$N = Lcos(\alpha) + Dsin(\alpha) \tag{3.6}$$

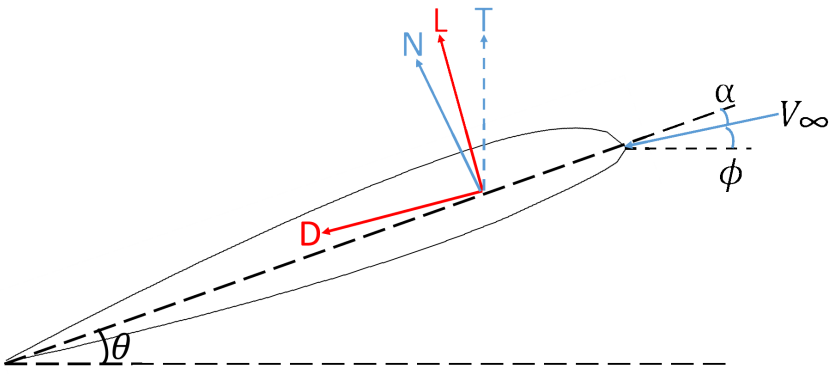

Figure 3.5: Schematic of Airfoil

$$c_N = c_L cos(\alpha) + c_D sin(\alpha) \tag{3.7}$$

θ is the summation of geometric twist and pilot control input.

$$\theta = \theta_{twist} + \theta_{pilot} \tag{3.8}$$

$$\theta_{pilot} = \theta_0 - \theta_{lat} cos(\psi) - \theta_{long} sin(\psi) \tag{3.9}$$

In 2D look-up tables, the lift and drag coefficients are non-dimensionalized by a parameter $2/(\rho(M_r c_\infty)^2 c)$. On the other hand, Equation 3.2 is non-dimensionalized by $2/(\rho(\Omega R)^2 c)$. Therefore, a transformation is required on thrust coefficient data provided by CHARM.

$$\frac{dc_T}{dr} = \frac{dT}{dr} \frac{2}{\rho(\Omega R)^2 c} \frac{(\Omega R)^2}{(M_r c_\infty)^2} \tag{3.10}$$

$$c_T = T \frac{2}{\rho(M_r c_\infty)^2 c} \tag{3.11}$$

By the help of Equation 3.5, 2D look-up tables are converted to thrust coefficient table at each angle of attack and Mach number. Following that, each thrust coefficient provided by the reconstructed results of CHARM is found in the thrust coefficient table with angle of attack and Mach number. This angle of

attack and Mach number are found on blade stations provided by CHARM reconstructed thrust coefficient data, and these blade stations are illustrated in Figure 3.6.

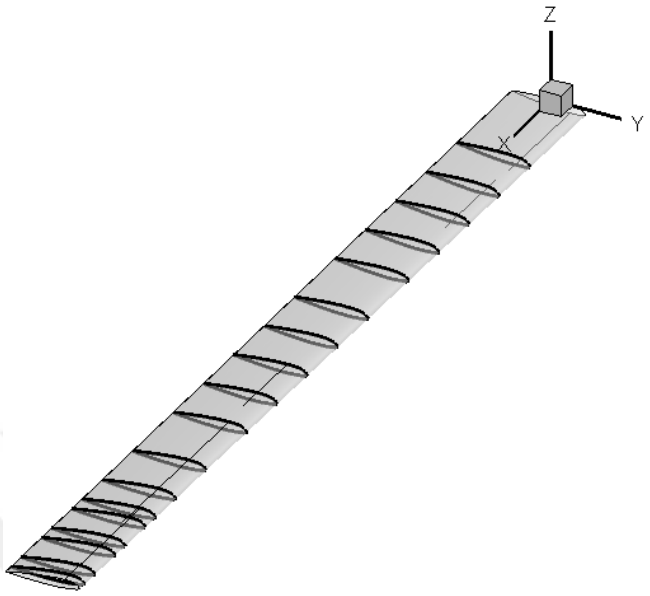

Figure 3.6: Blade stations of reconstructed data

After application of the procedure on each blade station illustrated in Figure 3.6, angle of attack and Mach number information are reproduced for more stations using interpolation and extrapolation methods.

To validate reconstructed angles of attack and Mach numbers, a validation of nondimensional sectional normal force is used at 87%R and shown in Figure 3.7. It is seen that reconstructed angles of attack and Mach numbers predict the BVI centered around $\psi = 50^{o}$ on the advancing side and around $\psi = 300^{o}$ on the retreating side. Prediction of airloads at the advancing side differs from the experiment due to rigid blade modeling and ignoring the wall effect. The mean value of the sectional load is 1.5% less than the mean value of the experiment. Therefore, low frequency contents are well predicted by the suggested methodology to find the reconstructed angles of attack. Additionally, normal force at the advancing side is slightly predicted differently due to instrumentation of experimental blade and rigid blade modeling in CHARM. Furthermore, a comparison is shown in Figure 3.8 by using analysis results from literature [49]. The com-

parison is performed by fluctuations of the nondimensional normal force, which means low frequency content is removed from data, and only high frequency content BVI related is shown. Similarly, normal force at advancing side differs from the experiment for all analyses due to the instrumentation of the experimental blade.

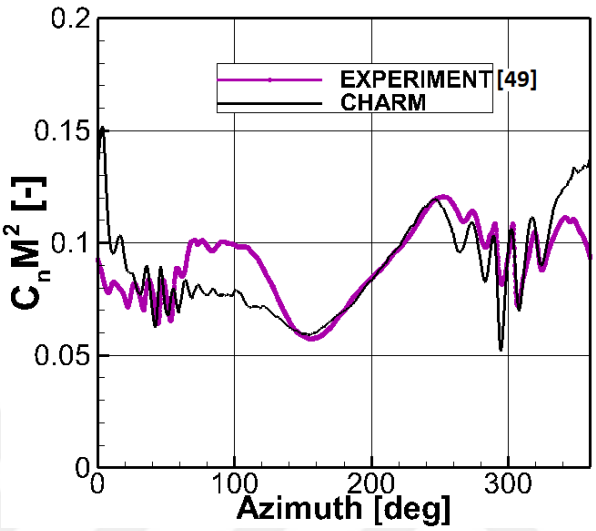

Figure 3.7: Nondimensional sectional normal force at 87% R, experiment data [49]

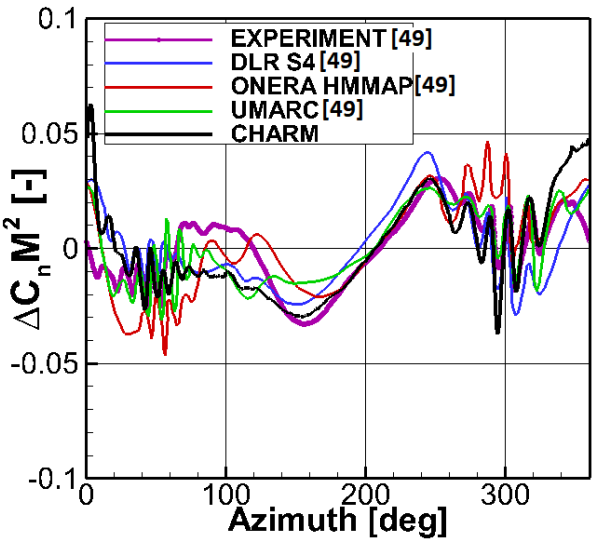

Figure 3.8: Nondimensional sectional normal force mean subtracted at 87% R with various comprehensive analysis tools [49]

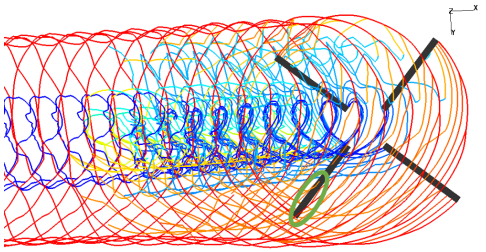

(a) BVI around 50°

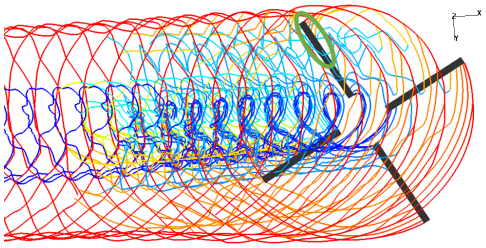

(b) BVI around 300°

Figure 3.9: Visualization of BVIs

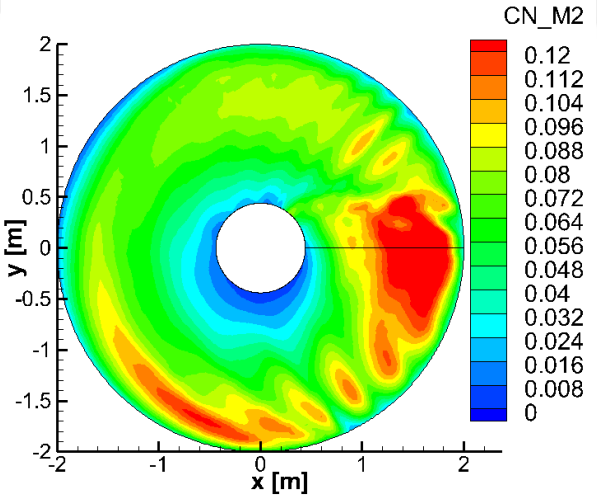

Figure 3.10: Nondimensional sectional normal force on rotor disc

Additionally, the location of the BVIs are visualized with wake geometry in Figure 3.9, and sectional normal force is depicted on a rotor disc for all azimuths in Figure 3.10.

3.4.2 Method of Finding Airfoil Pressure Distribution, FAPD

Reconstructed angles of attack and Mach numbers are calculated at the previous section to distribute pressure on a rotor blade. Preestablished airfoil pressure distribution data of the blade airfoil in several angles of attack and Mach numbers are used for the pressure distribution procedure. This airfoil pressure distribution database is generated by CFD, covers angles of attack from -180 degrees to 180 degrees and Mach number from 0.01 to 0.9. Therefore, available pressure distribution values cover the stall angles, compressible and transition regions. In this approach, effects of the 3D flow such as yawing speed and stall delay are neglected. However, it is stated that rotational flow effects do not change the pressure distribution dramatically [50]. Lastly, the rotor module of CHARM that contains rotor geometry and blade dynamics is used to generate rotor simulation for TACO. The procedure may be summarized as follows;

i. Blade geometry generation in blade axis.

ii. Reconstructed angles of attack and Mach numbers found in Section 3.4.1 are extrapolated and interpolated into desired blade sections illustrated in Figure 3.11.

iii. Sectional airfoil pressure distribution is obtained for each desired blade section with the reconstructed angle of attack and Mach number from the airfoil pressure database. An example is shown in Figure 3.12.

iv. The above procedure is performed azimuthwise.

The pressure distribution of each cell on the blade is multiplied by unit normal vector of the cells, and integrated over the each blade of the rotor to find the hub forces. After performing the integration procedure for each azimuth, another validation is performed with the hub force in the Z direction of the non-rotating hub axis in Figure 3.13.

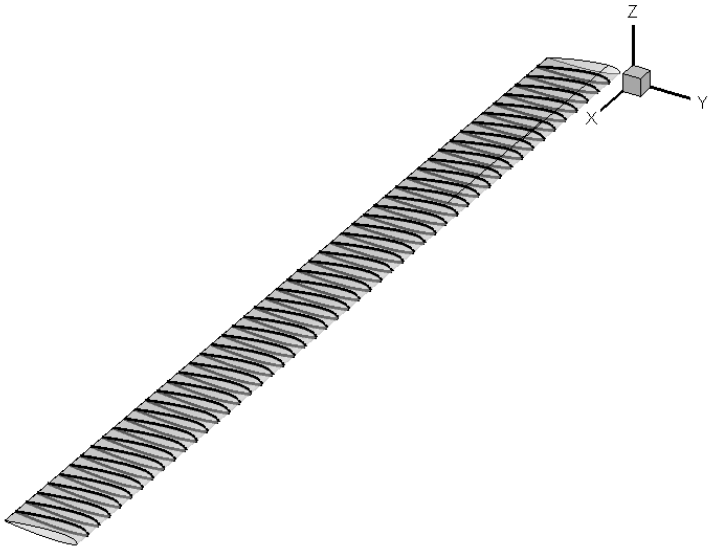

Figure 3.11: Extrapolated and interpolated blade stations of reconstructed angles of attack and Mach numbers

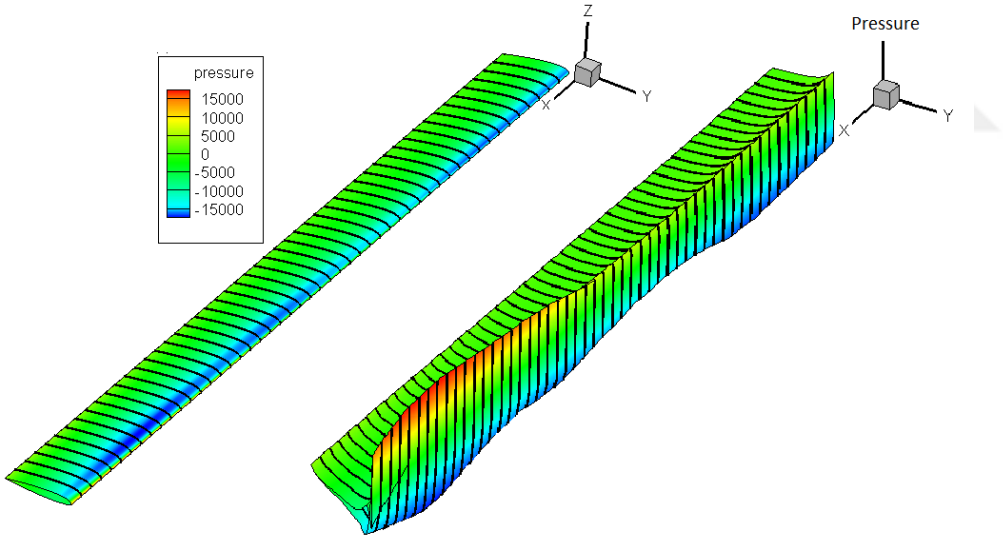

Figure 3.12: Pressure Distribution on Blade

This comparison is performed with data from the regular solution of CHARM and the proposed methodology. Low frequency content of hub load is quite similar for both. However, FAPD predicts high frequency content by BVIs due

to reconstructed angle of attack and Mach. This comparison shows that the suggested methodology does not lose low frequency when overall pressure is integrated. The effects of BVIs are observed from 25° to 55° and around 90°.

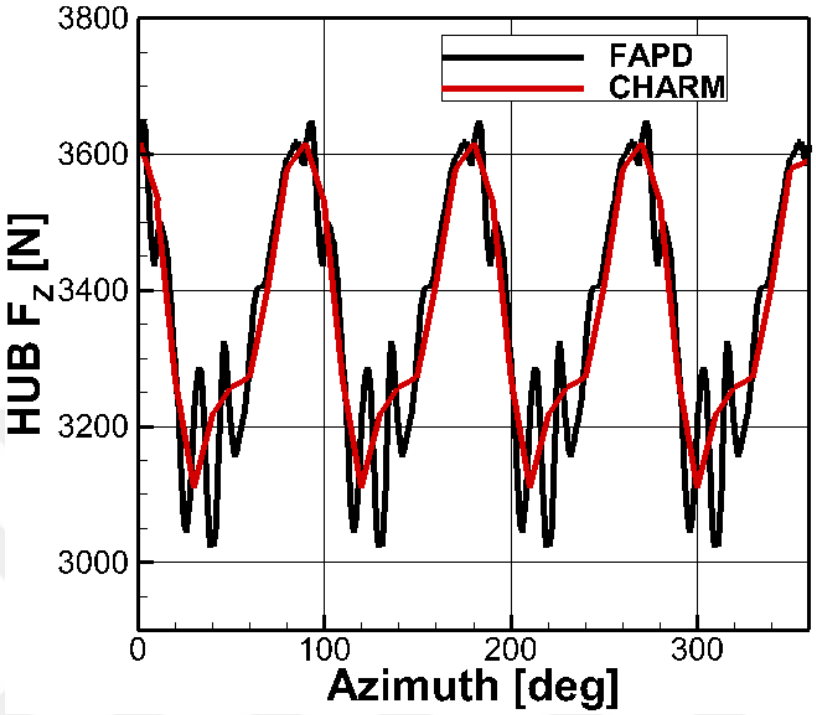

Figure 3.13: Hub Force Comparison between CHARM and FAPD

3.4.3 Aeroacoustic Validation

Lastly, total acoustic pressure is used to validate the proposed methodology. The azimuthal motion of one blade with pressure distribution is given as input to TACO. It has the ability to reproduce the remaining blades. The microphone is located under the rotor and advancing side due to catch the maximum peak of the noise contour [48].

Acoustic solution is provided by acoustic solver (TACO) at the microphone location given in Figure 3.14. Total acoustic pressure is compared with the test result and illustrated in Figure 3.15. The result indicates that the acoustic signals are well captured by the proposed methodology in 3.4.2.

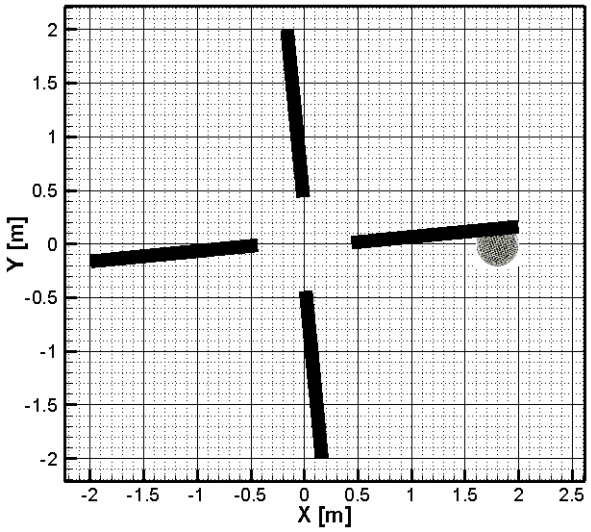

Figure 3.14: Location of microphone at advancing side

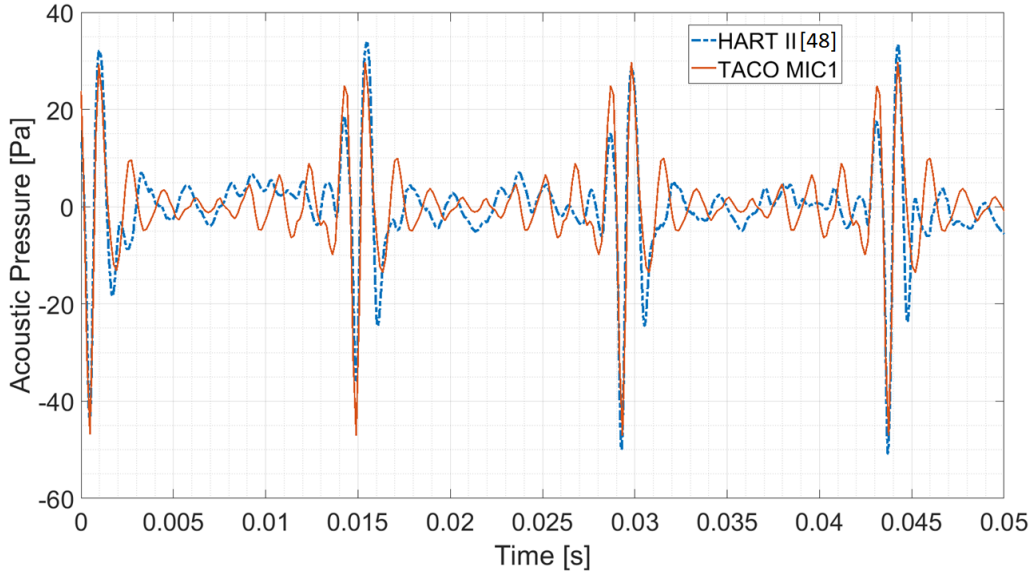

Figure 3.15: Total acoustic pressure comparison of HART II, test data [48]

CHAPTER 4

AERODYNAMIC AND AEROACOUSTIC EVALUATION OF TAIL ROTOR

In this chapter, different tail rotor configurations are investigated. Firstly, mathematical model for the helicopter is introduced. Then, investigation of a conventional tail rotor (CTR) configuration is carried out with different turn directions. In these initial computations, tail rotor is evaluated for both isolated and with full helicopter trim analysis. Finally, a scissors type tail rotor (STR) is introduced and investigated for assessing the effects of the scissors angle and vertical distance between rotors on the aerodynamic and aeroacoustic characteristics with full helicopter trim analysis. All of the studies are performed at three different flight conditions: forward flight, hover, and quartering flight.

4.1 Mathematical Model and Flight Conditions

Sample 10-ton class helicopter is modeled and the tail rotor blade of this sample helicopter has a rectangular planform as illustrated in Figure 4.1, and the specifications of the rotor are given in Table 4.1.

Initially, velocity sweep analyses are performed. The computed longitudinal cyclic, collective, pitch angle, and total required power curves with airspeed are illustrated in Figure 4.2.

Three different flight conditions were selected in this study. They are;

i. Forward flight with transition speed (80 knots)

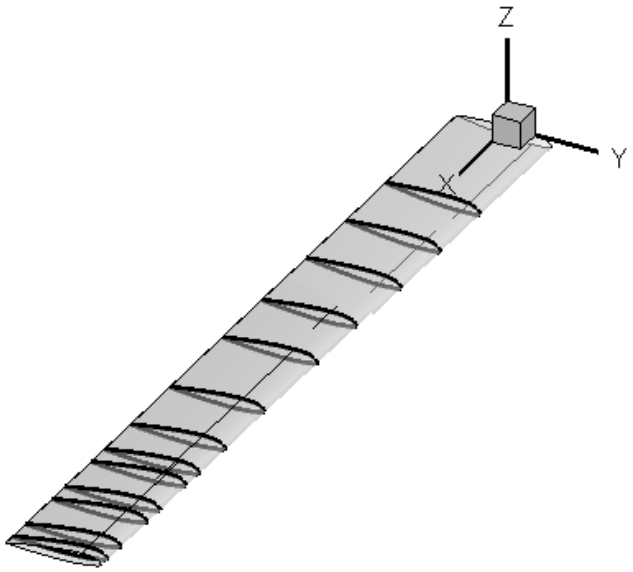

Figure 4.1: Tail Rotor Blade

Table 4.1: Tail Rotor Model Properties

Parameter	Value	Unit
Rotor Radius	1.9	m
Blade Chord	0.3	m
Linear Twist	4.5	deg
Number of Blades	4	-
Root Cutout	0.55	m
Rotational Speed	1100	rpm
Airfoils	NACA23012	-

ii. Hover

iii. Quartering flight with 30 degree sideslip angle (60 knots)

Forward and quartering flight conditions are selected because these are maneuvers in which the main rotor wake highly interacts with the tail rotor [3]. On the other hand, the tail rotor is not affected significantly by the main rotor wake in hover condition [4]. Therefore, with these maneuvering flight conditions, it is aimed to study the potential effects of the main rotor on the tail rotor. Addi-

tionally, Representative wake geometries are illustrated in Figure 4.3

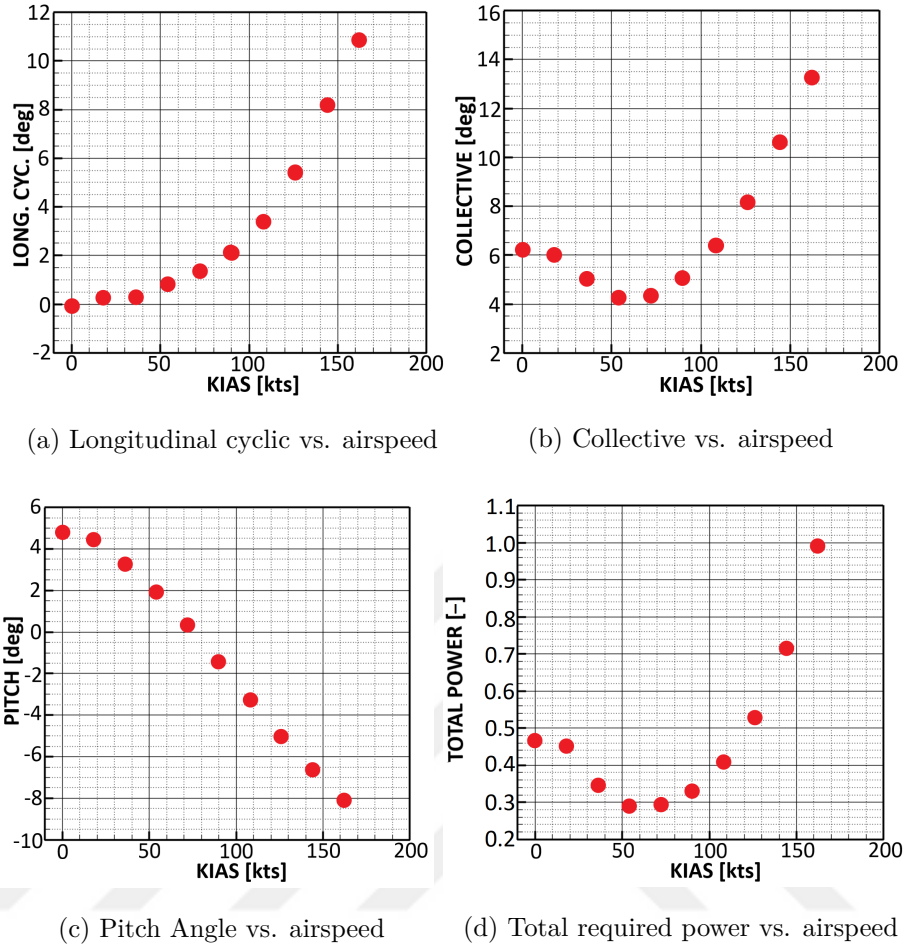

(a) Longitudinal cyclic vs. airspeed

(b) Collective vs. airspeed

(c) Pitch Angle vs. airspeed

(d) Total required power vs. airspeed

Figure 4.2: Full helicopter model validation

4.2 Conventional Tail Rotor

Tail rotors function as anti-torque generators to compensate the main rotor torque. Commonly, a rotor with smaller dimension than the main rotor is implemented at tail, and this is called conventional tail rotor. Conventional tail rotors might be modeled with different rotation directions, such as top-forward (TF) turn and bottom-forward (BF) turn directions. In this part, effects of main rotor interaction on tail rotor and effects of turn direction are studied for tail rotor interacting with the main rotor situation, at flight conditions as mentioned

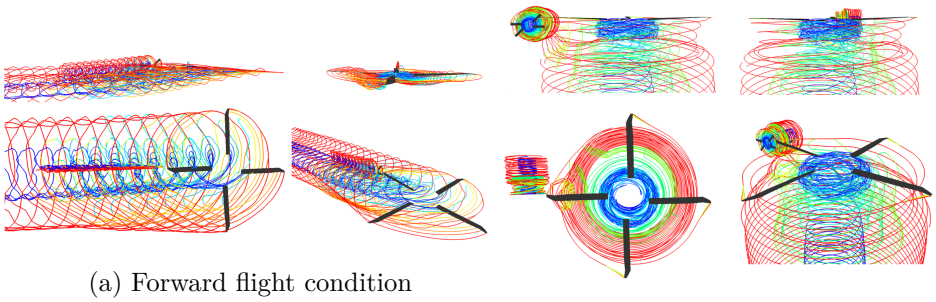

(a) Forward flight condition

(b) Hover condition

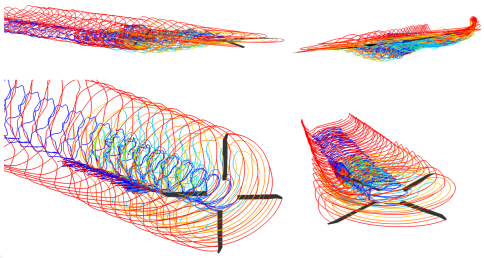

(c) Quartering flight condition

Figure 4.3: Wake geometry visualization of selected flight conditions

earlier. The results of these studies are assessed in terms of aerodynamics and aeroacoustics.

The positions of the rotors and rotation directions are illustrated in Figure 4.4 for better understanding of the airflow on tail rotor.

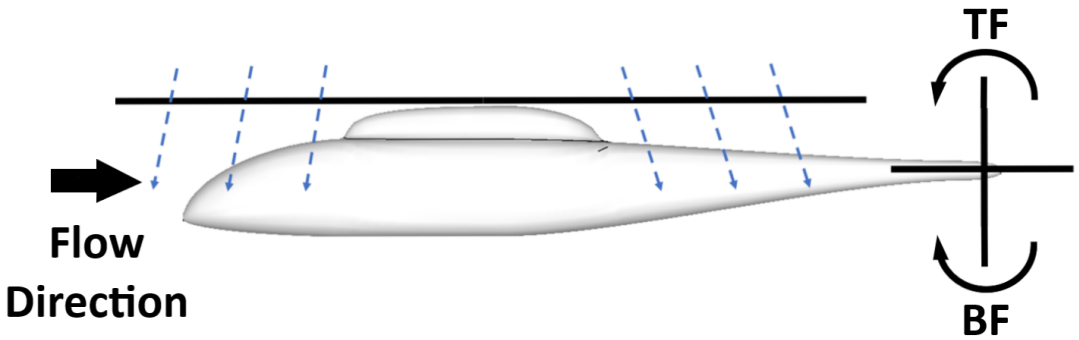

Figure 4.4: Position of rotors and rotation directions

4.2.1 Aerodynamics

In this part, aerodynamic properties such as performance, angle of attack, non-dimensional normal force, and non-dimensional peak to peak thrust are investigated due to rotation direction and main rotor wake interaction.

The tail rotor requires less power than the main rotor. Nevertheless, the tail rotor moment in rotation direction is an important input to design, and the tail rotor power contributes to the total power requirement. Variations of non-dimensional required power by rotation direction and main rotor interaction are depicted in Figure 4.5 for all three flight conditions. Required power values are non-dimensionalized by the isolated tail rotor power for each flight condition.

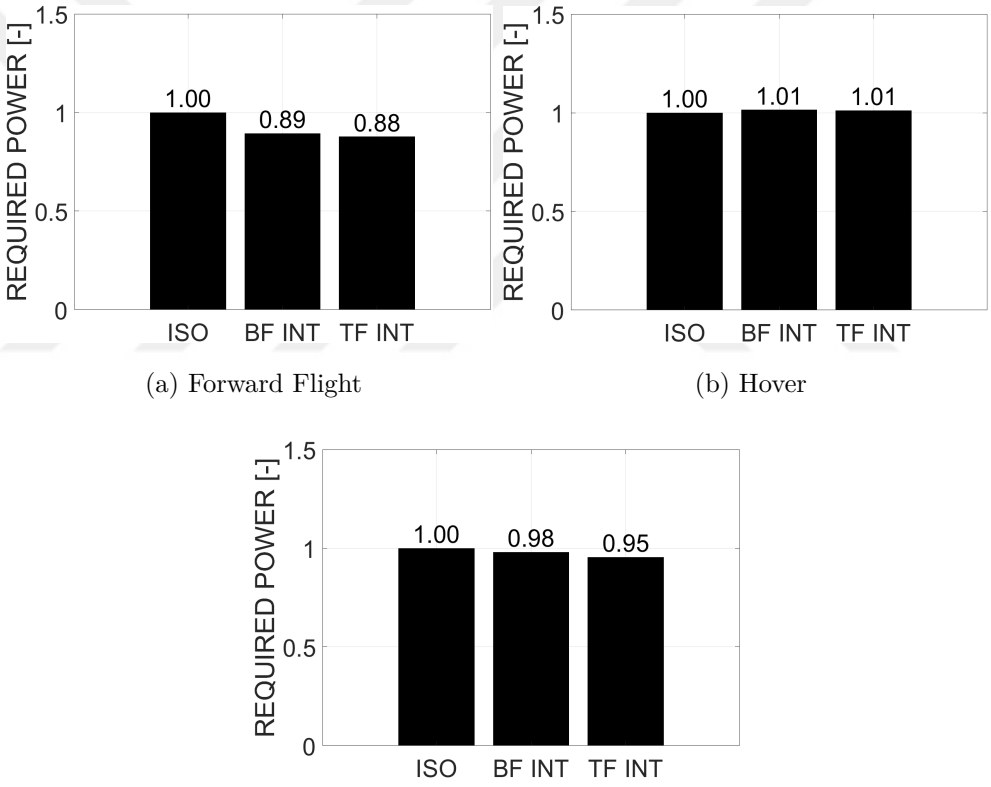

(a) Forward Flight

(b) Hover

(c) Quartering flight

Figure 4.5: Non-dimensional required power for various configurations and flight conditions

It is apparent from the results main rotor wake decreases the required power of

the tail rotor for forward flight condition more than 10%. Similarly, interaction decreases the required power 2% and 5% at quartering flight condition for the BF and TF rotation directions, respectively. On the other hand, the effect is 1% on hover condition. The interaction effect of the main rotor is thus negligible for hover condition in evaluating the required power.

Next, variations of angle of attack and non-dimensional normal forces are illustrated on a rotor disc. A sample representation of contour figures on disc template is shown in Figure 4.6.

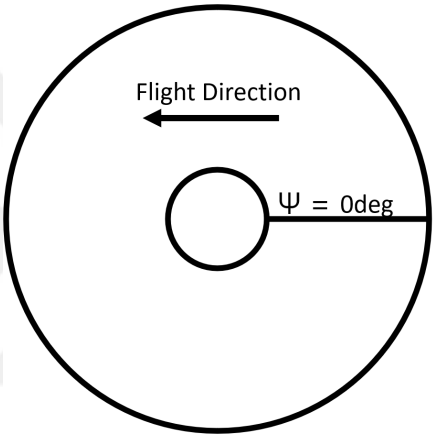

Figure 4.6: Template of disc contour

Variations of the angle of attack draw a general map to evaluate flow over airfoil sections. Angles of attack are compared for introduced tail rotor configuration at three different flight conditions and depicted in Figures 4.7 to 4.9.

The results indicated that forward and quartering flight conditions are significantly affected by both rotation direction and the existence of main rotor wake interaction. Self and main rotor BVI based oscillations are well seen for forward flight at all configurations. Hover condition is slightly affected by the main rotor wake, and interacted configurations have similar airflow over the rotor.

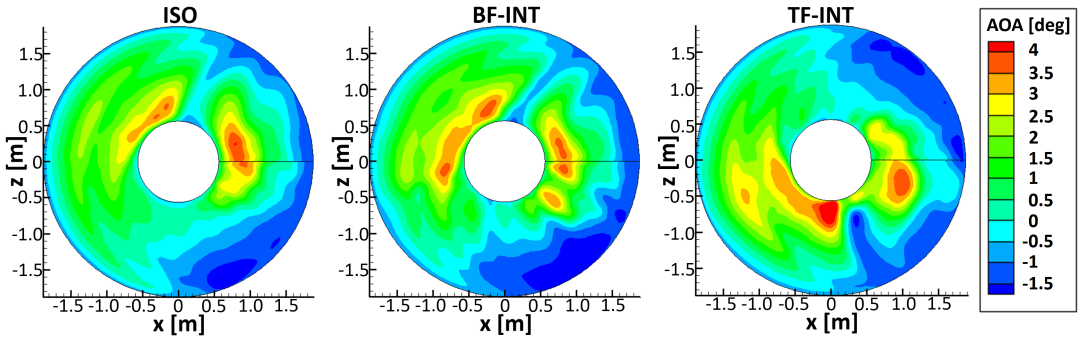

Figure 4.7: Forward Flight - Angle of attack

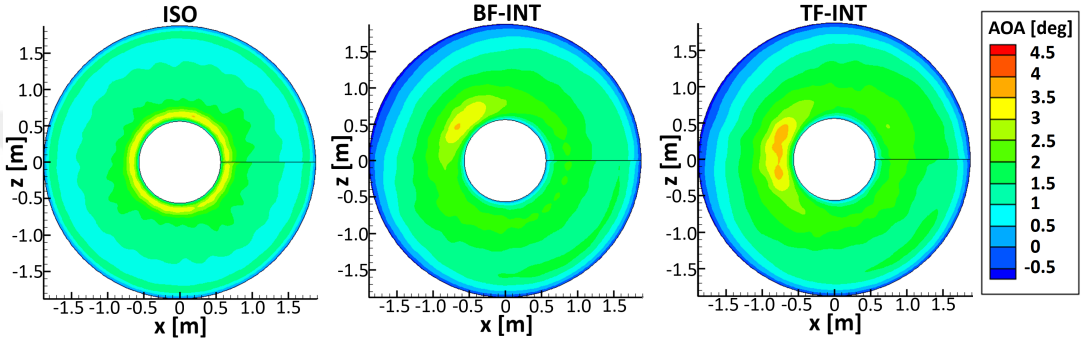

Figure 4.8: Hover - Angle of attack

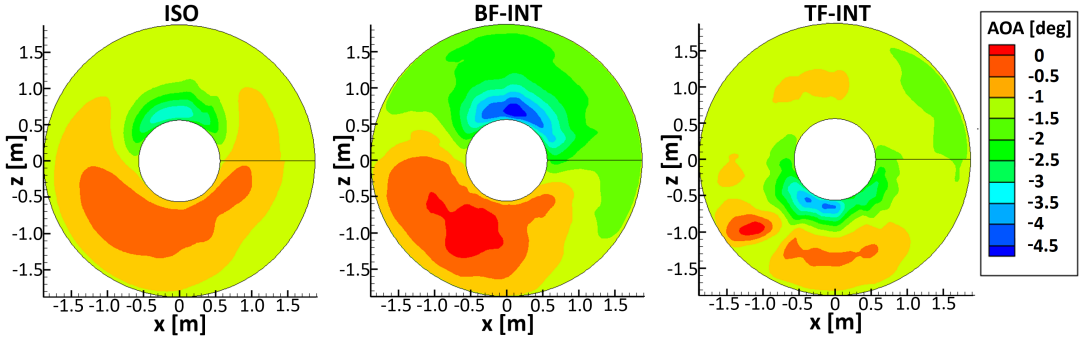

Figure 4.9: Quartering Flight - Angle of attack

Non-dimensional normal force contour gives extra information on how the sectional forces are affected by rotation direction and main rotor wake interaction. Illustration of non-dimensional normal force contour on rotor disc is given in Figures 4.10 to 4.12. As in angle of attack contours, forward and quartering flight conditions are significantly affected by the rotation direction and main

rotor wake. Main rotor wake interactions are well seen by the BVI at BF rotation direction in forward flight condition. Isolated tail rotor gives similar non-dimensional normal force contour, and interaction of main rotor wake slightly changes the non-dimensional normal force at hover condition.

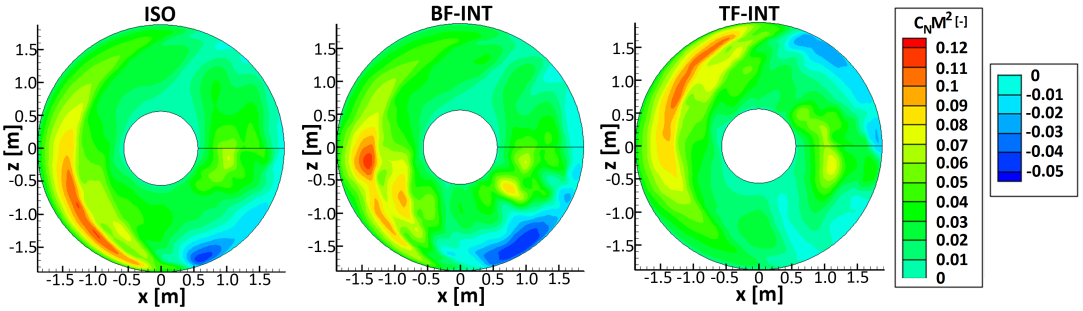

Figure 4.10: Forward Flight - Non-dimensional normal force

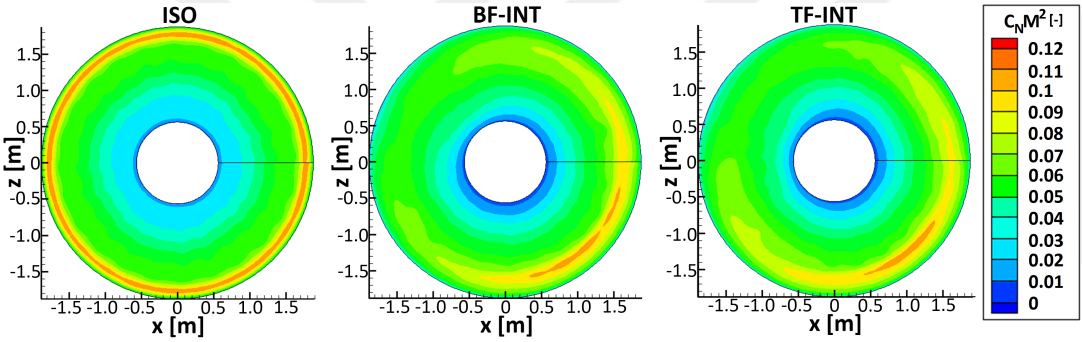

Figure 4.11: Hover - Non-dimensional normal force

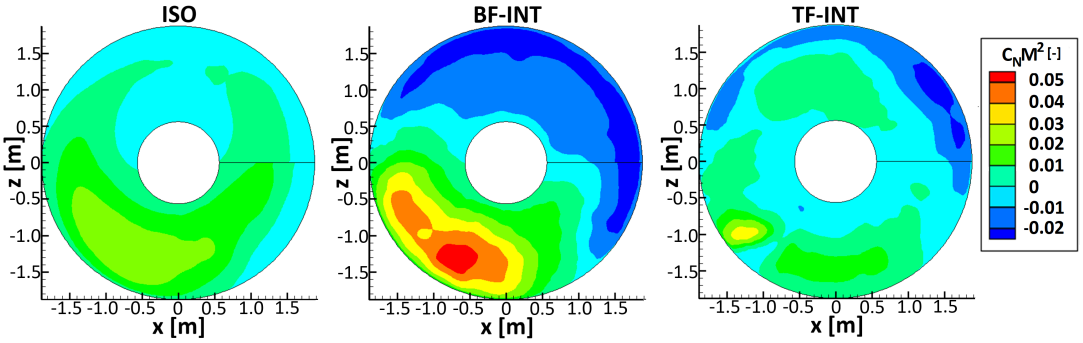

Figure 4.12: Quartering Flight - Non-dimensional normal force

Peak to peak oscillations are illustrated in Figure 4.13. Findings show that peak

to peak thrust values are non-dimensionalized by peak to peak thrust value of isolated tail rotor for each flight condition. Certainly, interaction increases oscillations on thrust. Hover condition is less affected flight conditions for oscillatory thrust. BF tail rotor configuration at forward flight has 0.8 times extra oscillation than oscillation of isolated tail rotor. 1.81 times extra oscillation value is observed in TF tail rotor configuration at quartering flight.

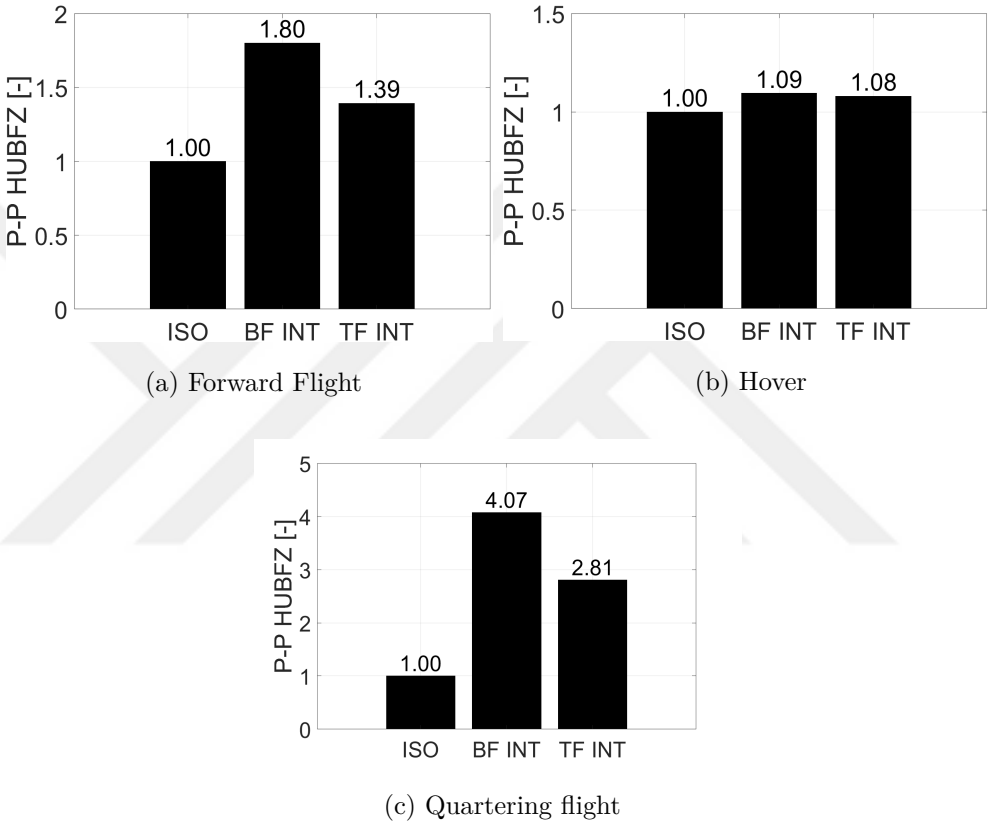

(a) Forward Flight

(b) Hover

(c) Quartering flight

Figure 4.13: Peak to peak non-dimensional thrust for various configurations and flight conditions

Aerodynamic evaluation of the conventional tail rotor indicates that main rotor has a great influence on aerodynamics behavior of the tail rotor at forward and quartering flight conditions.

4.2.2 Aeroacoustics

Aeroacoustic evaluation of tail rotor with rotation direction and main rotor wake interaction is introduced in this part. The comparison focuses on loading, thickness, and total acoustic pressure and sound pressure level (SPL) on vertical and horizontal plane microphone grids. An illustration of the microphone grids is given in Figure 4.14. These grids are 10 meters by 10 meters with 121 microphones in each grid, and they are 4 meters away from the rotor.

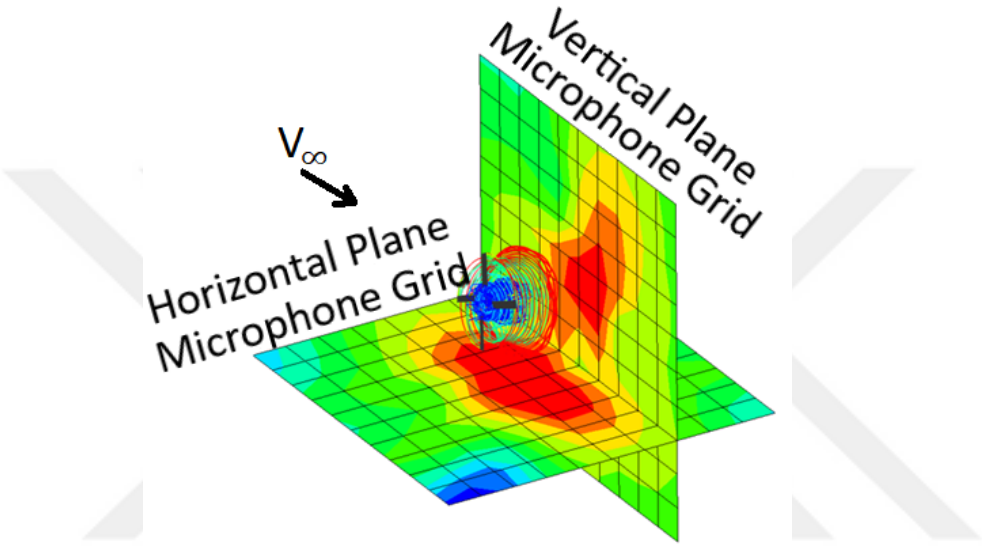

Figure 4.14: Visualization of microphone grids

The aim of measuring the noise on two planes is to study different effects of the loading and thickness noise. General directivity of helicopter noise sources are illustrated for main rotor in Figure 4.15. Similarly, the loading noise of the tail rotor is radiated in the direction of the vertical plane grid, and the thickness noise of the tail rotor is radiated in the direction of the horizontal plane grid. Therefore, radiation of thickness noise on the vertical plane grid is not implicitly investigated.

Loading, thickness, and total acoustic pressure are examined for isolated and main rotor interacted tail rotor configurations.

Effect of rotation direction is depicted in Figure 4.16. Results point that change in rotation direction directly affects the loading noise because of the change of

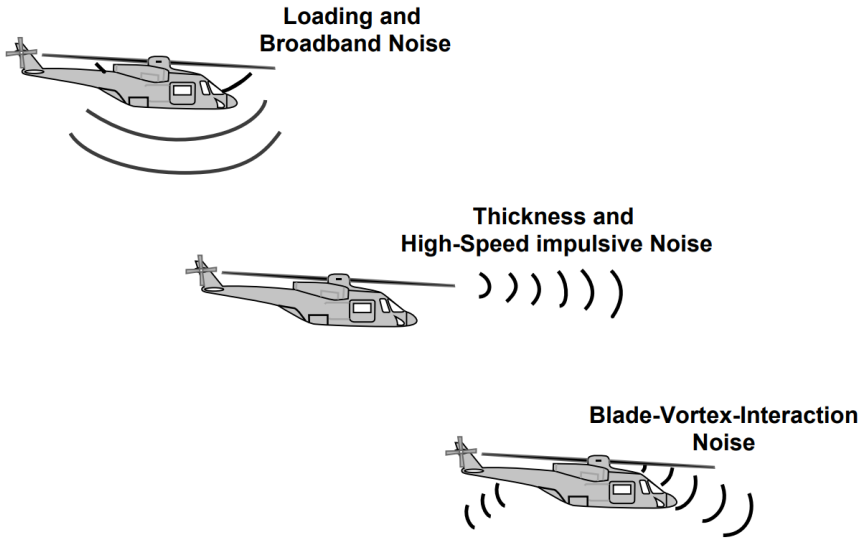

Figure 4.15: Typical direction of primary radiation of various main rotor noise sources [51]

aerodynamic behavior. Even the geometry of the blade is the same, thickness noise changes. The reason behind it, the signals received by microphones are changed. Total acoustic pressure differs due to change in loading and thickness noise.

The main rotor wake interaction of tail rotor noise is shown in Figure 4.17. Thickness noise is generated by the geometry of the blade and deflections, and interaction affects only aerodynamic behavior. However, elastic deformations are neglected, and tail rotor blades are modeled as a rigid blade. Therefore, findings show that thickness noise remains the same for both tail rotor configuration while loading acoustic pressure differs. Since loading acoustic pressure changes, total acoustic pressure also changes.

Comparison of the rotation direction and main rotor wake interaction using acoustic pressure shows the effect on only one microphone. Further investigations are held on using sound pressure level (SPL) on horizontal and vertical plane microphone grids.

SPL is a measurement of absolute sound pressure against a reference level of sound, measured in decibel. Conversion from acoustic pressure to SPL is given

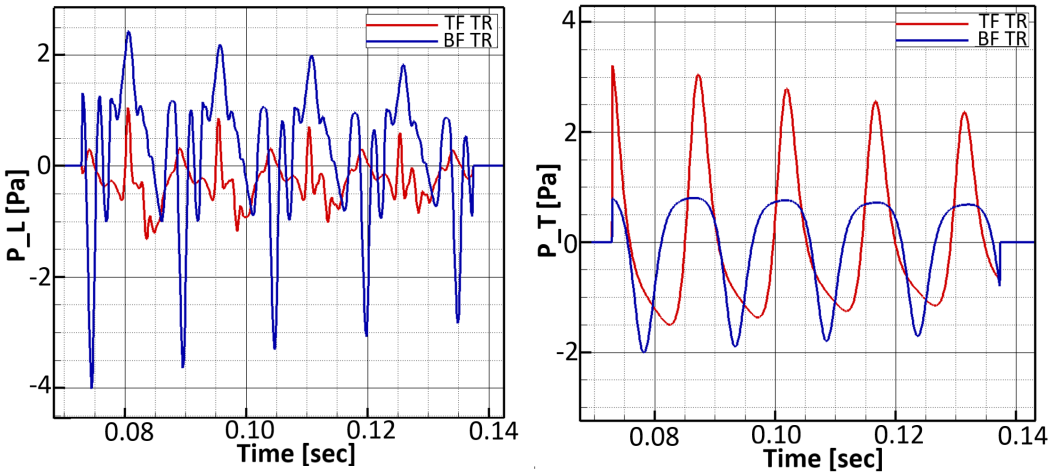

(a) Loading noise

(b) Thickness noise

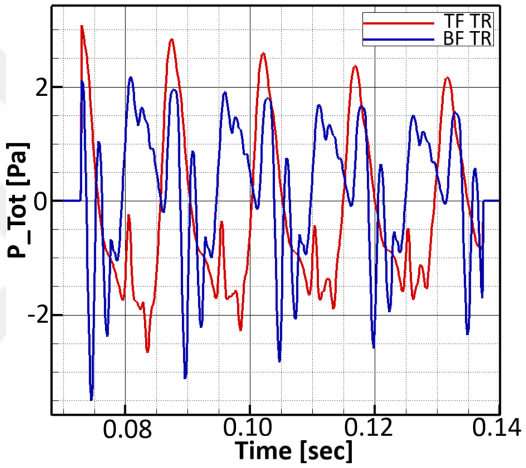

(c) Total noise

Figure 4.16: Acoustic pressure comparison of BF and TF rotation direction

in Equation 4.1.

$$SPL = 20log_{10}\frac{P'_{rms}}{P_{ref}} \tag{4.1}$$

P'_{rms} is the root mean square of the sound pressure. P_{ref} is the reference pressure, $2\times10^{-5}Pa$. The measured sound pressure level is calculated at each microphone location, and the SPL values are contoured on the microphone grip planes.

The comparisons are illustrated on a contour plane for each configuration for

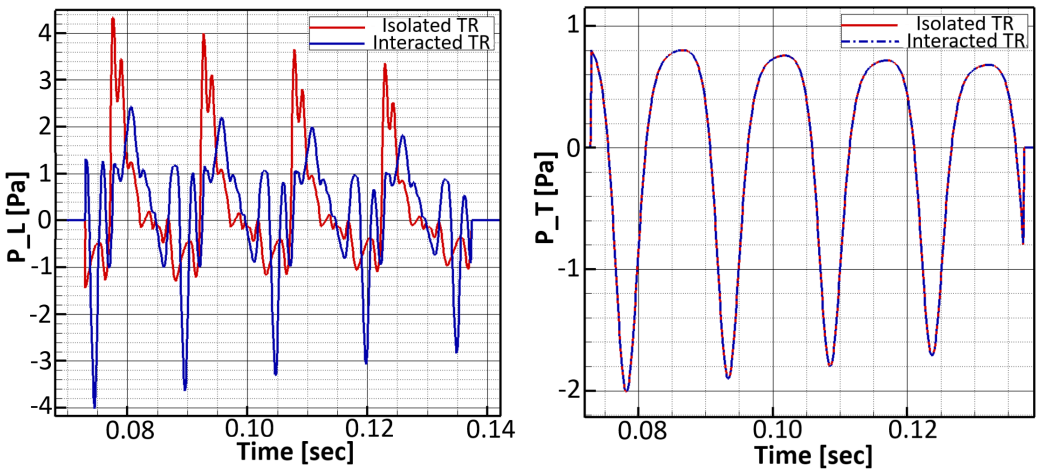

(a) Loading noise

(b) Thickness noise

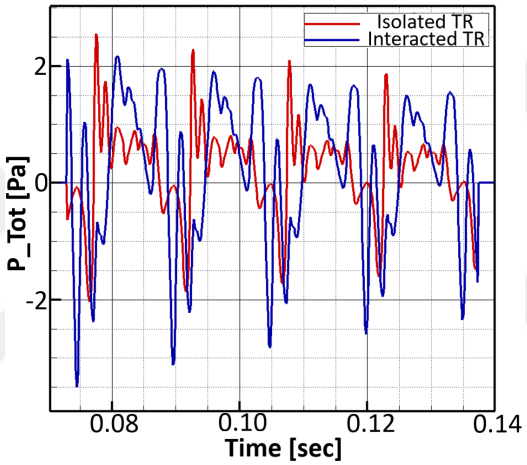

(c) Total noise

Figure 4.17: Acoustic pressure comparison of main rotor wake interaction

forward flight condition in Figure 4.18. The main rotor wake interaction is compared with BF configuration. Findings indicated that the interacted tail rotor has an increment in loading noise and total noise due to changes in pressure oscillation on blade surfaces. These increments can be evaluated by the area of 112dB for loading noise and 114dB for total noise on vertical plane. However, thickness noise remains similar because of the rigid blade modeling. Therefore, deflections are neglected, and geometrically interacted and isolated tail rotors are identical in flight condition. In the evaluation of rotation direction, similar noise characteristics are observed for BF and TF configuration on the vertical

plane due to pure aerodynamic effects. The noise of BF configuration is greater than noise on the vertical plane for TF configuration due to BVIs mentioned before in aerodynamic investigation, and it might be evaluated by the maximum sound pressure level area of the both configurations. However, significant changes are observed for rotation direction investigation on the horizontal plane grid. The advancing side of BF configuration is close to the horizontal plane. However, the retreating side of TF configuration is near to the horizontal plane. Therefore, the blades suffer from different velocity components when blades are near to horizontal plane. Therefore, loading noise, thickness noise, and total noise show different noise characteristics. It is easily seen for both configurations that loading noise and thickness noise are both effective at total noise on the horizontal plane.

The comparisons are illustrated on a contour plane for each configuration for hover condition in Figure 4.19. Similarly, in aerodynamics properties, tail rotor noise is not affected significantly for each tail rotor configuration. The maximum sound pressure level areas are similar for each tail rotor configuration for both vertical and horizontal plane. In this condition, there is no retreating or advancing side for blade due to the absence of free stream velocity. Therefore, similar noise characteristics are observed for three tail rotor configurations.

The comparisons are illustrated on contour planes for each configuration at quartering flight condition in Figure 4.20. Similar to forward flight condition, the interaction of the main rotor increases loading and total noise of the tail rotor. However, thickness noise on the horizontal plane is not affected by the main rotor interaction due to rigid blade modeling. Aerodynamic effects on noise may be evaluated on the vertical plane for effects of rotation direction. BF configuration is superior to TF configuration on the vertical plane for both loading and total noise. In other words, BF configuration generates less loading noise than TF configuration on the vertical plane. However, rotor blades close to the horizontal plane interact with different velocity components for BF and TF configuration similar to forward flight. Therefore, BF configuration generates more thickness noise than TF configuration.

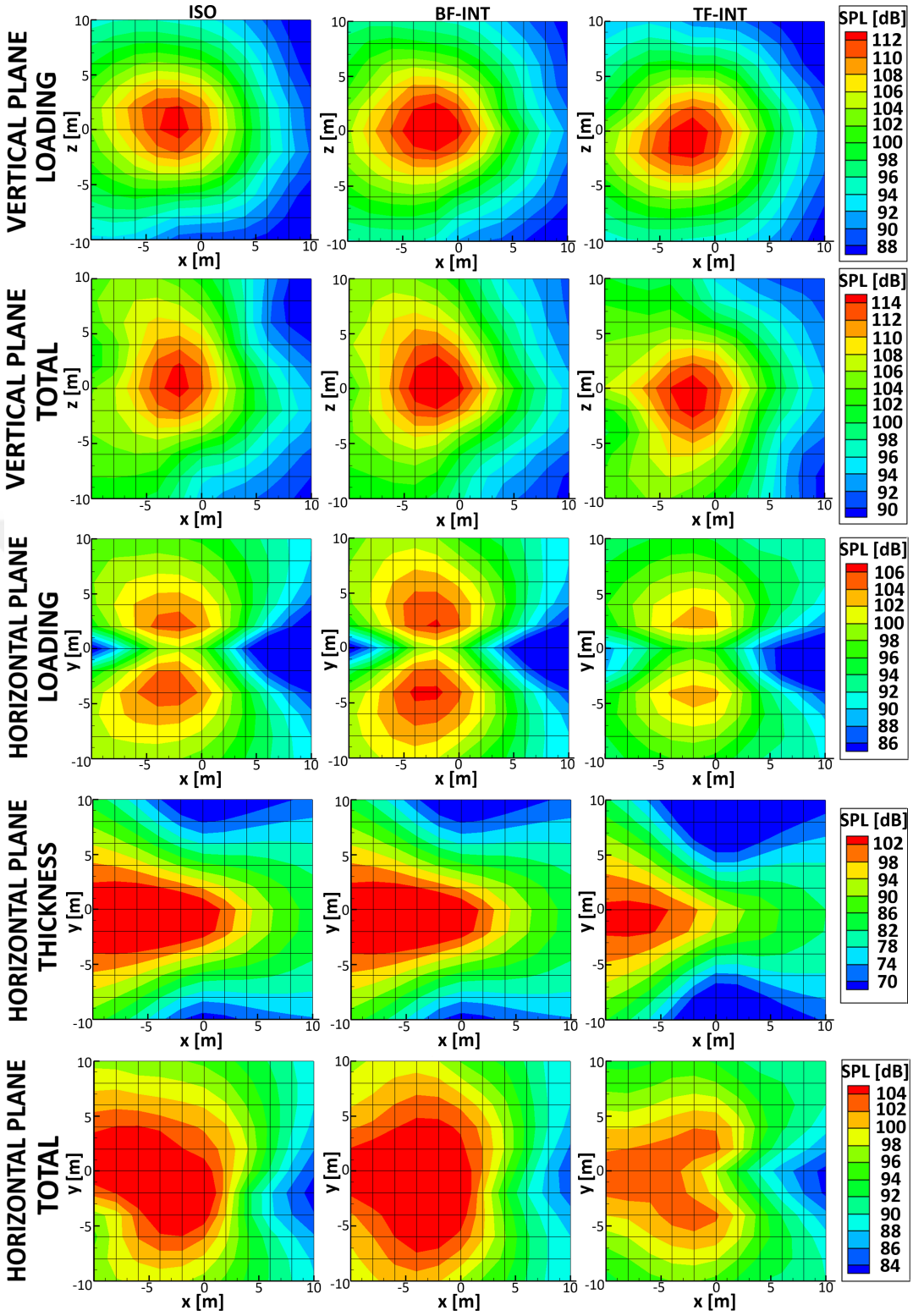

Figure 4.18: Effects of main rotor interaction and rotation direction for forward flight condition on microphone grids

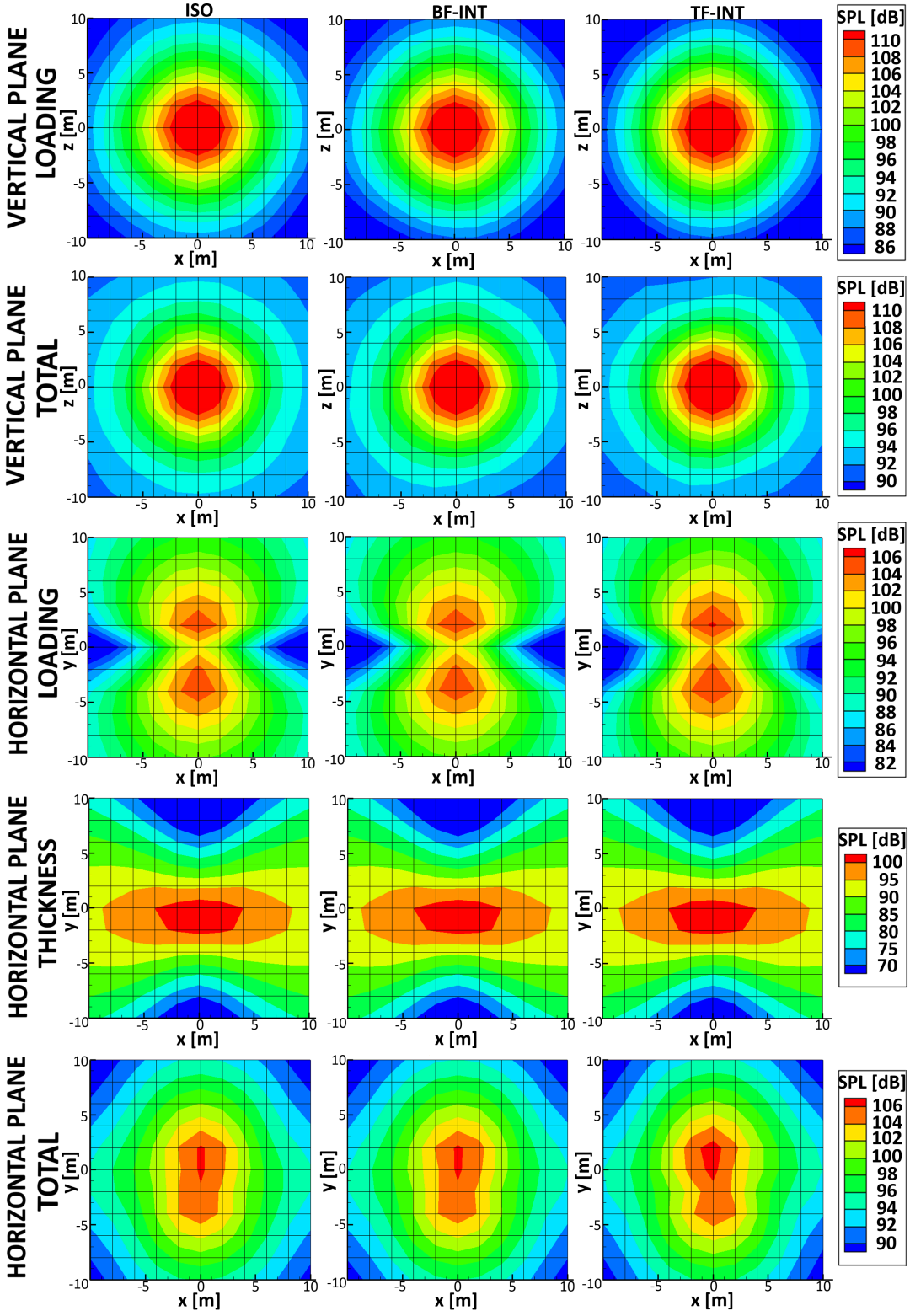

Figure 4.19: Effects of main rotor interaction and rotation direction for hover condition on microphone grids

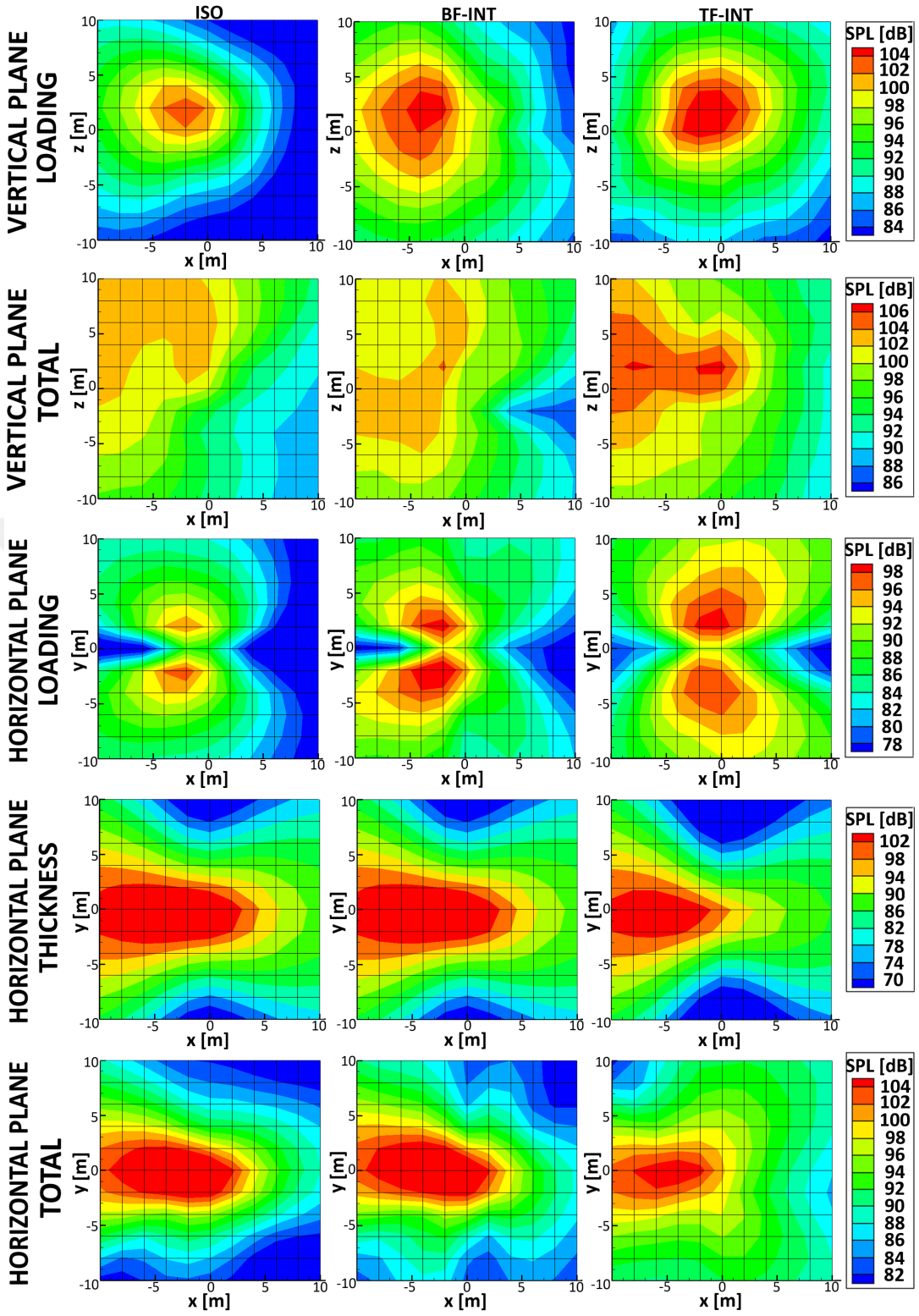

Figure 4.20: Effects of main rotor interaction and rotation direction for forward flight condition on microphone grids

Study on conventional tail rotor shows that main rotor wake effects aerodynamic behavior and acoustic signature of tail rotor, significantly. Additionally, rotation direction plays an essential role in tail rotor noise evaluation at forward and quartering flight conditions. Previous studies on the rotation direction of tail rotor state that BF configuration has better directional controllability and adverse pedal gradients than TF configuration [1,52]. Therefore, BF configuration with main rotor wake interaction configuration is selected for further evaluation of the tail rotor.

4.3 Scissors Tail Rotor

Scissors tail rotor is used for anti-torque to compensate the main rotor torque. The difference from the conventional tail rotor is the angle between blades. This angle is different from 90^o. Scissors tail rotors are generally made by two rotors with two blades, and their hub center collides. This part of the study investigates the effects of the scissors angle and vertical distance on aerodynamics and aeroacoustics signature at forward flight, hover, and quartering flight conditions. Analysis of scissors tail helicopter is performed using full helicopter trim and BF configuration.

Scissors tail rotor configuration has two design parameters, vertical distance, and scissors angle. Firstly, the effect of vertical distance is investigated in terms of aerodynamics and aeroacoustics. Then, the scissors angle is evaluated.

4.3.1 Vertical Distance

Vertical distance is a parameter that defines how the rotors are far from each other in z direction of the hub axis, illustrated in Figure 4.21. Three different distances are used in the investigation and tabulated in Table 4.2

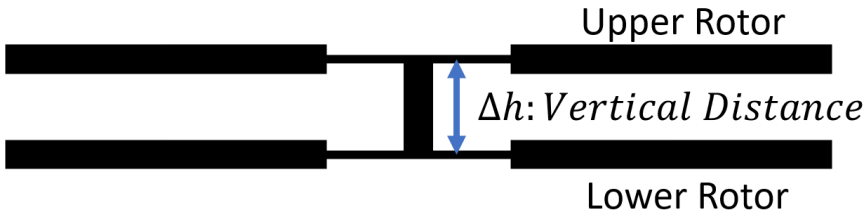

Figure 4.21: Vertical Distance

Table 4.2: Vertical Distance

Vertical Distance	Value	Explanation
CTR	0 [m]	no vertical distance between two rotors
0.1R	0.19 [m]	lower rotor is 0.19 meter far from the upper rotor
0.2R	0.38 [m]	lower rotor is 0.38 meter far from the upper rotor

4.3.1.1 Aerodynamics

Evaluation of required power is given as a bar chart in Figure 4.22 for introduced vertical distance cases at forward flight, hover, and quartering flight conditions. The required power for each tail rotor configuration is non-dimensionalized by the required power value of the conventional tail rotor at each flight condition.

The results indicated that 0.1R vertical distance increases the required power %1 while 0.2R vertical distance decreases the required power %2 at hover condition. 0.1R vertical distance does not affect the required power at forward and quartering flight conditions. On the other hand, 0.2R vertical distance decreases the required power of tail rotor %1 at forward flight, contrarily increases the required power %1 at quartering flight. No correlation might be mentioned for hover condition. Increasing required power correlation exists with increasing vertical distance at quartering flight condition. Decreasing required power correlation is seen with increasing vertical distance at forward flight condition.

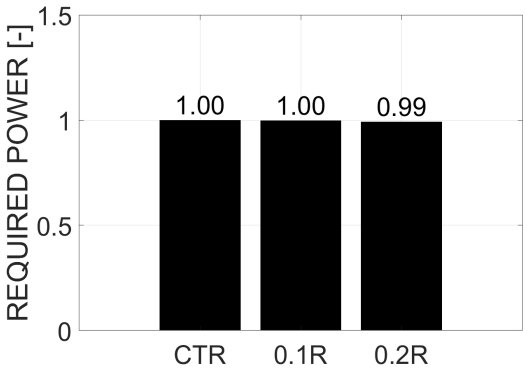

(a) Forward Flight

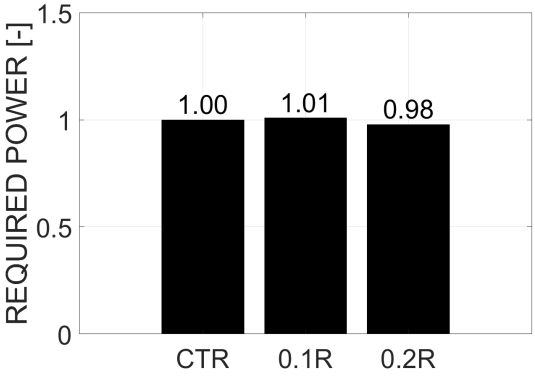

(b) Hover

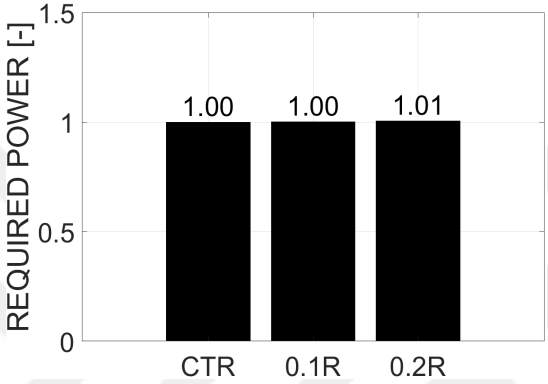

(c) Quartering Flight

Figure 4.22: Non-dimensional required power for various vertical distance at different flight conditions

Angle of attack variations are shown in Figure 4.23 at forward flight condition. It is observed that aerodynamic behavior stays similar with increasing vertical distance. However, the magnitude of the angles of attack is increased on the left half of the tail rotor disc due to change in BVI locations. BVI based oscillations are reduced with the increasing vertical distance in the right half of the tail rotor.

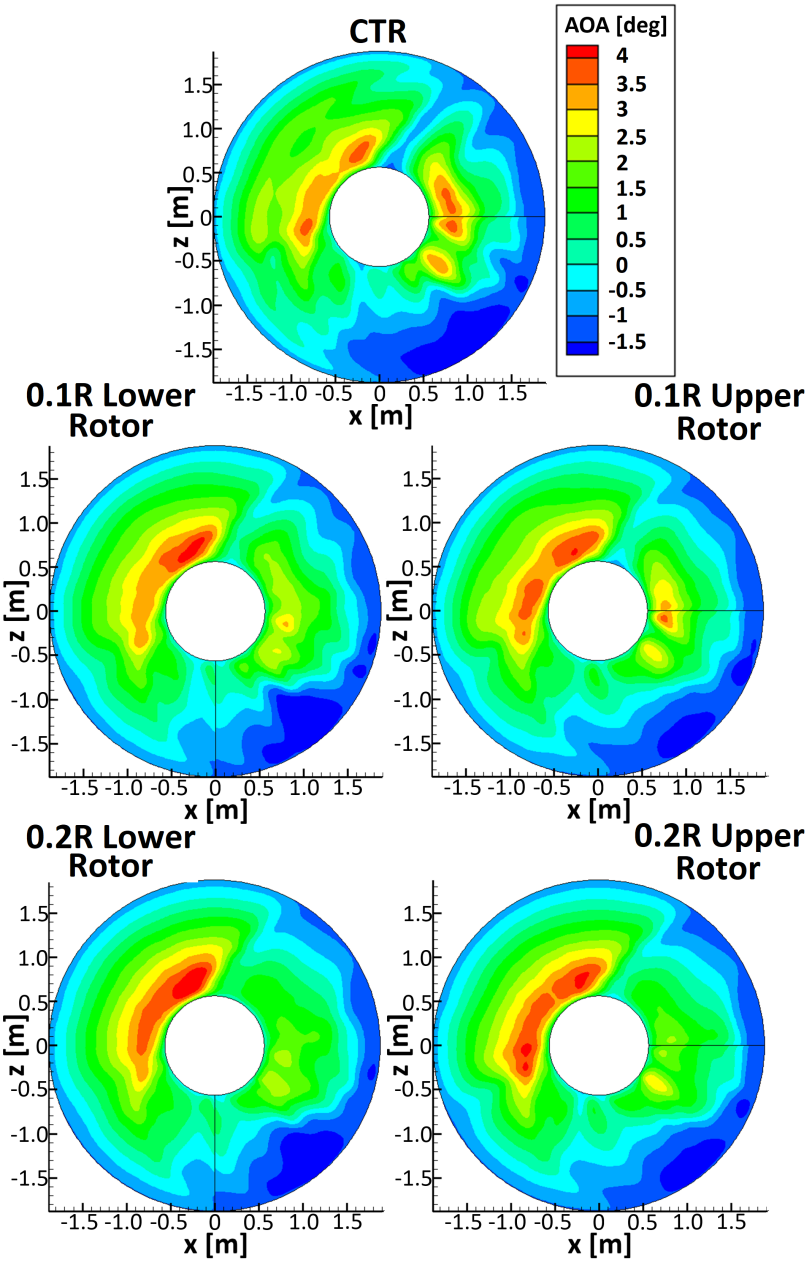

Figure 4.23: Angle of attack contour on disc for various vertical distance at forward flight condition

The angle of attack variations of hover condition are illustrated on a rotor disc in Figure 4.24. Angles of attack significantly differ between the lower rotor and upper rotor for 0.1R and 0.2R configuration. The reason behind this phenomenon is the wake of the upper rotor. The wake of the upper rotor directly interacts with the region between 0.25R and 0.75R of the lower rotor and decreases its angle of attack. The main part of the thrust is generated by the upper rotor for both 0.1R and 0.2R configuration.

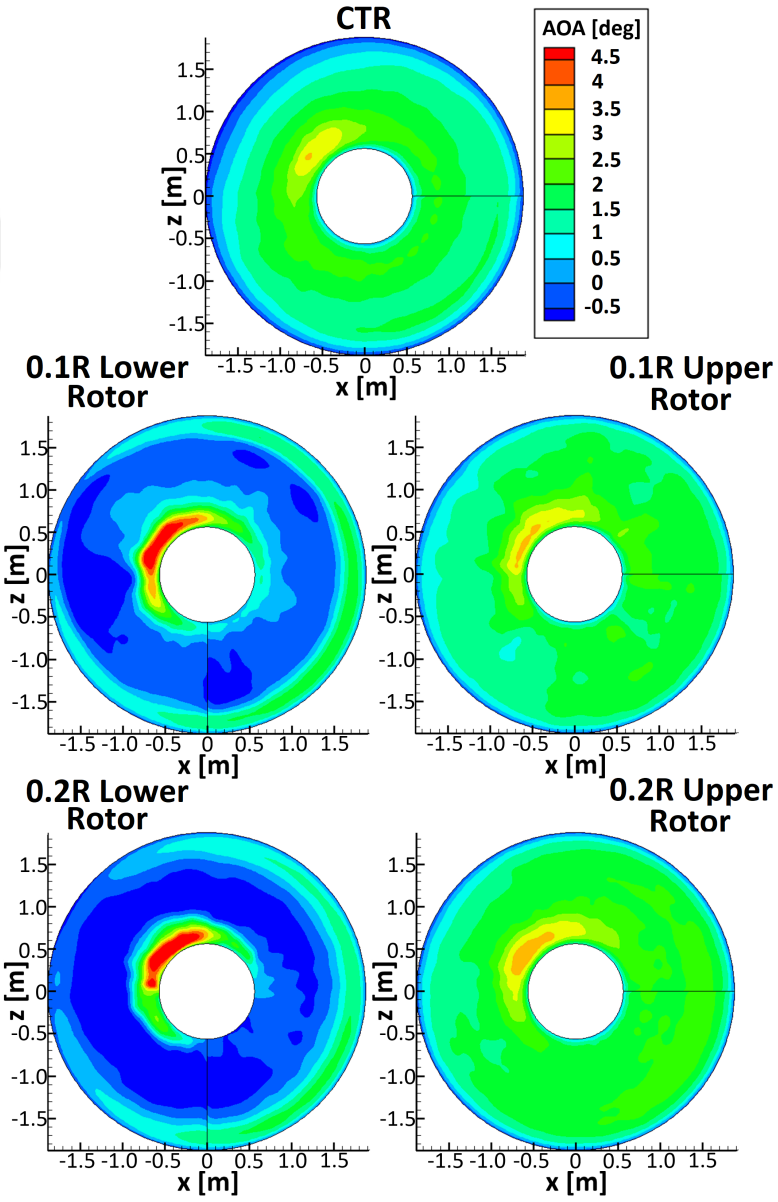

Figure 4.24: Angle of attack contour on disc for various vertical distance at hover condition

The angle of attack variations are shown in Figure 4.25 at quartering flight condition. No correlation is observed with the change in vertical distance.

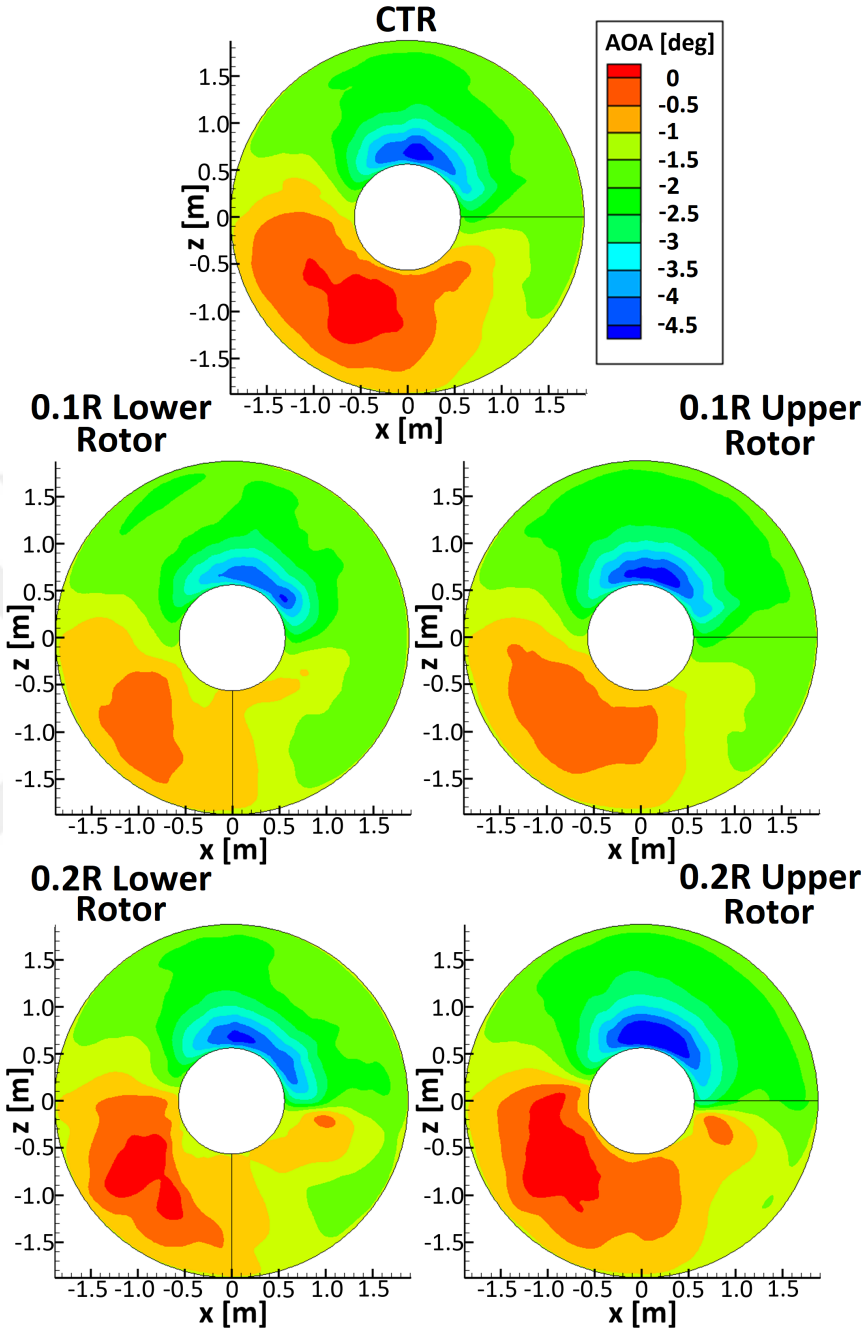

Figure 4.25: Angle of attack contour on disc for various vertical distance at quartering flight condition

BVI based loading impulses are well seen in the non-dimensional normal force illustrated in Figure 4.26 at forward flight condition. Increasing vertical distance vanishes the BVI locations.

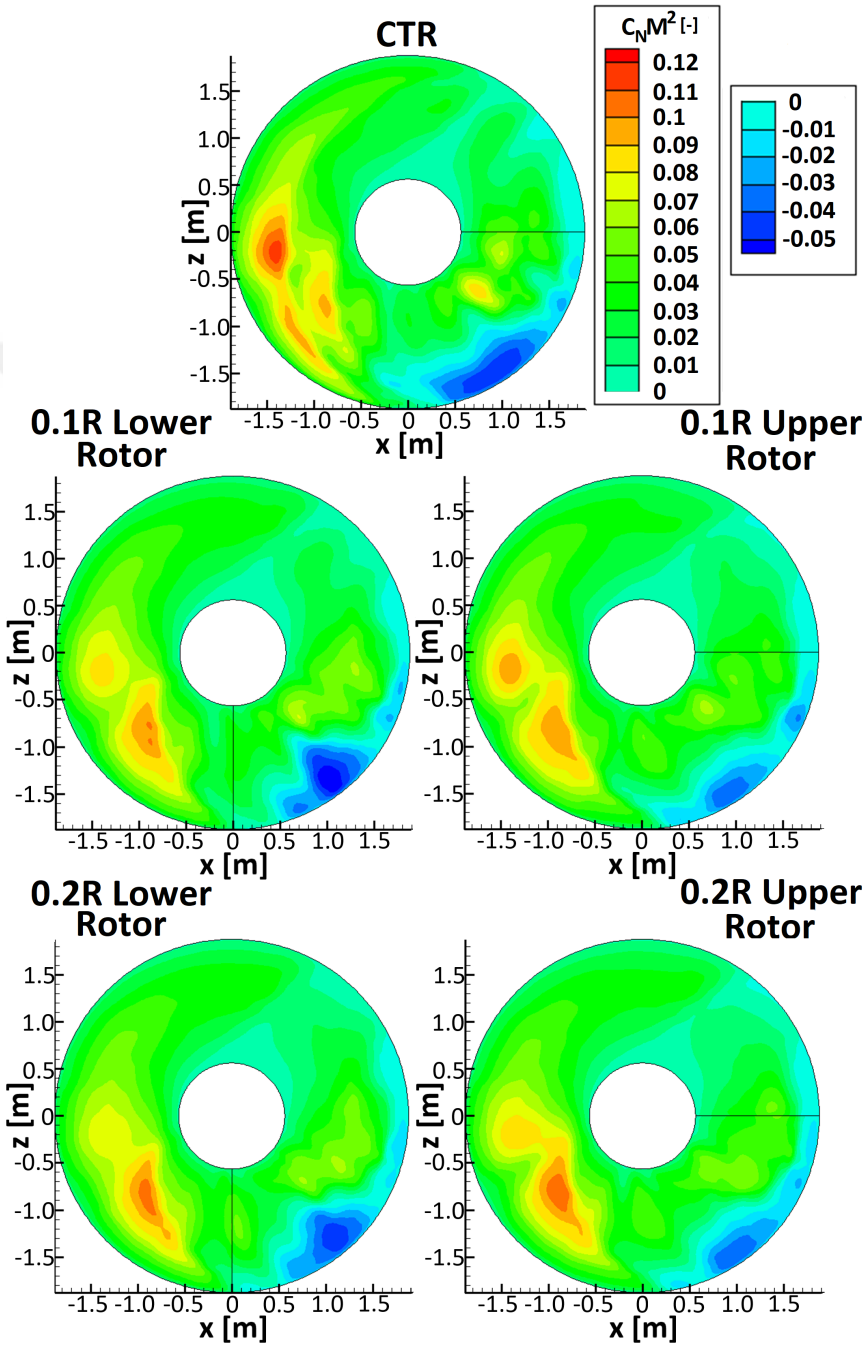

Figure 4.26: Non-dimensional normal force contour on disc for various vertical distance at forward flight condition

Non-dimensional normal force contours are depicted in Figure 4.27. The upper rotor generates the main contribution to the overall thrust of the tail rotor. The region between 0.25R and 0.75R at the lower rotor generates almost no thrust. However, there are no significant oscillations observed generated by the main rotor wake.

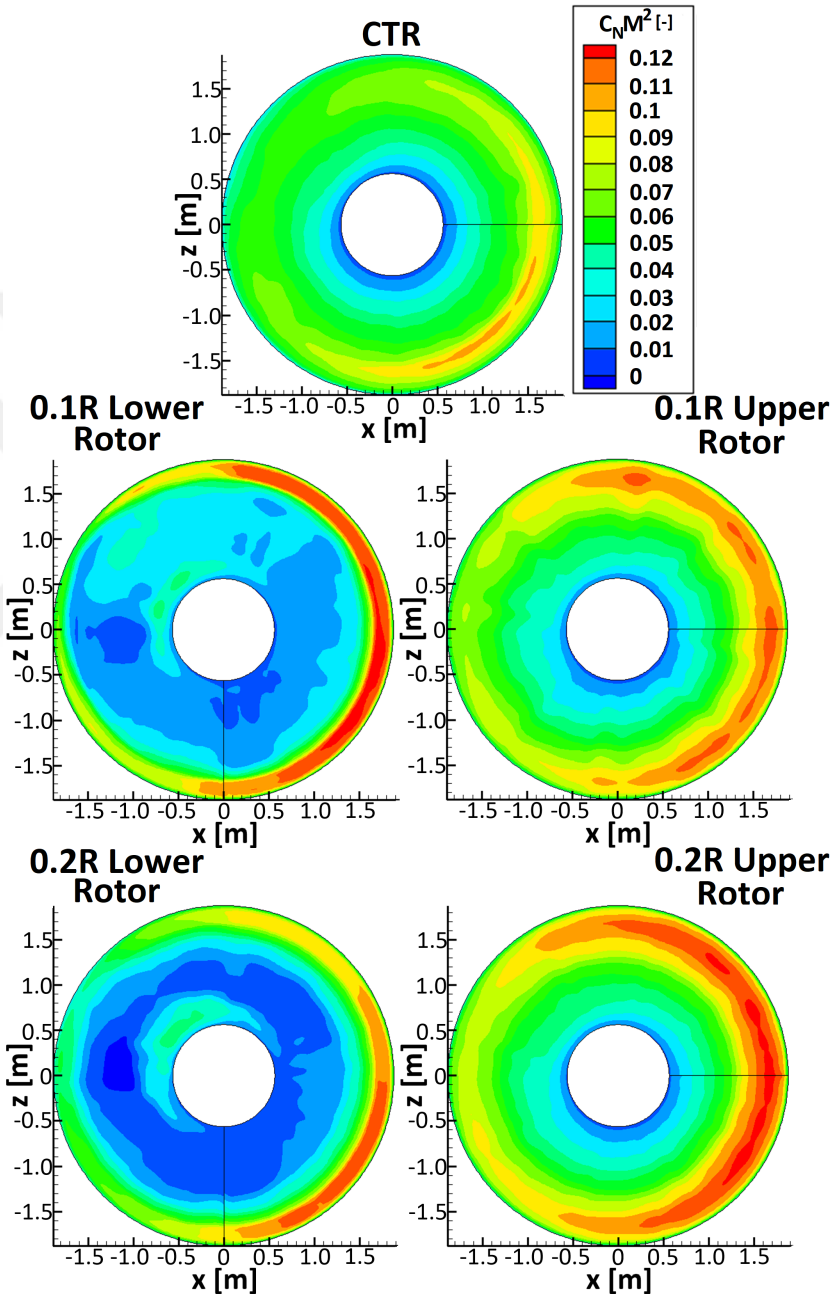

Figure 4.27: Non-dimensional normal force contour on disc for various vertical distance at hover condition

Quartering flight condition has increasing oscillations over non-dimensional normal force contour with the increasing vertical distance, illustrated in Figure 4.28.

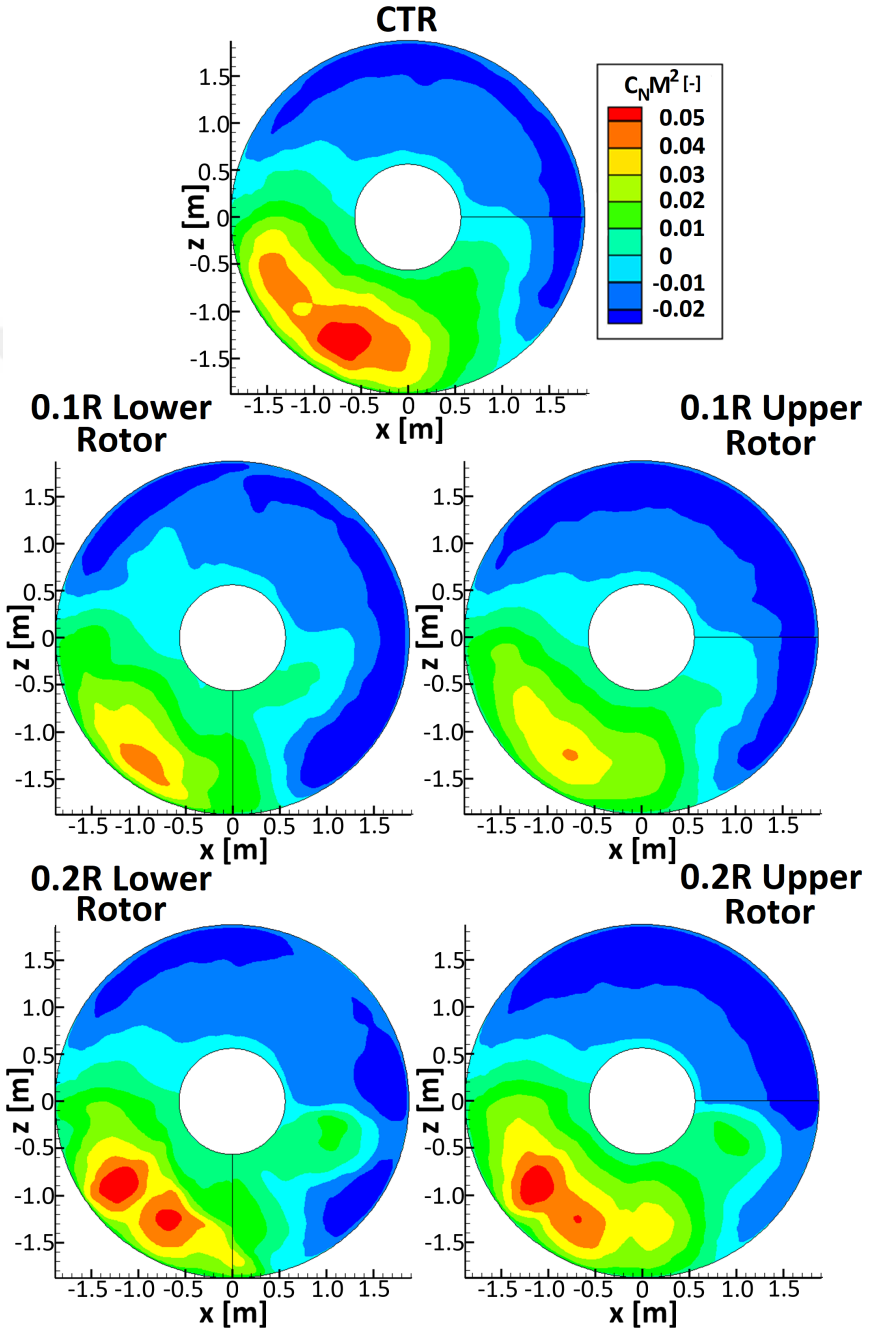

Figure 4.28: Non-dimensional normal force contour on disc for various vertical distance at quartering flight condition

Peak-to-peak thrust evaluation at each flight condition is given in Figure 4.29. These peak-to-peak thrusts are non-dimensionalized by the CTR peak-to-peak value. Findings point that increasing the vertical distance increases the peak-to-peak oscillation up to %81 at quartering flight. On the other hand, increasing vertical distance causes less peak-to-peak oscillation at forward flight and hover conditions. Oscillations are decreased %20 at most for hover condition and %8 for forward flight condition.

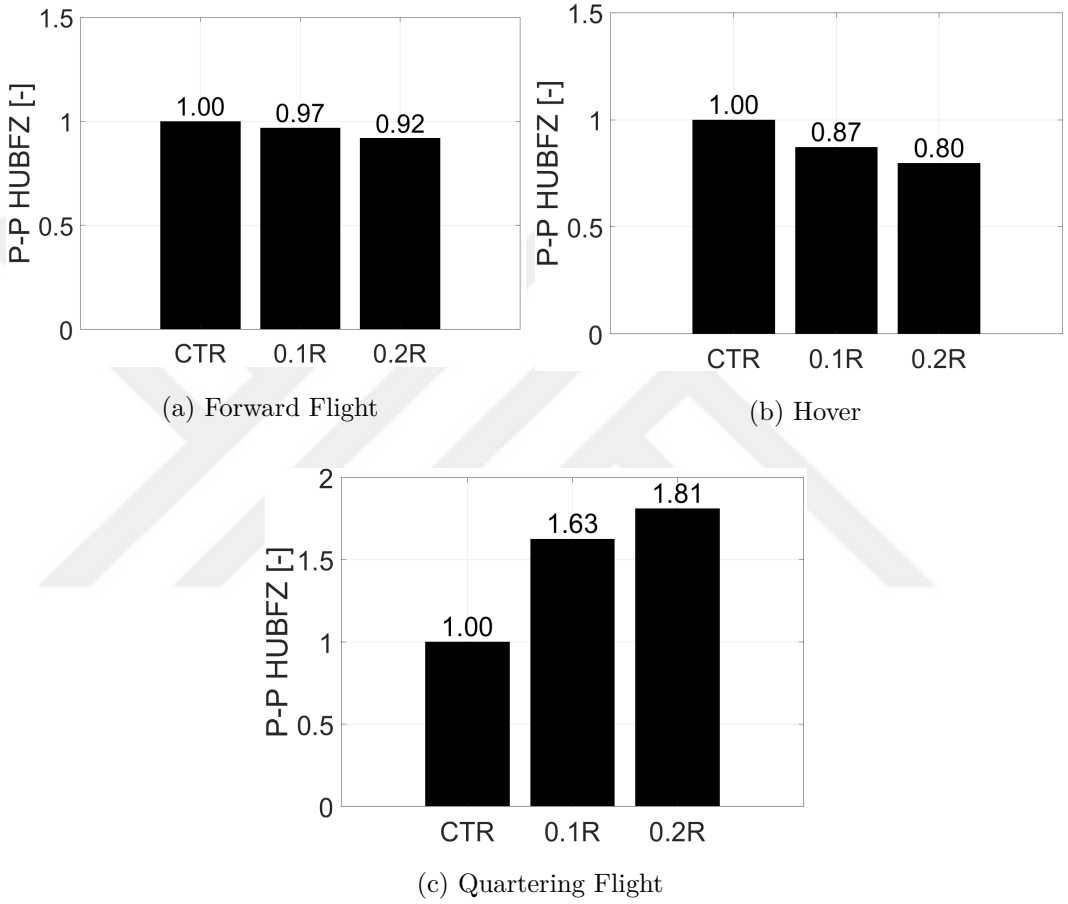

(a) Forward Flight

(b) Hover

(c) Quartering Flight

Figure 4.29: Peak to peak non-dimensional thrust for various vertical distance at different flight conditions

4.3.1.2 Aeroacoustics

The investigation of aeroacoustics is performed on the aforementioned mentioned horizontal and vertical plane microphone grids. Change on acoustic pressure is

represented in Figure 4.30.

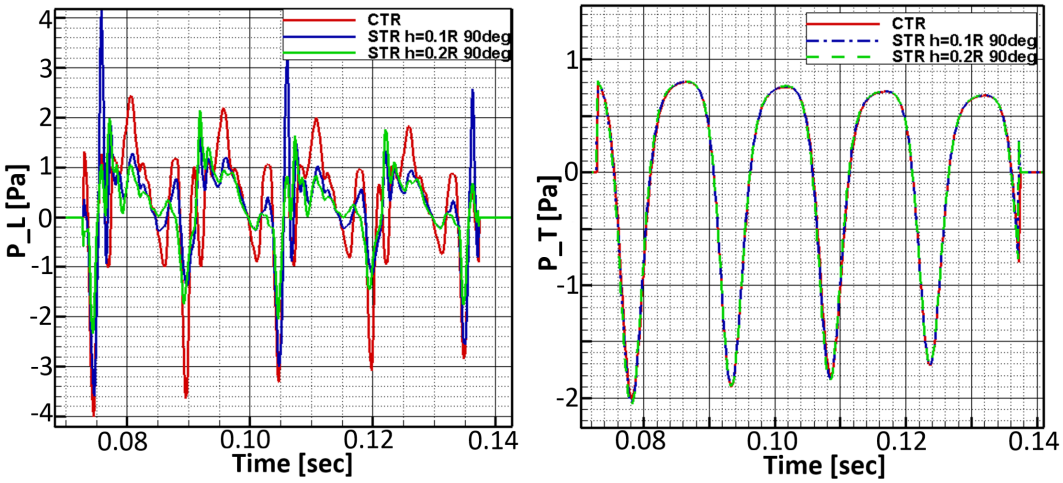

(a) Loading noise

(b) Thickness noise

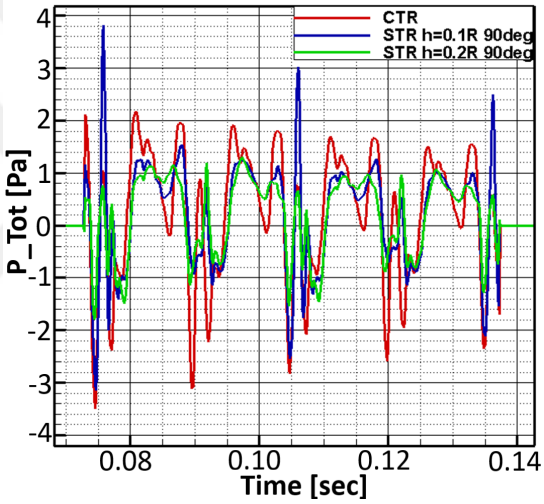

(c) Total noise

Figure 4.30: Acoustic pressure comparison of vertical distance

Loading acoustic pressure is affected by the orientation change. Because orientation alters the aerodynamic behavior of air around the rotors, and it affects the loading noise. It is observed that increasing vertical distance affects the frequency of the loading based acoustic pressures. On the other hand, thickness acoustic pressure is affected insignificantly. The reason for this insignificant change is the distance between rotors. Therefore, small changes are observed in thickness acoustic pressure signals. Overall, total acoustic pressure is the sum-

mation of loading and thickness acoustic pressure, and it is also affected by the orientation change.

More intensive studies are performed on SPL contour planes on different flight conditions.

SPL contours are illustrated on vertical and horizontal plane microphone grids for loading, thickness, and total noise at forward flight condition in Figure 4.31. Results show that contour area of maximum sound pressure level of loading noise on both grids decreases with increasing the vertical distance. Decreasing loading noise is the result of decreasing BVI based oscillations which are shown in angle of attack contour at forward flight condition. Thickness noise remains similar because no change in blade geometry is introduced. Overall, total noise on both grids diminishes with vertical distance due to change in loading noise.

At hover condition, SPL contours are given in Figure 4.32, and small changes are observed on area of maximum sound pressure level due to decreasing peak-to-peak oscillations mentioned at previous section.

Dramatically increasing on SPL of loading noise is observed at quartering flight condition and depicted in Figure 4.33. With a similar reason as in forward flight and hover conditions, no significant change is observed at thickness noise. However, thickness noise is dominated the total noise on the horizontal plane. Therefore, the acoustic signature remains similar for total noise.

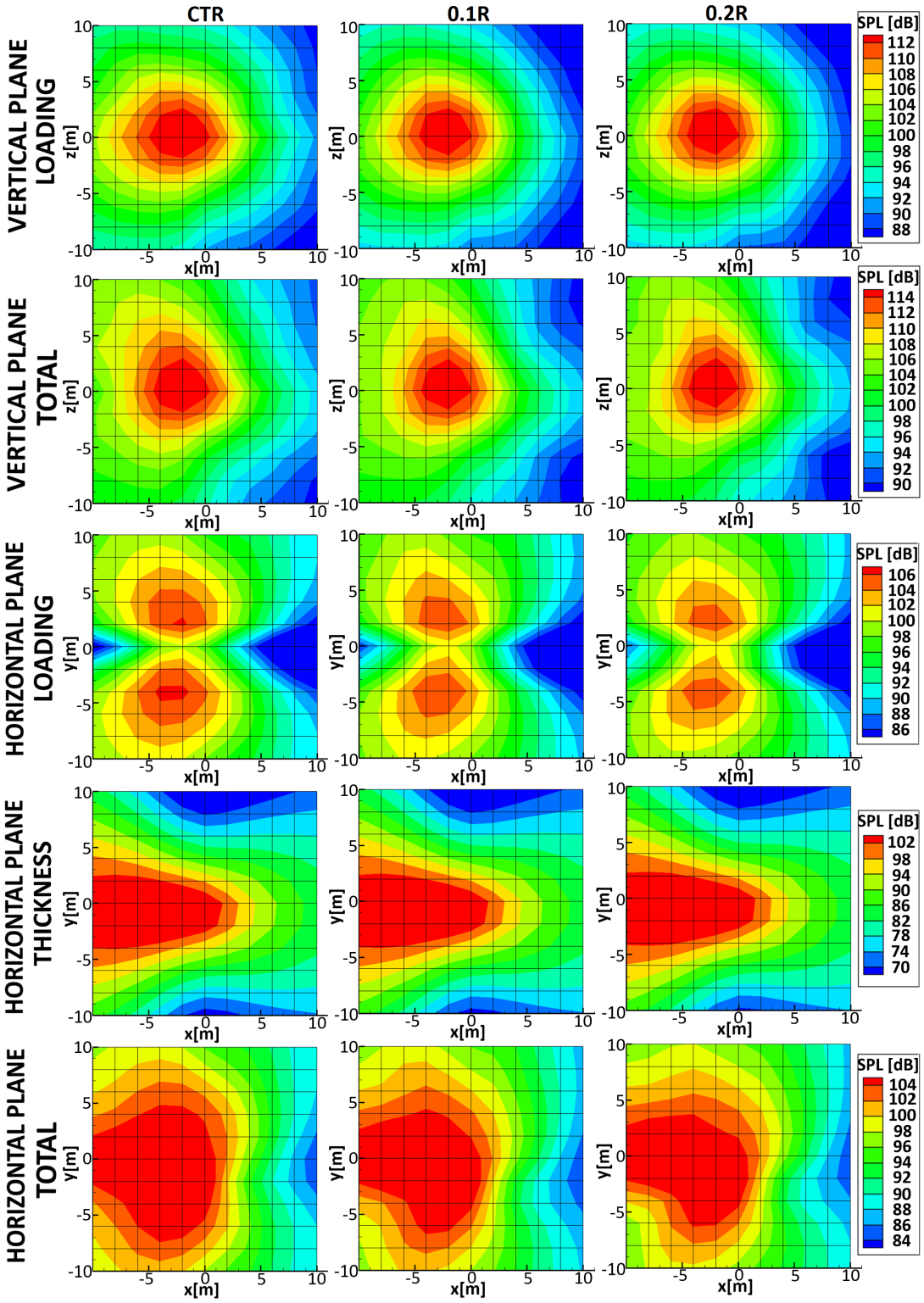

Figure 4.31: Effects of vertical distance for forward flight condition on microphone grids

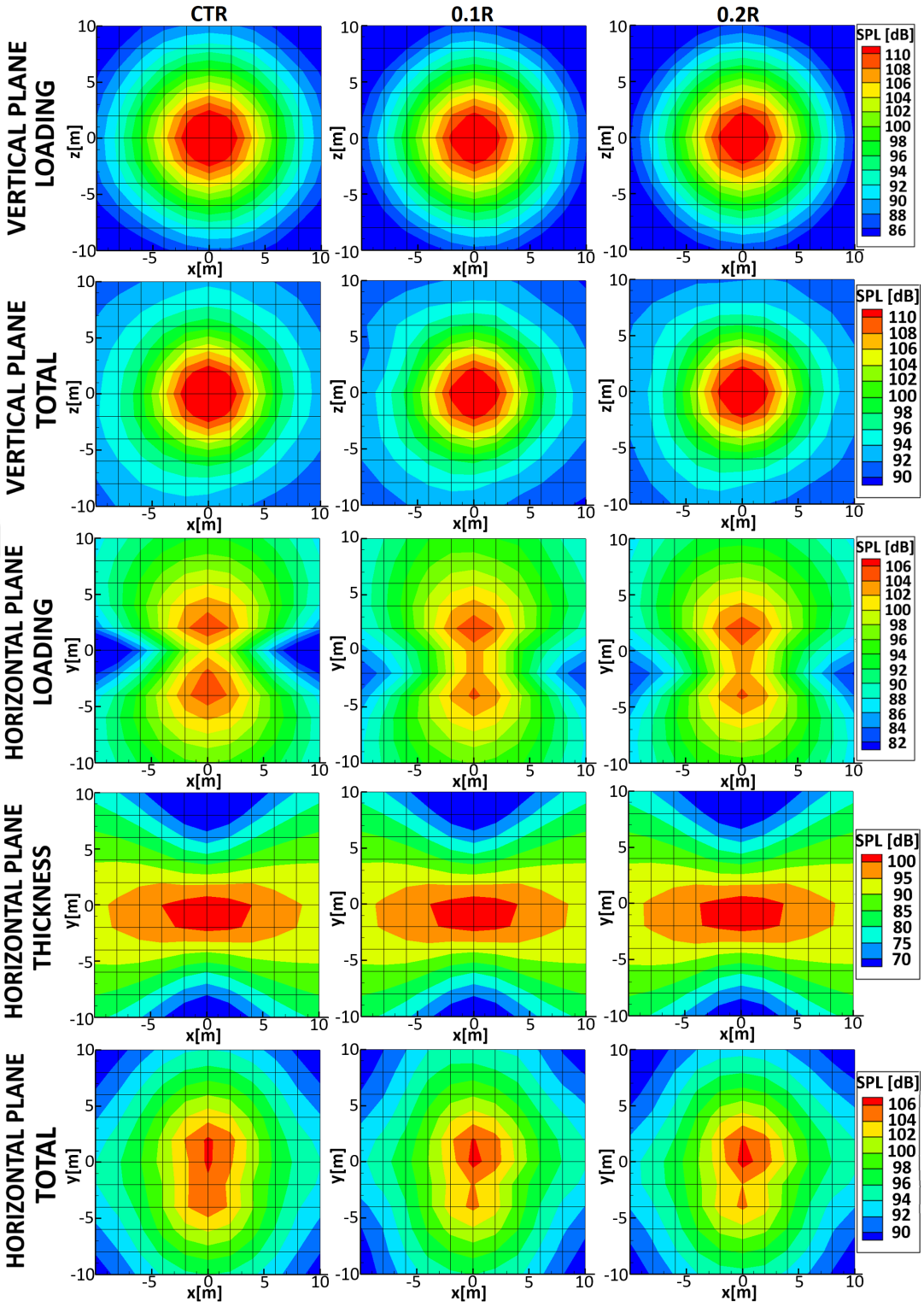

Figure 4.32: Effects of vertical distance for hover condition on microphone grids

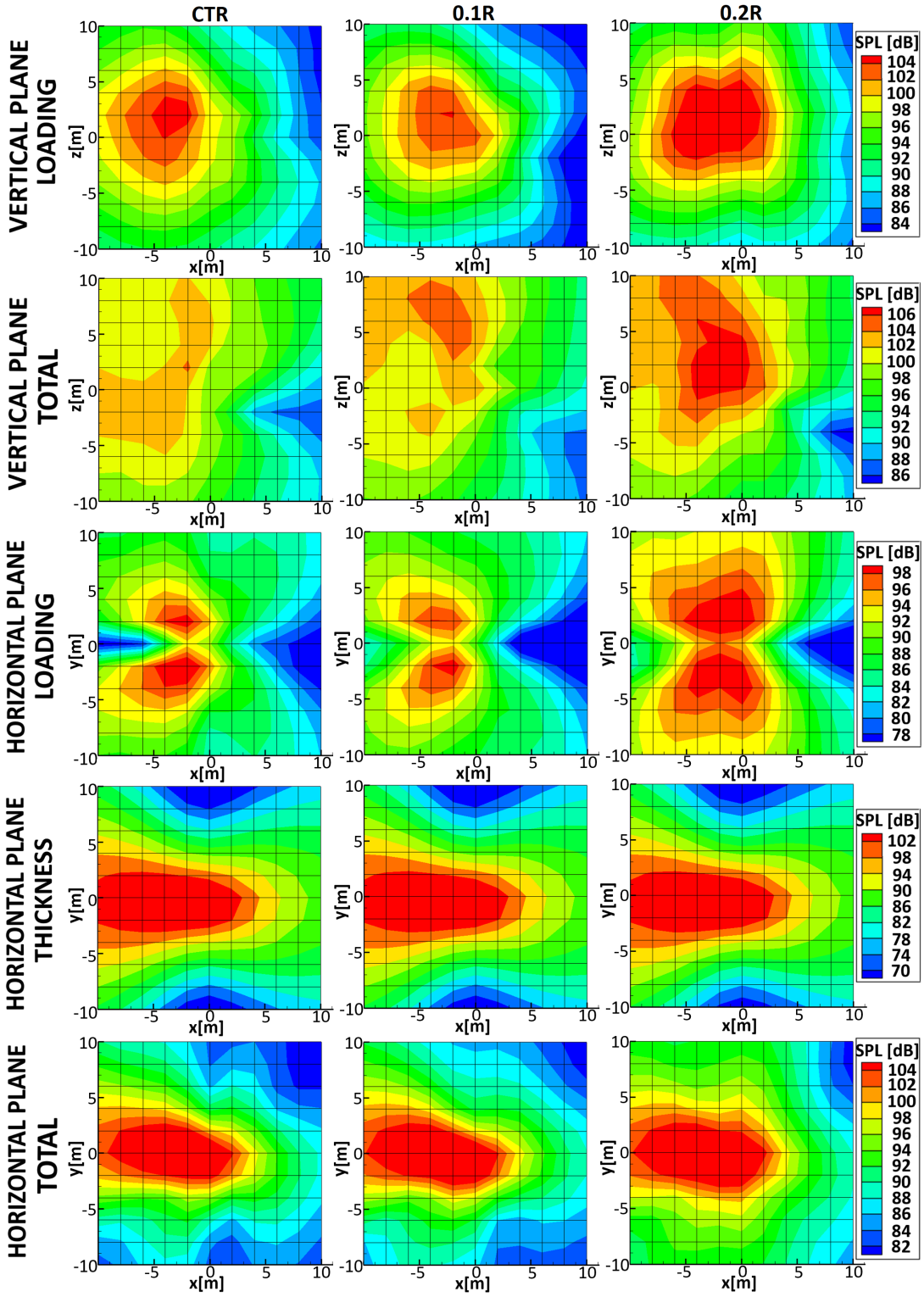

Figure 4.33: Effects of vertical distance for quartering flight condition on microphone grids

4.3.2 Scissors Angle

Another design parameter of scissors tail rotor configuration is called as scissors angle. Scissors angle represents the angular offset of two rotors, illustrated in Figure 4.34. Eleven different scissors angles are investigated in this study, and the angles are tabulated in Table 4.3.

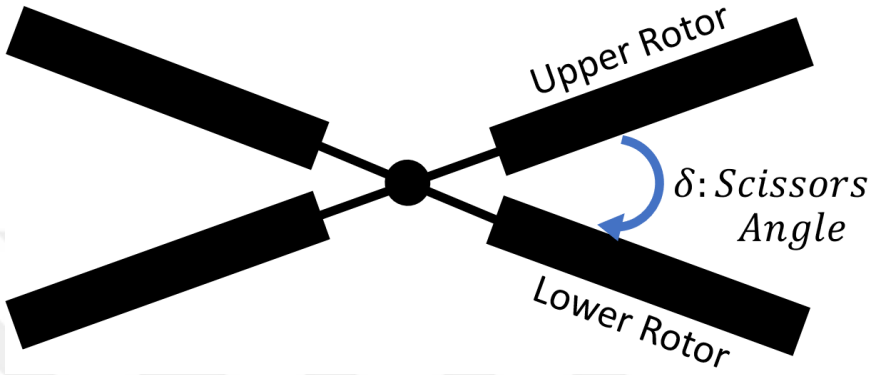

Figure 4.34: Scissors Angle

Table 4.3: Investigated scissors Angle

Scissors Angle	Value	Explanation
15deg	15 [deg]	Lower rotor is leading with 15 degree
30deg	30 [deg]	Lower rotor is leading with 30 degree
45deg	45 [deg]	Lower rotor is leading with 45 degree
60deg	60 [deg]	Lower rotor is leading with 60 degree
75deg	75 [deg]	Lower rotor is leading with 75 degree
90deg	90 [deg]	No leading rotor
105deg	105 [deg]	Upper rotor is leading with 75 degree
120deg	120 [deg]	Upper rotor is leading with 60 degree
135deg	135 [deg]	Upper rotor is leading with 45 degree
150deg	150 [deg]	Upper rotor is leading with 30 degree
165deg	165 [deg]	Upper rotor is leading with 15 degree

4.3.2.1 Aerodynamics

In this section, the change of aerodynamic properties with changing scissors angle is investigated. Initially, the required power is evaluated for all scissors angles. After that, angle of attack and non-dimensional normal force contours are given to investigate BVI based oscillations for 30, 60, 90, 120, and 150 degree scissors angles. Finally, peak-to-peak thrust oscillations are investigated, and correlation analysis is performed for all scissors angles.

Firstly, the non-dimensional required power is evaluated for the aerodynamic investigation with changing scissors angle. The evaluation is illustrated as bar charts in Figure 4.35 and required power values are non-dimensionalized by the power value of CTR configuration. Results indicate %1 required power decrease is observed scissors angle between 15 and 45 degrees both lower and upper rotor leading configurations. The lower rotor leading configuration is superior to upper rotor leading configuration at hover condition. Lower rotor leading configurations require upto %3 less power at hover condition. No correlation is observed at quartering condition in terms of required power.

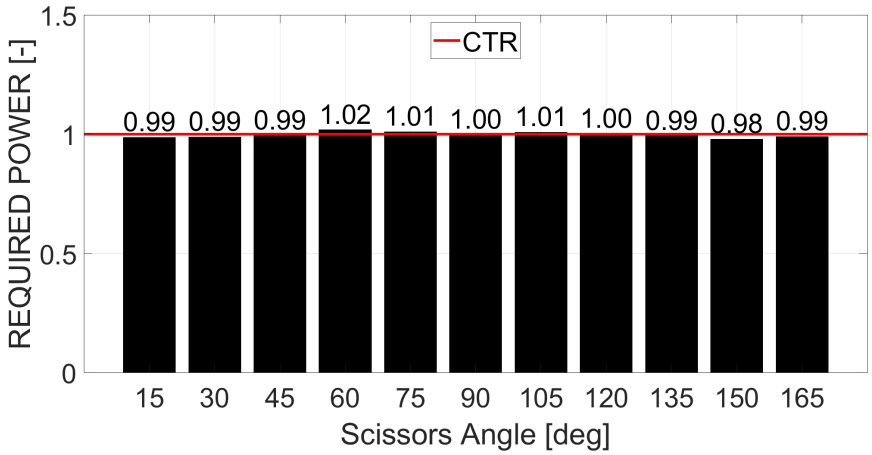

(a) Forward Flight

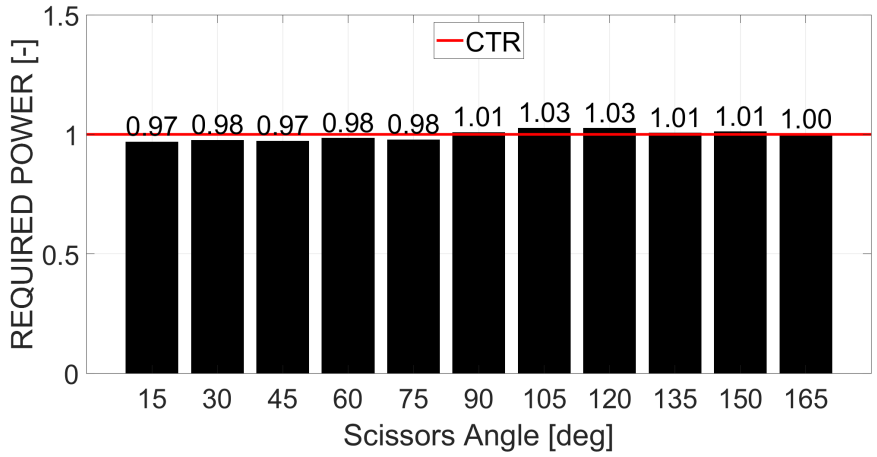

(b) Hover

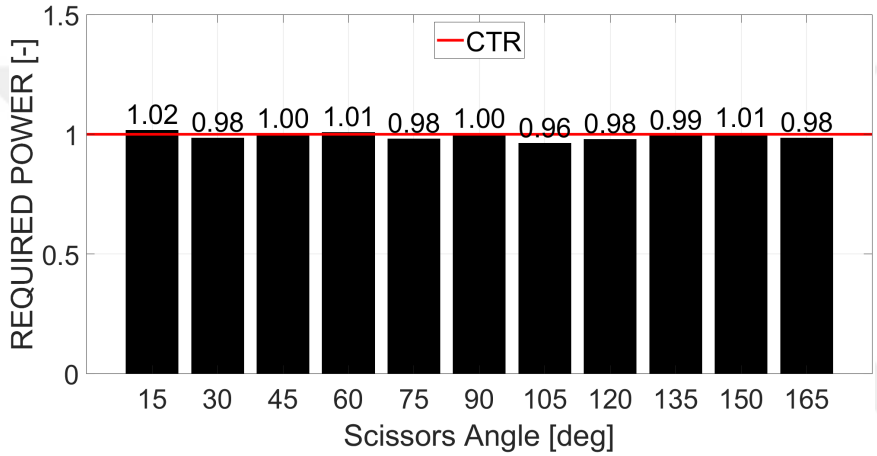

(c) Quartering Flight

Figure 4.35: Non-dimensional required power for various scissors angle at different flight conditions

Angle of attack change is illustrated from Figures 4.36 to 4.38 for forward flight, hover and quartering flight conditions, respectively. Increasing the scissors angle directly affects the airflow over lower and upper rotors at forward flight, hover, and quartering flight conditions. The lower rotor suffers more powerful BVIs at the lower scissors angle, and the upper rotor suffers similarly at larger scissors angle for forward and quartering flight conditions. For hover condition, the interaction of upper rotor wake on lower rotor increases with the increasing scissors angle.

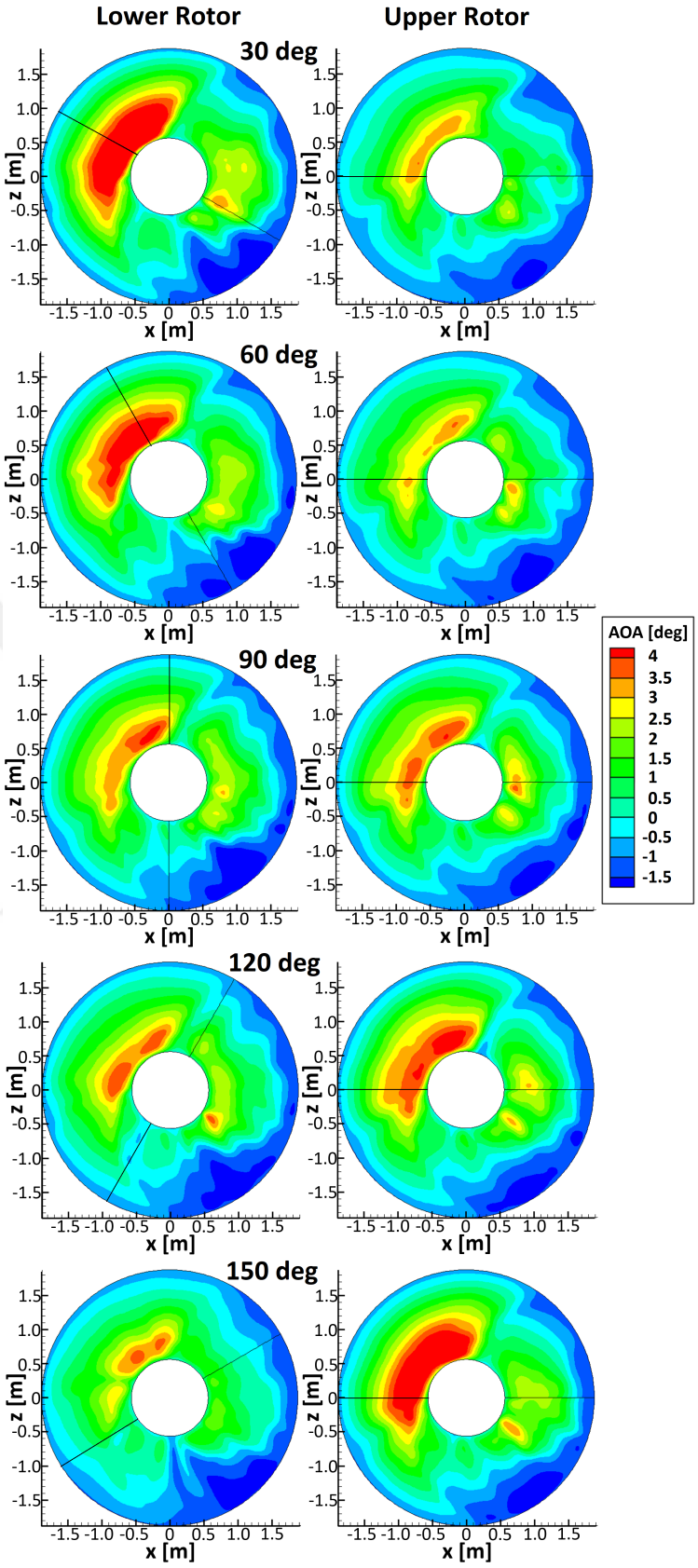

Figure 4.36: Angle of attack contour on disc for various scissors angle at forward flight condition

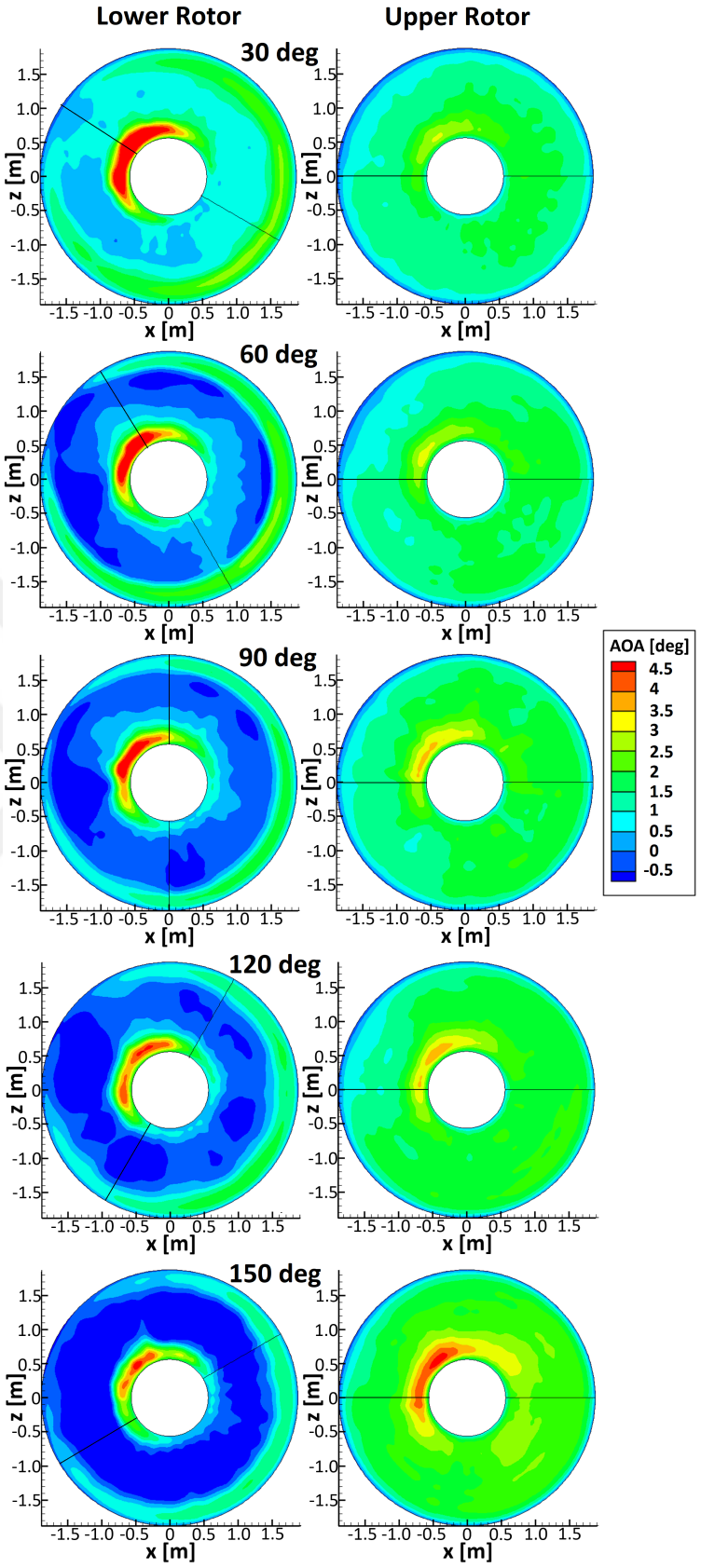

Figure 4.37: Angle of attack contour on disc for various scissors angle at hover condition

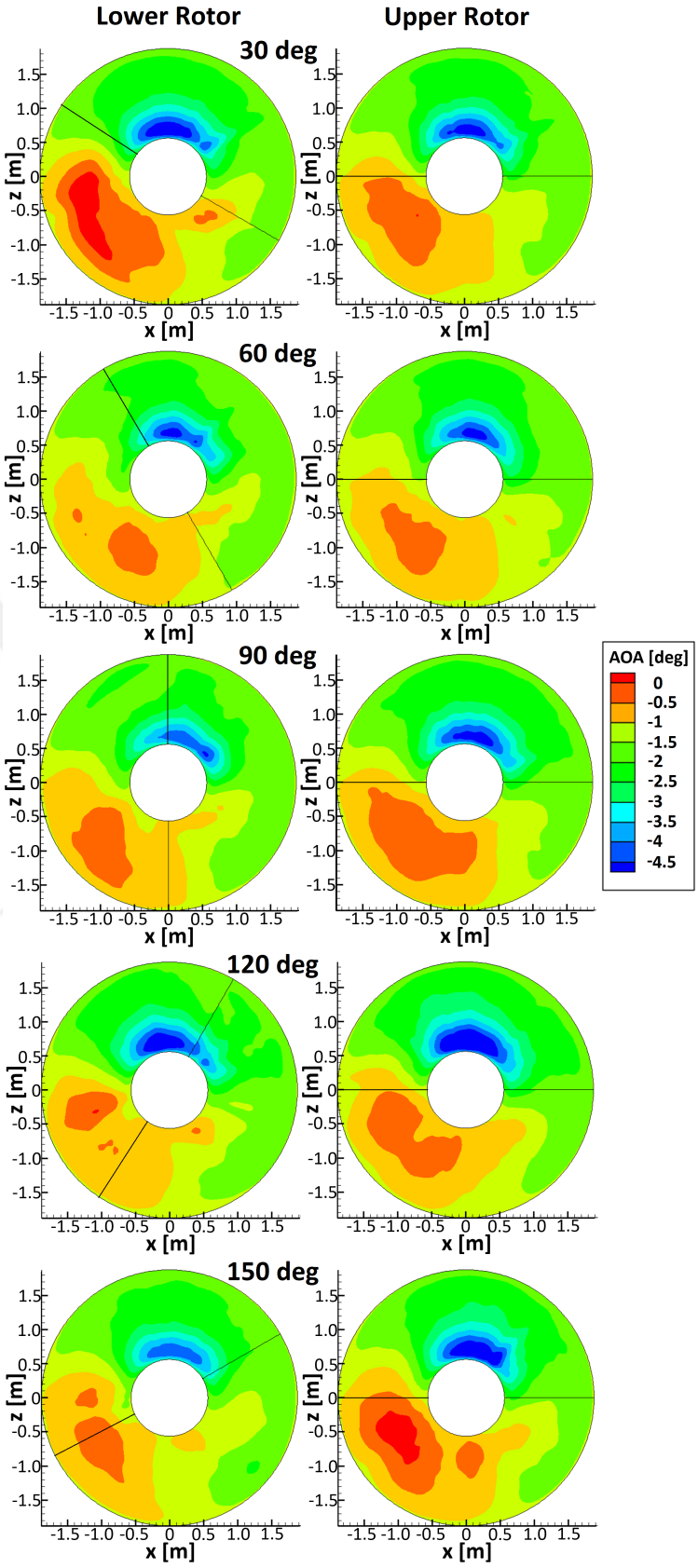

Figure 4.38: Angle of attack contour on disc for various scissors angle at quartering flight condition

Non-dimensional normal force change is illustrated from Figures 4.39 to 4.41 for forward flight, hover and quartering flight conditions, respectively. Similar to the angle of attack investigation, increasing the scissors angle directly affects the thrust generated by lower and upper rotors at forward flight, hover, and quartering flight condition. Especially for hover condition, increasing scissors angle dramatically decreases thrust generated by the lower rotor. The lower rotor of 150 degree scissors angle configuration loses a big amount of its thrust capacity.

Peak-to-peak thrust evaluation at each flight condition is given in Figure 4.42. These peak-to-peak thrusts are non-dimensionalized by the CTR peak-to-peak value. Red line in the figures shows the normalized peak-to-peak thrust value of the CTR configuration. Oscillation over tail rotor thrust highly dependent on scissors angle. Generally, increasing the scissor angle towards 90 degree of scissors angle decreases peak-to-peak thrust value and increases after 90 degrees of scissors angle at forward and quartering flight condition where the main rotor interaction is significant. The main reason for the oscillations is BVIs. Scissors angle affects the interaction position of the main rotor based BVIs and self-generated BVIs. However, such a correlation is not observed at the hover condition due to the main rotor interaction being ineffective.

Oscillation is larger than CTR for any scissors angle except 90 degrees at flight conditions except quartering flight. The variation of oscillation is between 0.13 times and 1.14 times extra on CTR configuration for forward flight condition. Similarly, variation is between 0.01 times and 0.65 times extra for hover condition, and 0.63 times and 4.48 times extra at quartering condition. Quartering flight condition, suffers more oscillatory loads due to generation of small thrust. Flight condition with sideslips requires less thrust due to the fuselage lateral aerodynamic database involves. It causes a more sensitive tail rotor to interactions.

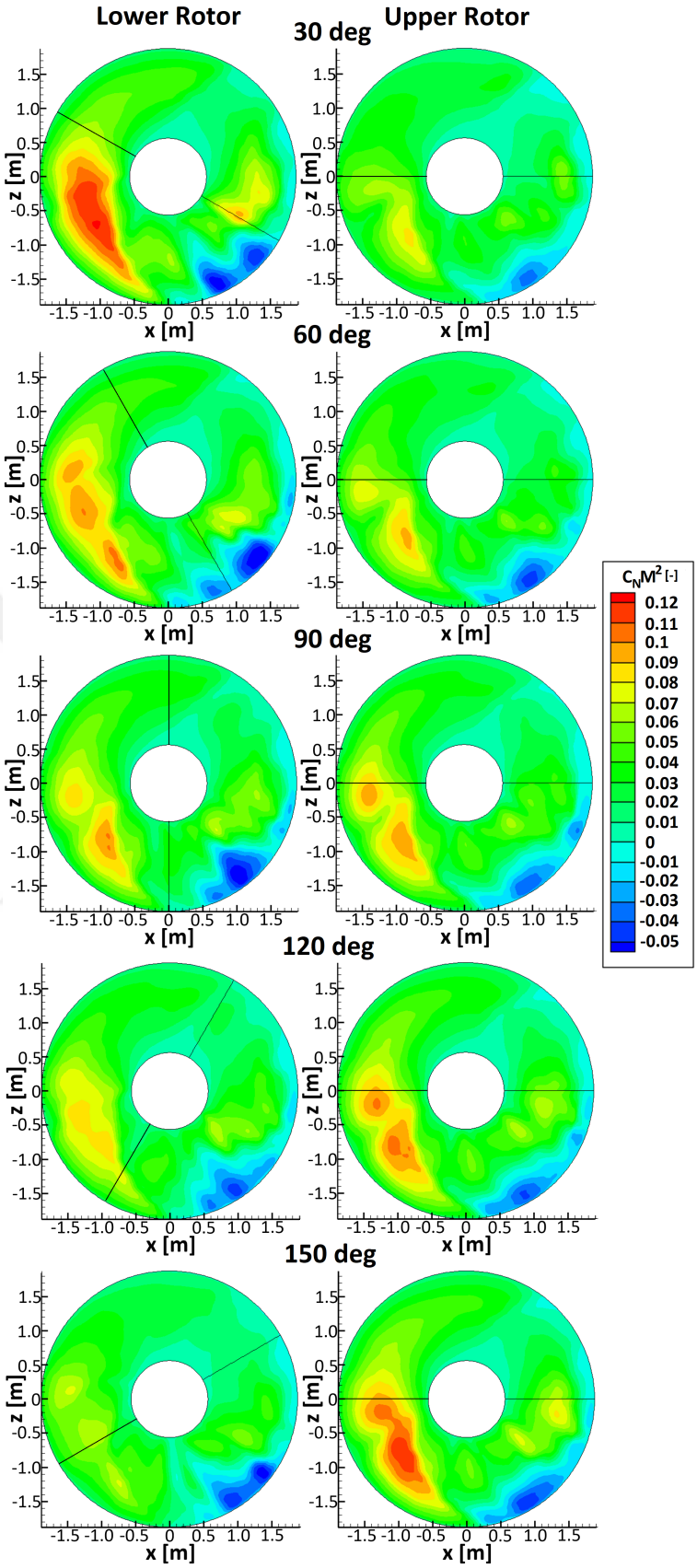

Figure 4.39: Non-dimensional normal force contour on disc for various scissors angle at forward flight condition

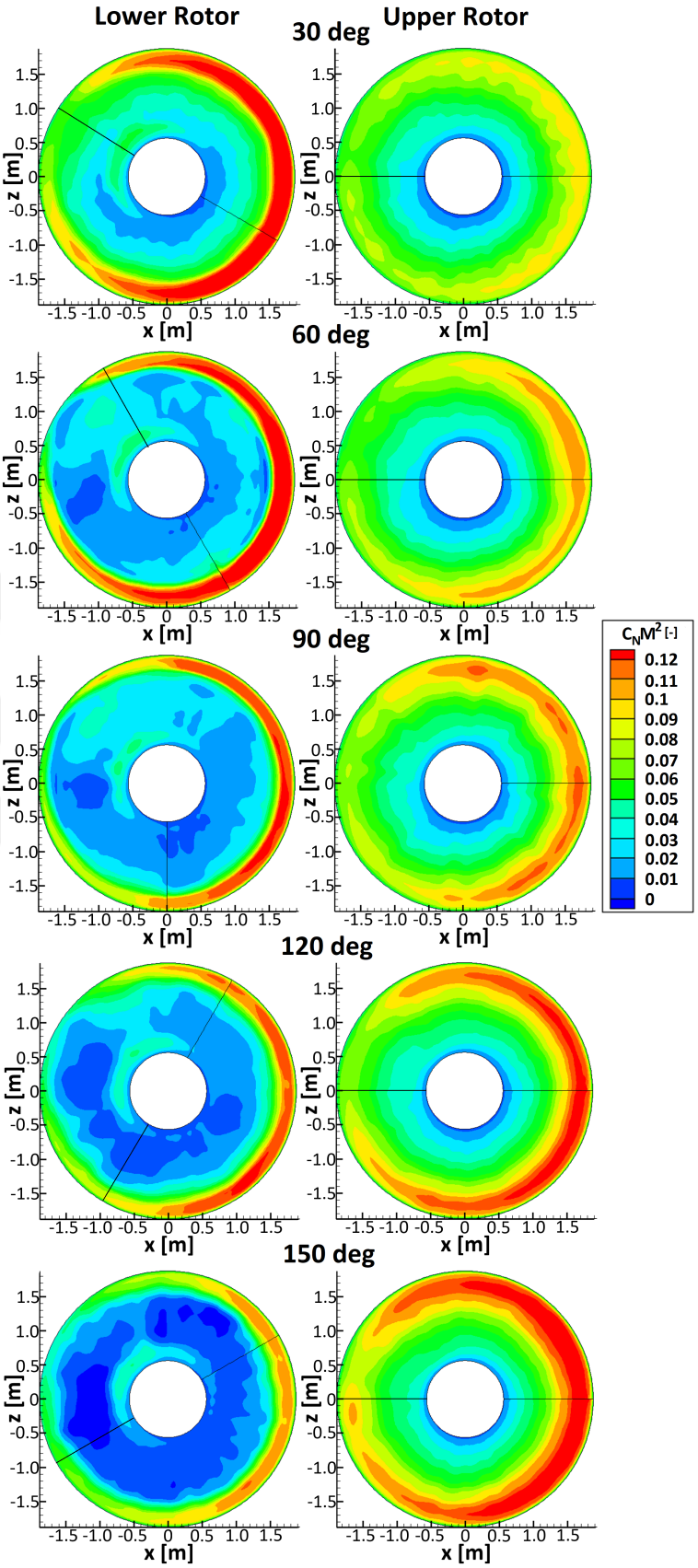

Figure 4.40: Non-dimensional normal force contour on disc for various scissors angle at hover condition

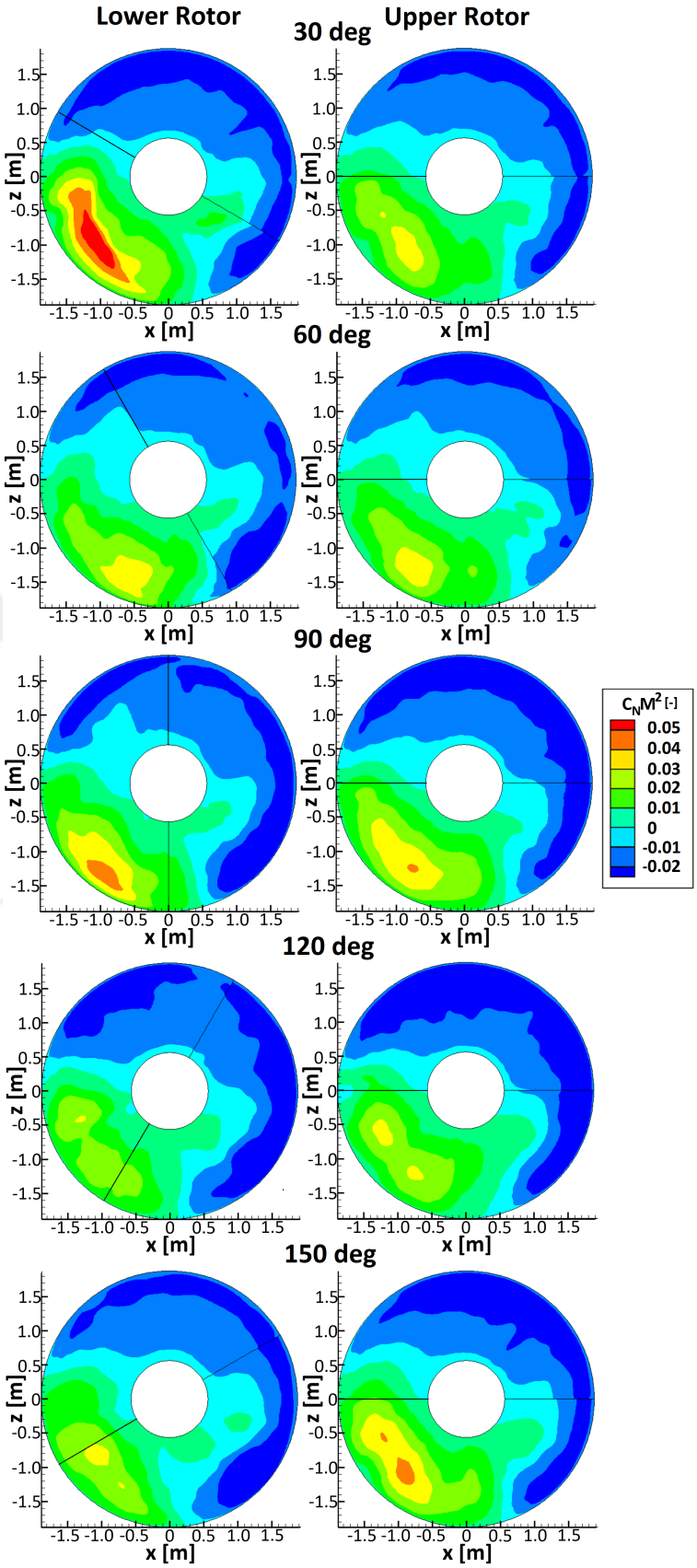

Figure 4.41: Non-dimensional normal force contour on disc for various scissors angle at quartering flight condition

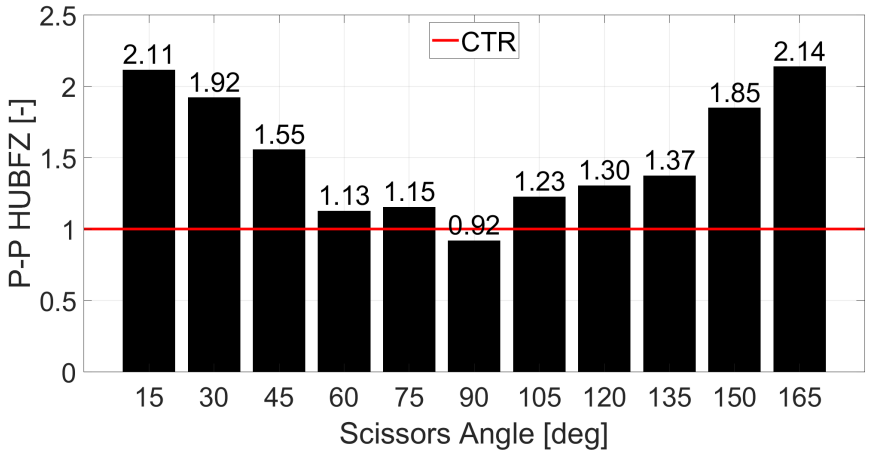

(a) Forward Flight

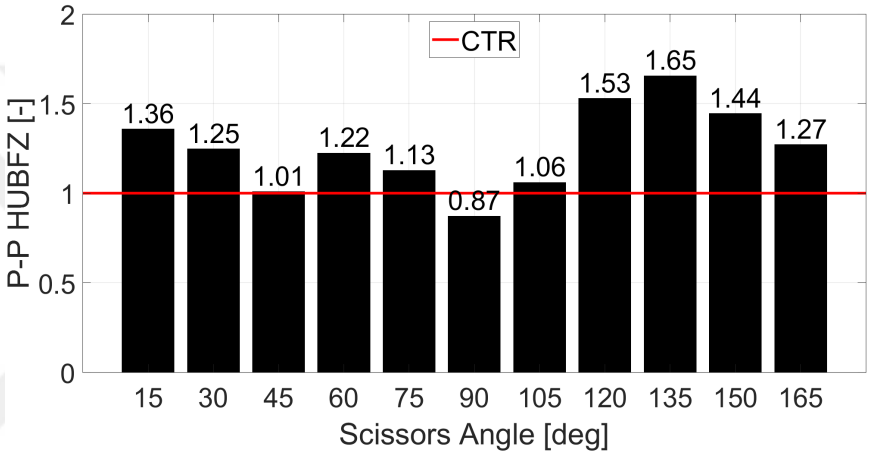

(b) Hover

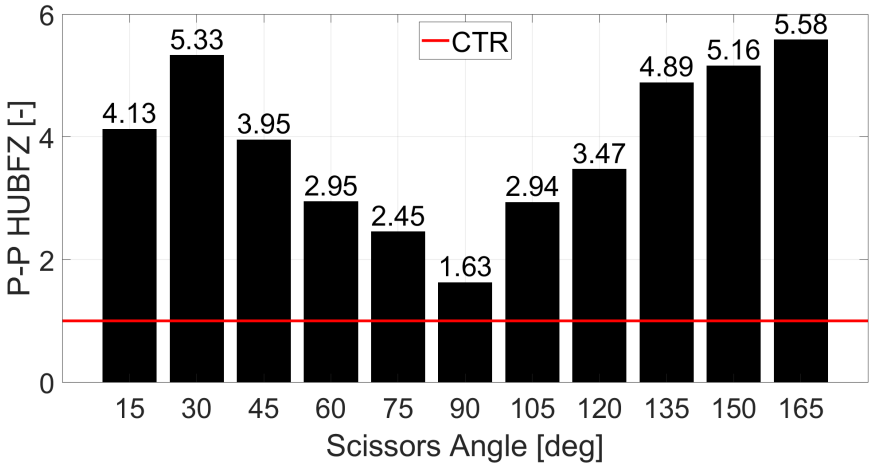

(c) Quartering Flight

Figure 4.42: Peak to peak non-dimensional thrust for various scissors angle at different flight conditions

4.3.2.2 Aeroacoustics

The investigation of aeroacoustics is performed on previously mentioned vertical and horizontal plane microphone grids. Change on acoustic pressure for some of the scissors angle is represented in Figure 4.43.

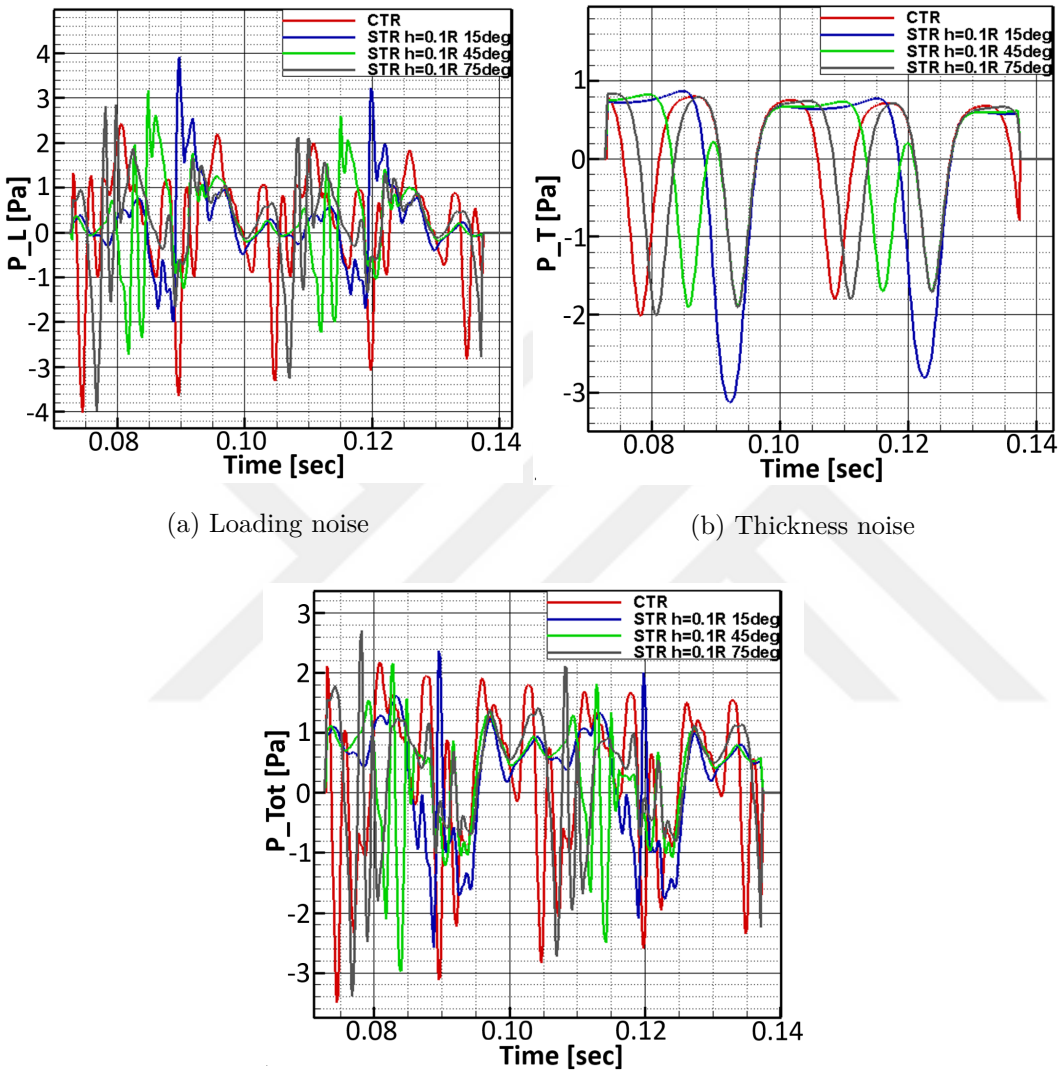

(a) Loading noise

(b) Thickness noise

(c) Total noise

Figure 4.43: Acoustic pressure comparison of scissors angle

Loading acoustic pressure is affected by the orientation change. Because orientation alters the aerodynamic behavior of air around the rotors, and it affects the loading noise. Furthermore, thickness noise is significantly changed. This

effect is called as modulated effect [53]. It is seen four peaks at thickness noise of CTR equally spaced. However, the number of peaks and spacing between peaks are changed at the thickness noise of STR. For example, STR with 15 degree scissors angle has two peaks. Even this configuration has four blades, it is acted as two blades rotor in the perspective of noise signals. The aeroacoustic signals are superposed in this configuration, and they become one huge single peak. On the other hand, STR with 45 degree scissors angle has a magnitude-wise decreased four peaks. It points that thickness noise is significantly affected by the scissors angle. In the end, total acoustic pressure is the superposition of loading and thickness acoustic pressure. Therefore, it is certainly affected by the scissors angle.

More intensive studies are performed on an SPL contour plane on different flight conditions. Loading and thickness noises are investigated at 30, 60, 90, 120, and 150 degree scissors angle, and total noise is investigated entire scissors angle set.

Firstly, forward flight condition is investigated and illustrated from Figures 4.44 to 4.48. Due to aerodynamic behavior change, loading noise is highly affected, and minimum of 2 dB decrease is seen maximum sound pressure level contour on the horizontal plane. The change of scissors angle directly influences thickness noise. The level of the noise is the same for all configurations, but area of the maximum sound pressure level differs. Minimum of 2 dB noise decreases are observed at 30, 135, and 150 degree scissors angles for total noise on the horizontal plane. Furthermore, areas of the maximum sound pressure level of 135 and 150 degree scissors angle configurations are less than the area of 30 degree scissors angle.

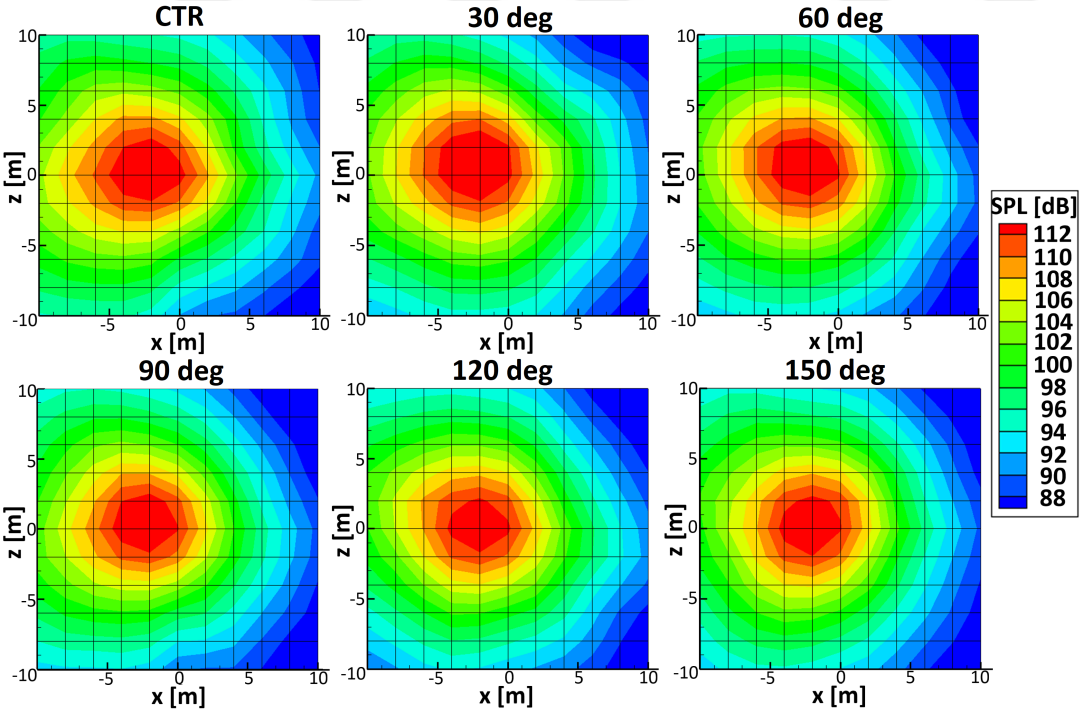

Figure 4.44: Loading noise SPL on vertical plane at forward flight condition

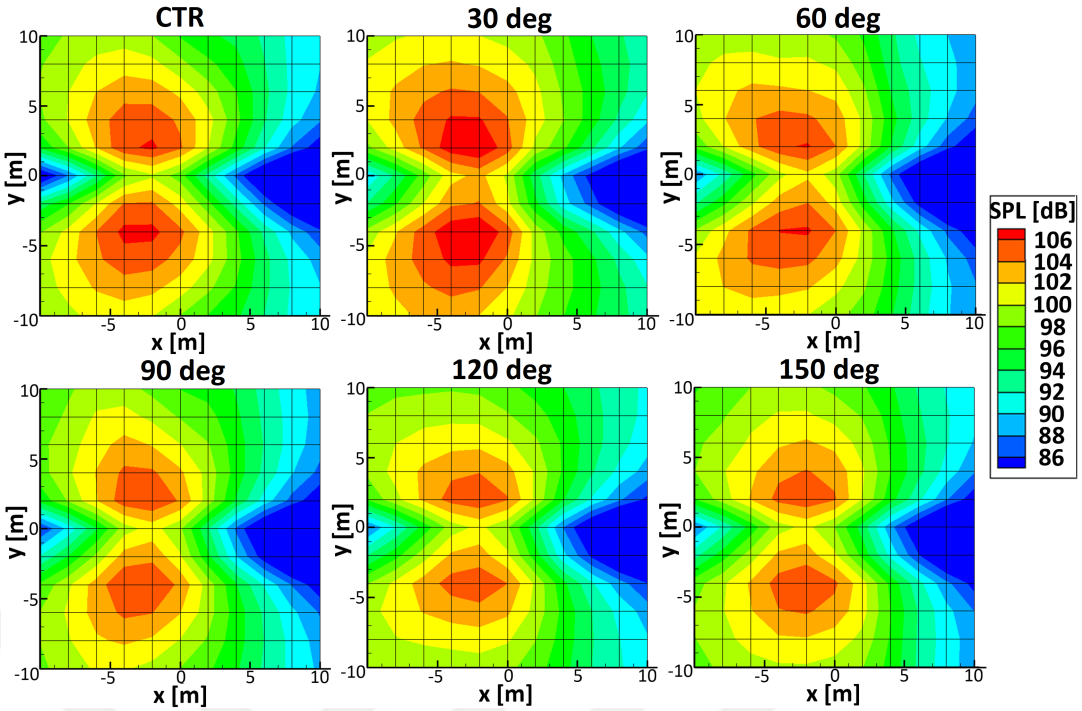

Figure 4.45: Loading noise SPL on horizontal plane at forward flight condition

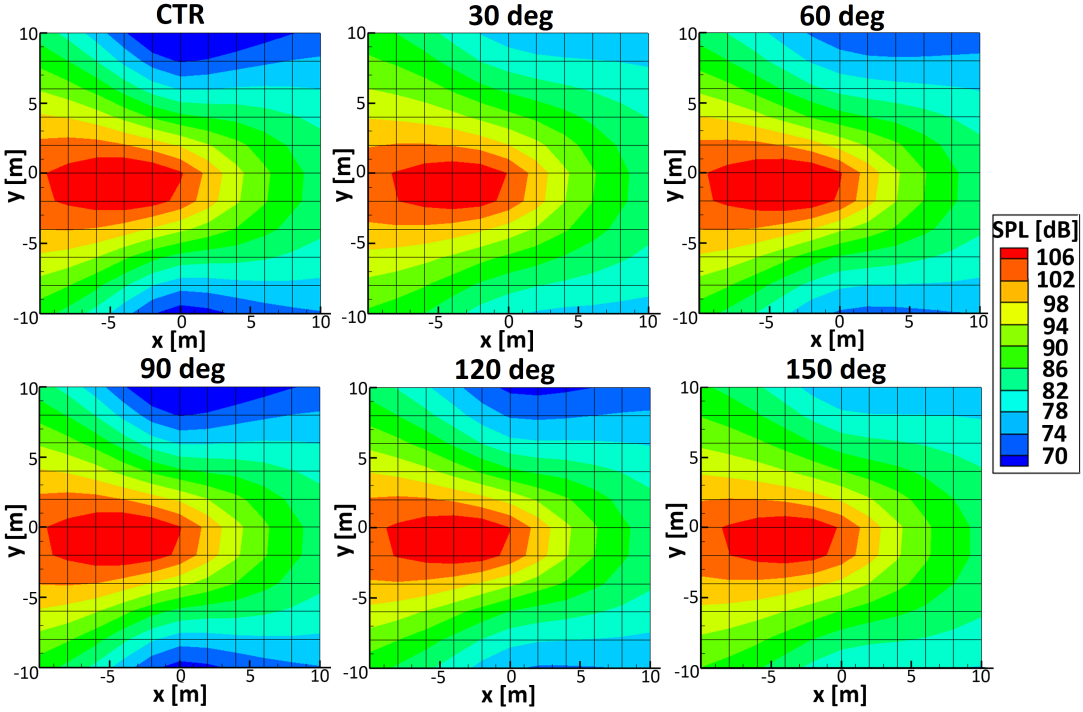

Figure 4.46: Thickness noise SPL on horizontal plane at forward flight condition

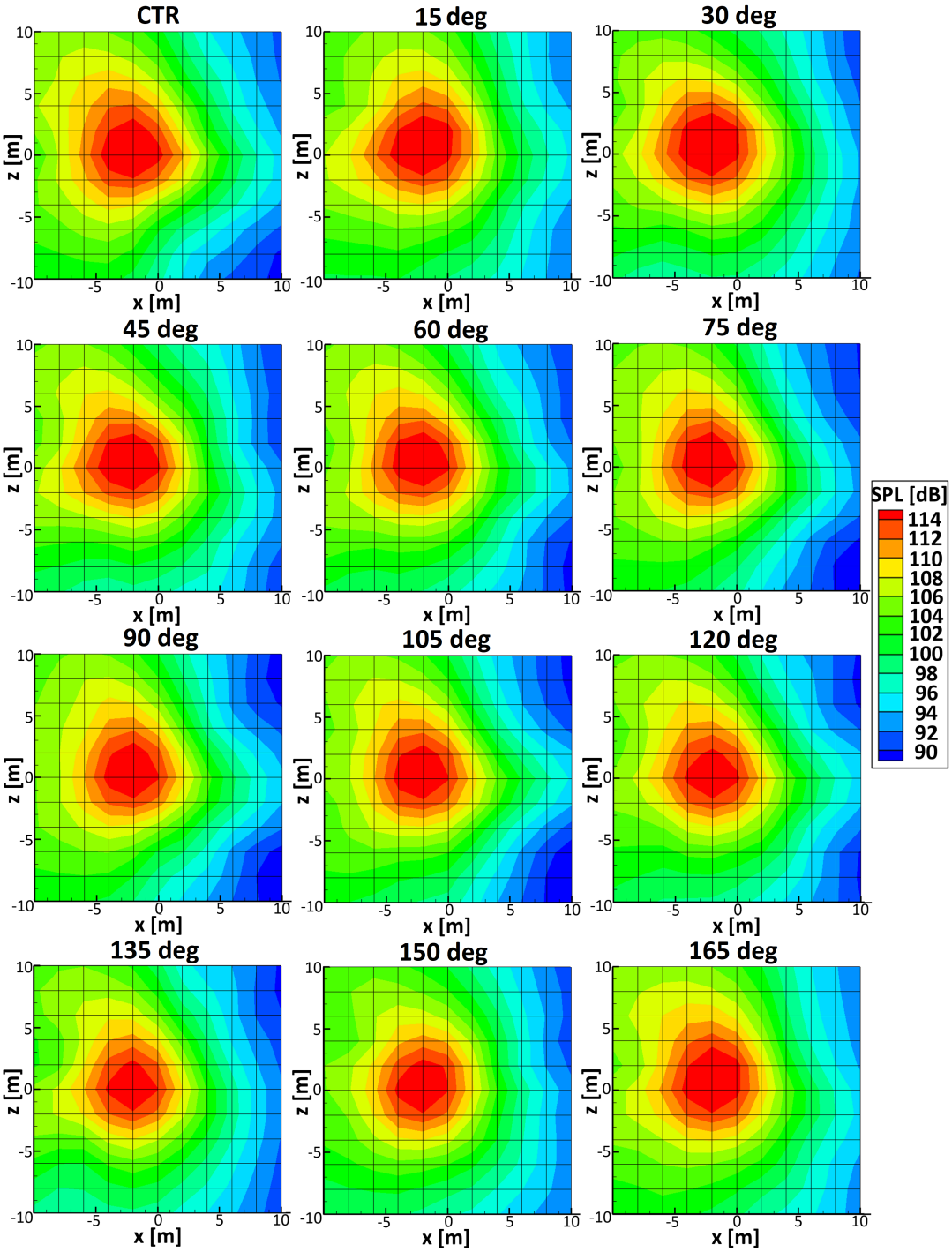

Figure 4.47: Total noise SPL on vertical plane at forward flight condition

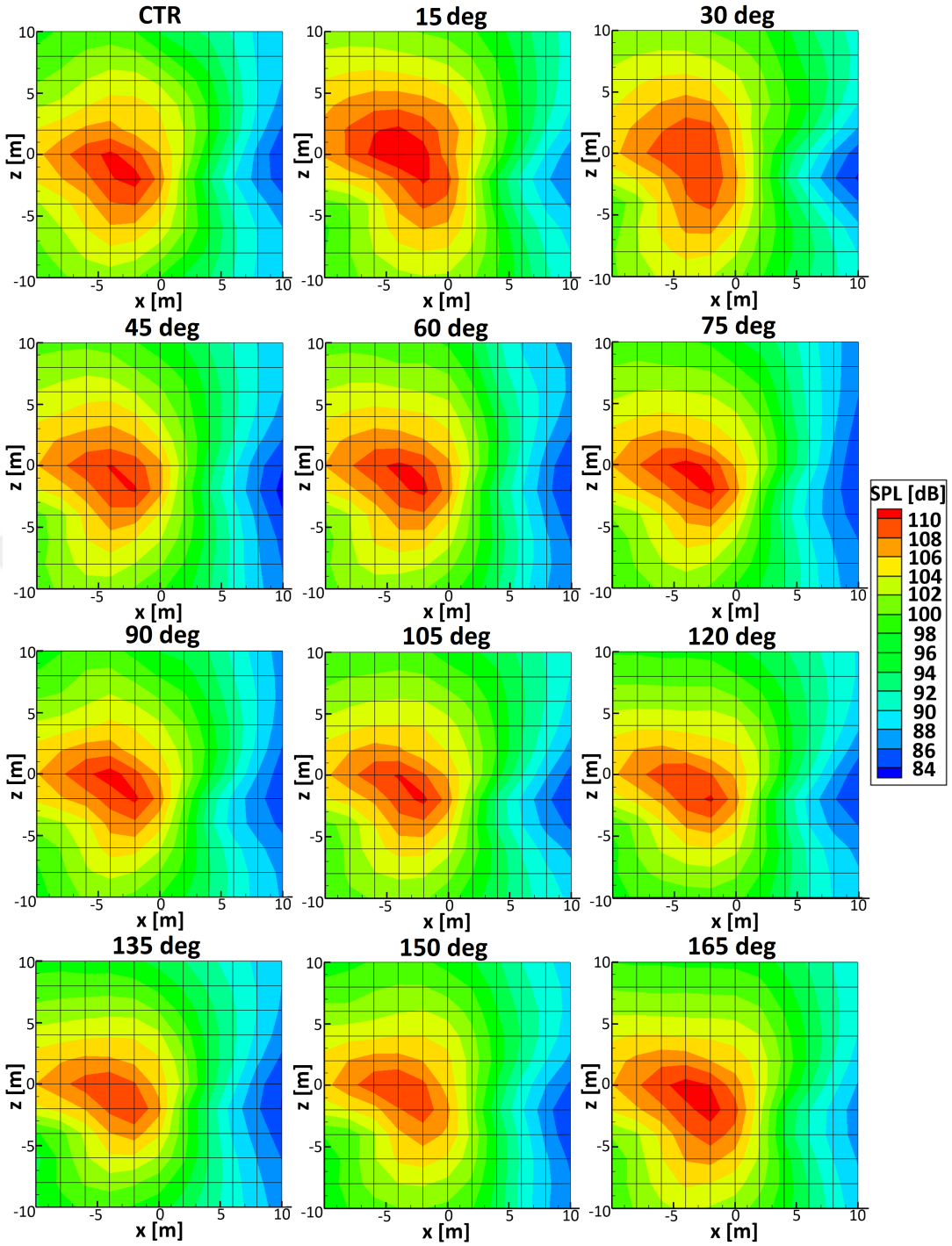

Figure 4.48: Total noise SPL on horizontal plane at forward flight condition

Hover condition is investigated and illustrated from Figures 4.49 to 4.53. As in conventional tail rotor and vertical distance investigations, noise of hover condition is not affected as much as forward and quartering flight conditions with scissors angle. However, 75 degree scissors angle configuration is superior to other configurations for lower area for maximum sound pressure level at total noise on horizontal plane.

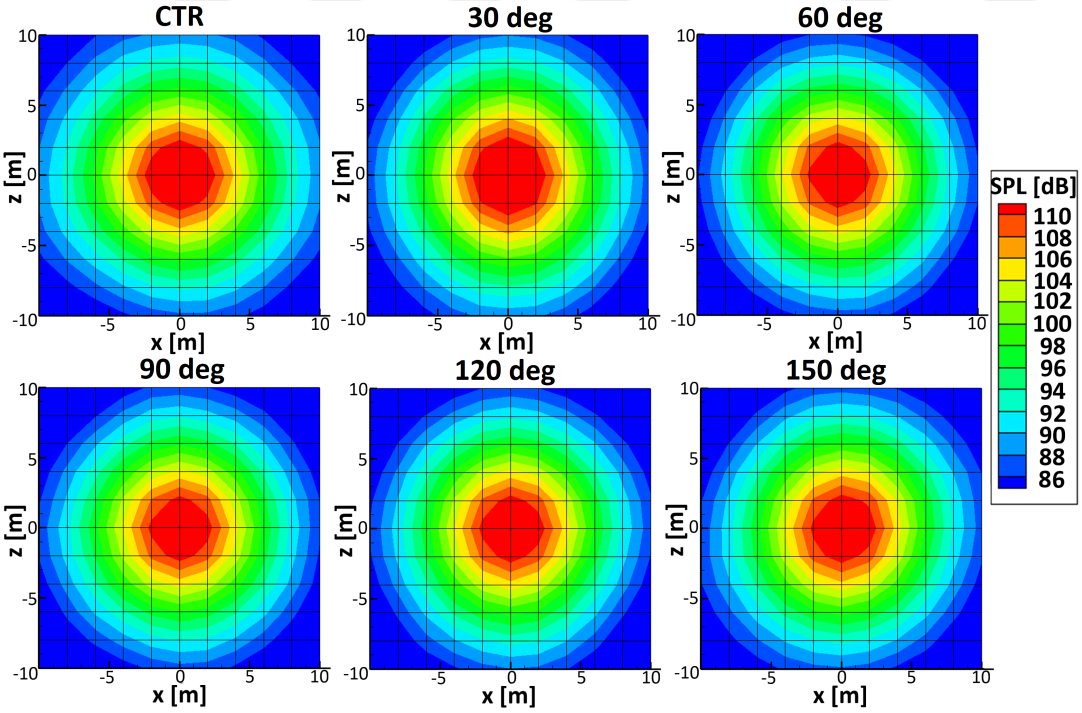

Figure 4.49: Loading noise SPL on vertical plane at hover condition

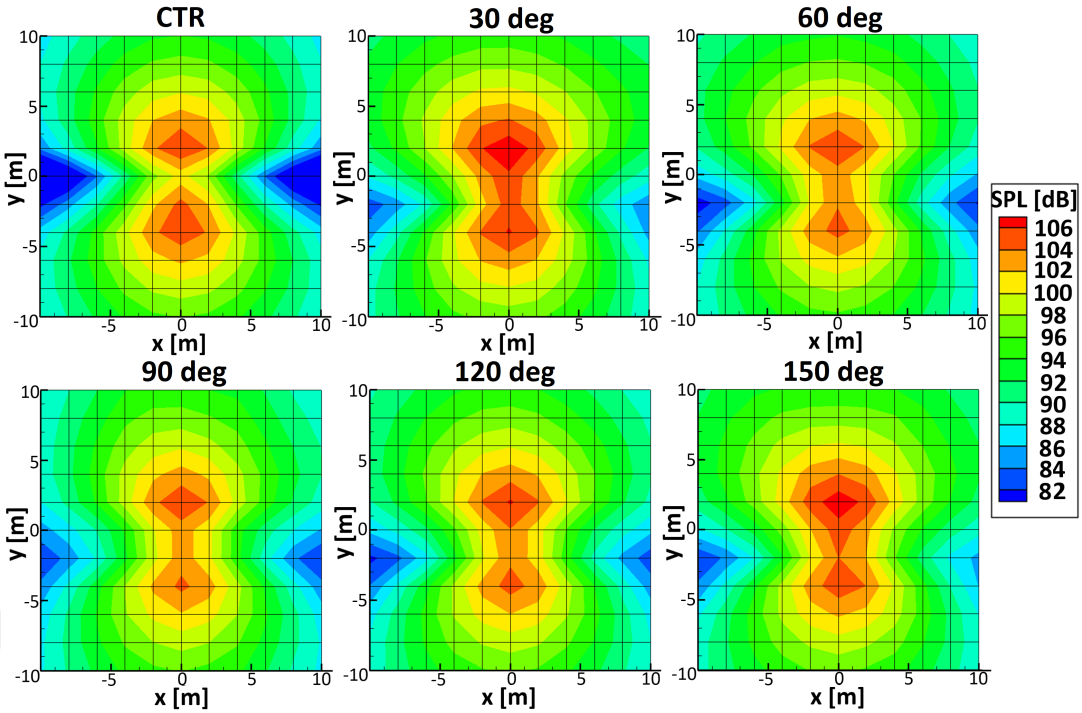

Figure 4.50: Loading noise SPL on horizontal plane at hover condition

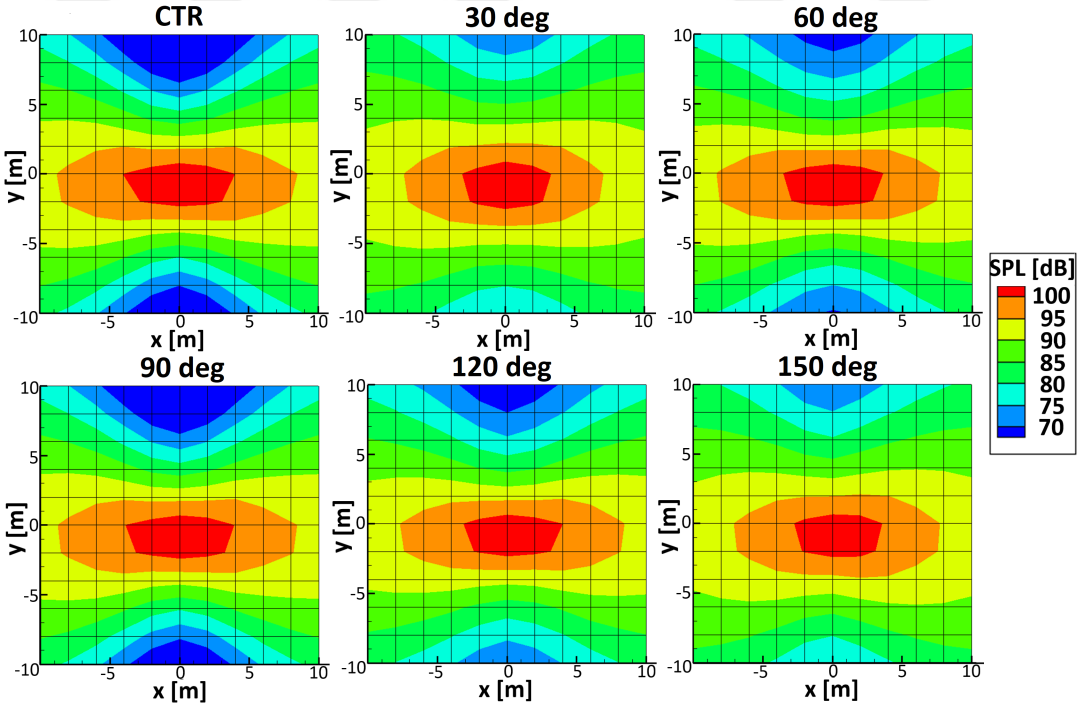

Figure 4.51: Thickness noise SPL on horizontal plane at hover condition

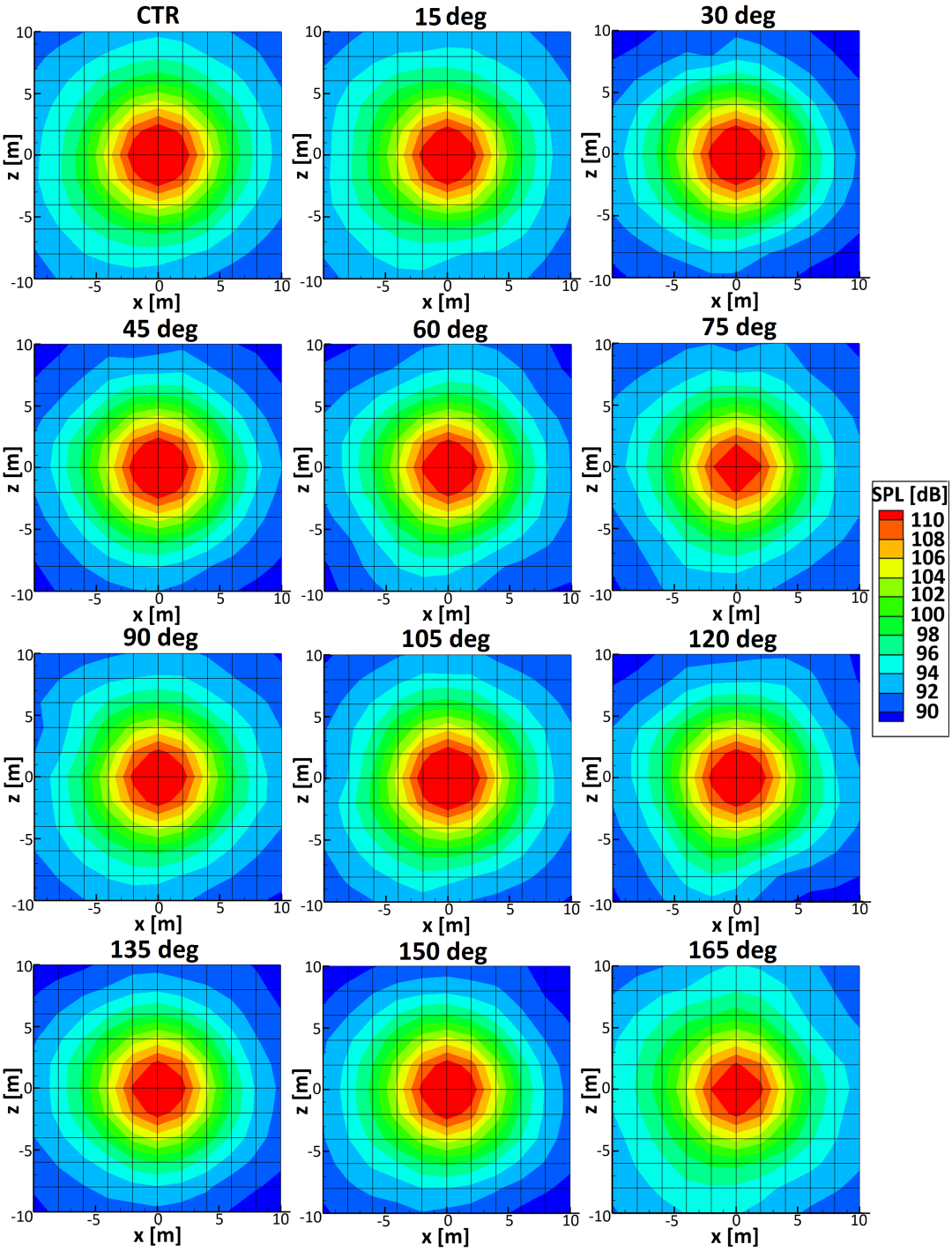

Figure 4.52: Total noise SPL on vertical plane at hover condition

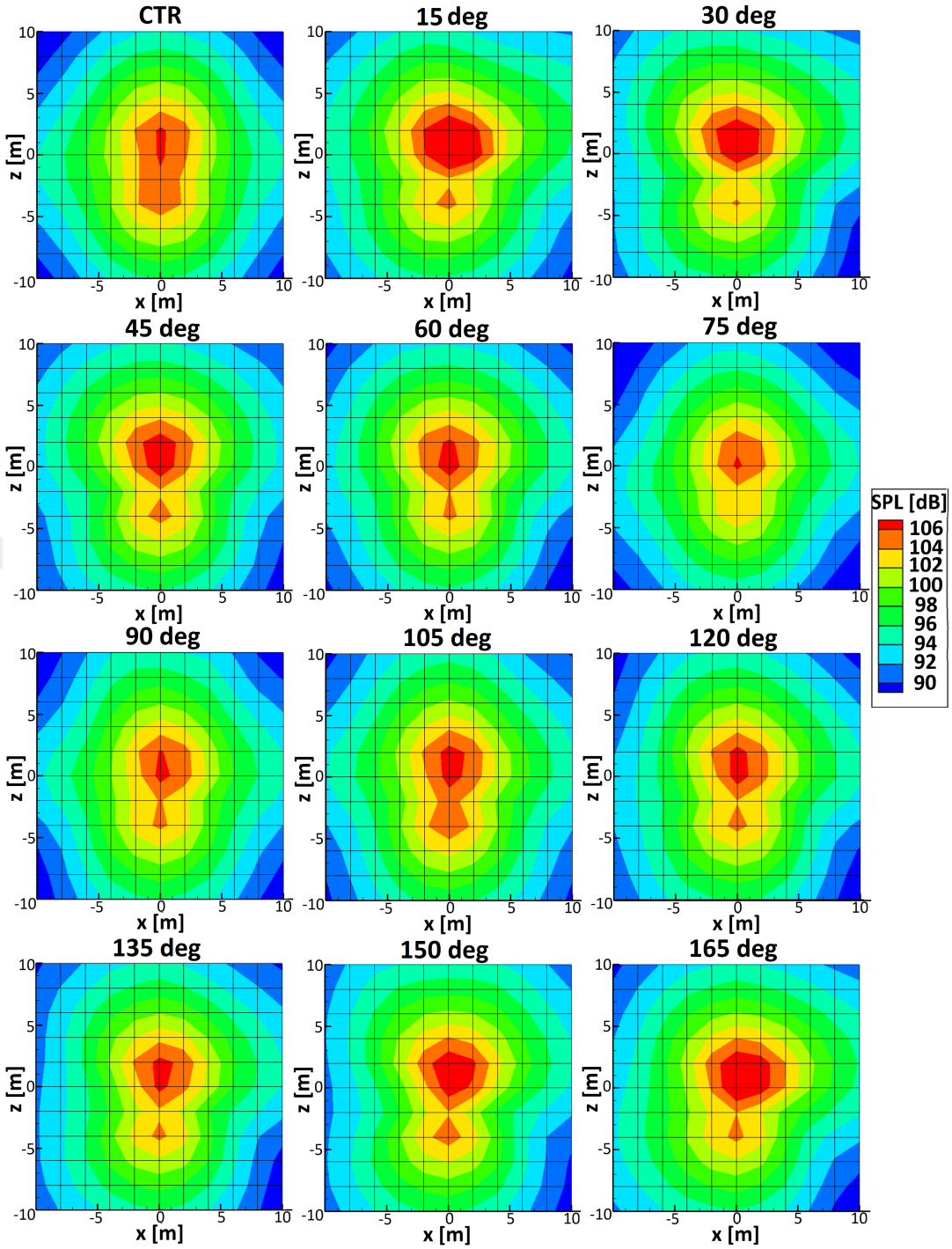

Figure 4.53: Total noise SPL on horizontal plane at hover condition

Quartering flight condition is investigated and depicted from Figures 4.54 to 4.58. Loading noise on vertical plane has an aeroacoustic signature with decreasing trend towards 90 degree scissors angle. This result is similar to result of oscillatory thrust. Thickness noise is directly influenced by the change of scissors angle. Level of the noise is same for all configurations, but distribution differs. Loading noise on horizontal plane is significantly affected by the scissors angle. At this flight condition, upper rotor leading configurations are superior to lower rotor leading configuration on horizontal plane. However, no effective change is observed for total noise on horizontal plane due dominance of thickness noise on horizontal plane.

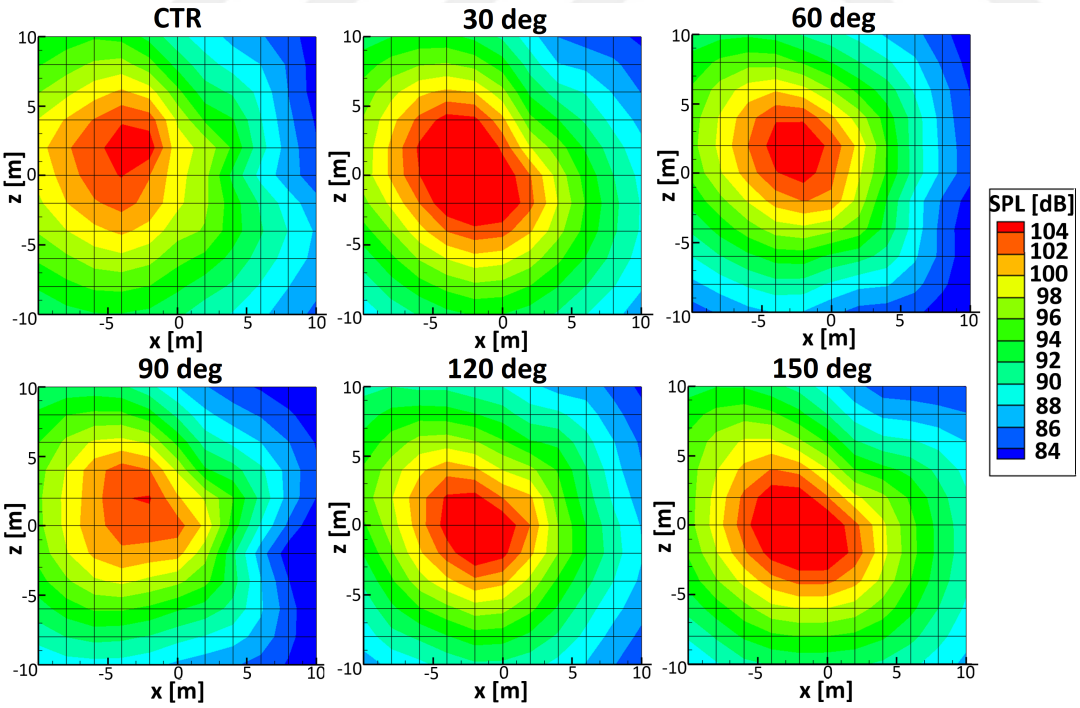

Figure 4.54: Loading noise SPL on vertical plane at quartering flight condition

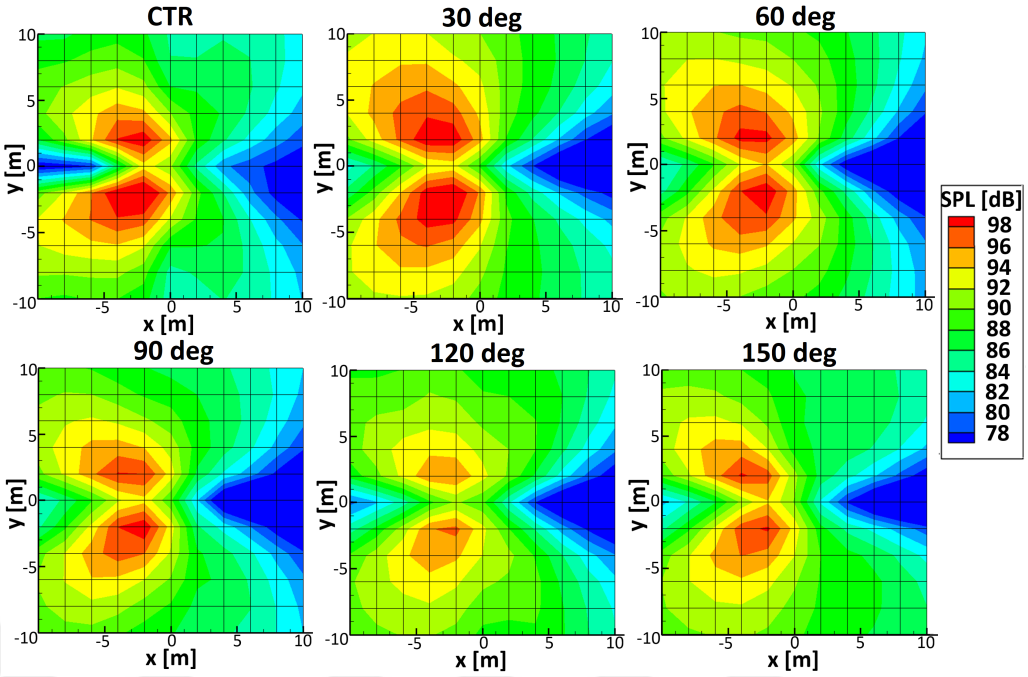

Figure 4.55: Loading noise SPL on horizontal plane at quartering flight condition

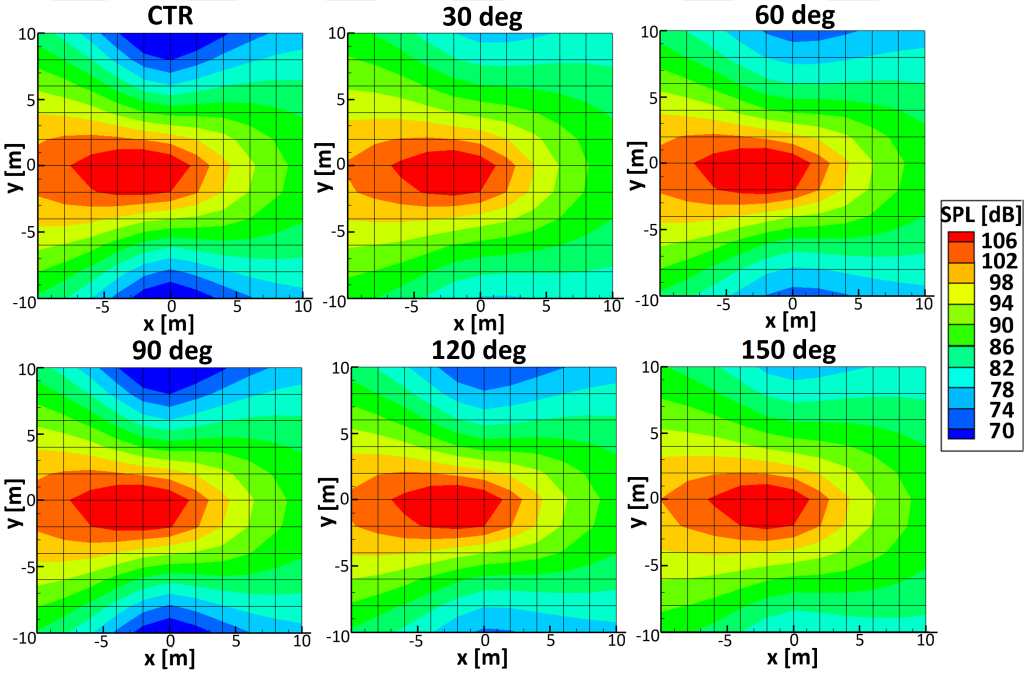

Figure 4.56: Thickness noise SPL on horizontal plane at quartering flight condition

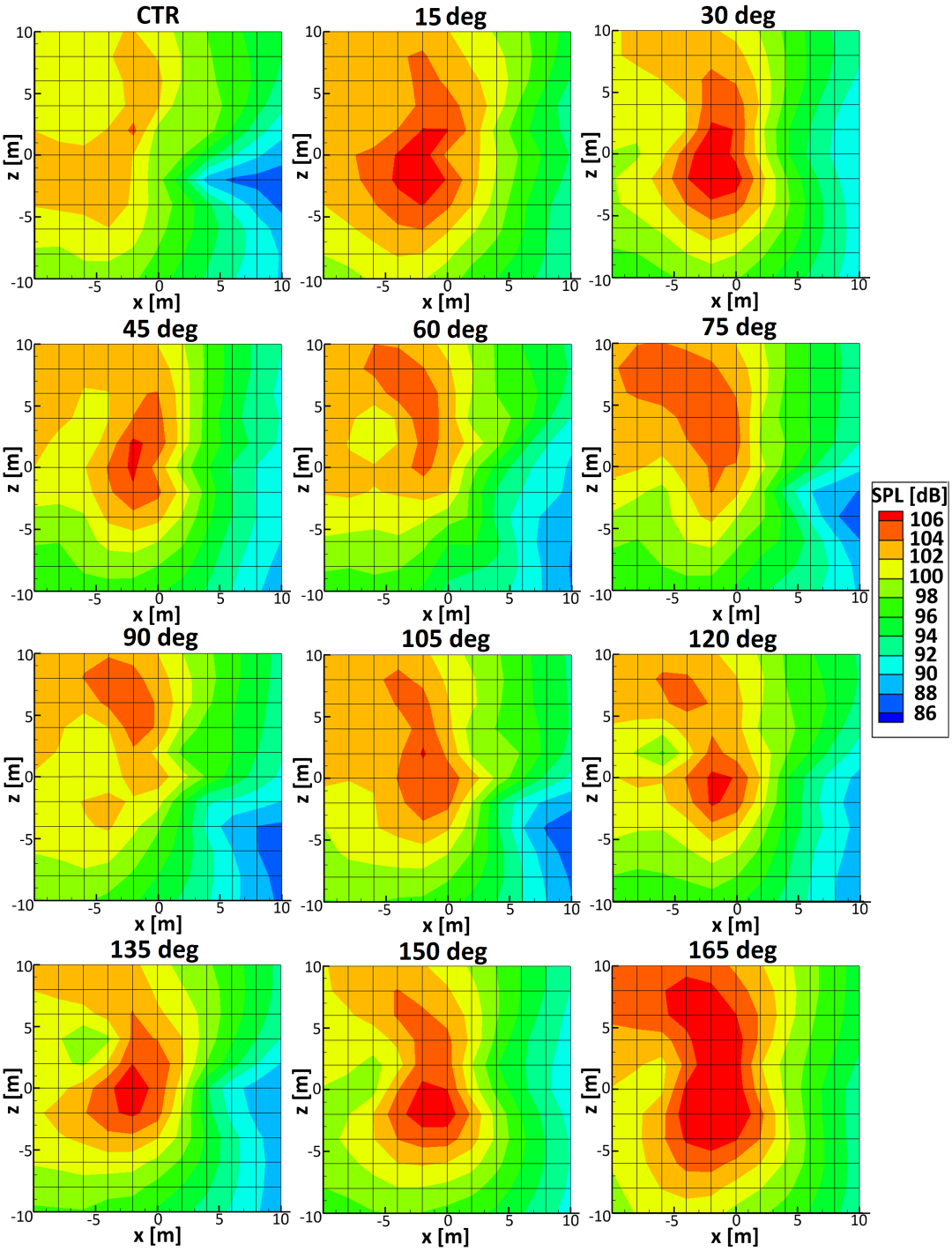

Figure 4.57: Total noise SPL on vertical plane at quartering flight condition

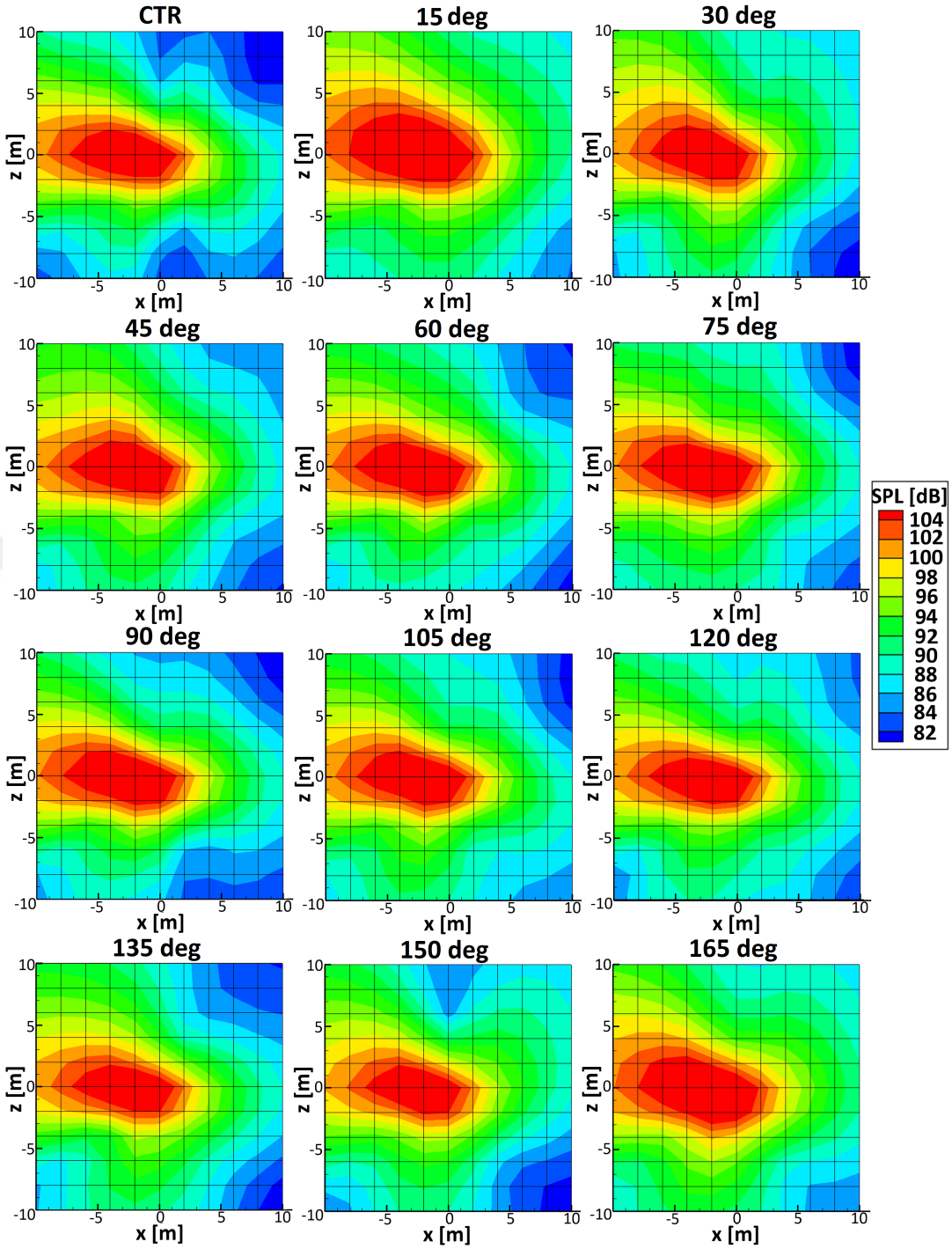

Figure 4.58: Total noise SPL on horizontal plane at quartering flight condition

CHAPTER 5

CONCLUSION

In this study, an aerodynamic model is implemented and validated to use in CHARM by available power data and sectional airloads. Furthermore, the coupling between CHARM and TACO is developed and implemented to use a comprehensive analysis approach while predicting rotor noises. Reconstructed sectional airloads, rotor thrust, and acoustic pressure are compared with HART-II test case at the validation of this methodology.

Firstly, a conventional tail rotor is investigated while the absence and existence of main rotor with bottom-forward and top-forward rotation direction to show how the tail rotor interfaces by the configurations. Observations of investigation on the conventional tail rotor are summarized;

- Main rotor interaction and rotation direction have no significant effects on integrated aerodynamic performance at hover condition.
- Main rotor interaction decreases the required power of the tail rotor due to increase on local dynamic pressure at forward and quartering flight conditions.
- Main rotor wake influence increases blade-vortex interactions on tail rotor for forward and quartering flight conditions, and there is no significant oscillations are observed at hover condition at conventional tail rotor configurations.
- Loading, thickness and total noises are affected by the rotation direction.
- Main rotor influence on tail rotor does not affect the thickness noise due to

rigid blade modeling of tail rotor. However, it affects the loading noise due to aerodynamic interference at forward and quartering flight conditions.

- Bottom-forward rotor configuration generates more noise than top-forward rotor configuration at forward and quartering flight conditions due to position of advancing side.
- There are no significant differences at hover condition for acoustic evaluation.

After evaluating the conventional tail rotor, the scissors tail rotor with 90 degree scissors angle is investigated for different vertical distances at the bottom-forward rotation direction with a full helicopter model to add the main rotor influence. Observations of investigation on vertical distance are summarized;

- Vertical distance does not change required power for forward flight, hover and quartering flight conditions, considerably.
- Increasing vertical distance has a direct influence on oscillatory thrust, decreasing trend at forward flight and hover, increasing trend at quartering flight.
- Vertical distance has no significant effects at hover condition on aeroacoustic behavior.
- Increasing vertical distance enhances the aeroacoustic signature at forward flight due to decreasing blade-vortex interactions. Contrary effects are observed at quartering flight due to increasing blade-vortex interactions.

Finally, the second design parameter of the scissors tail rotor is evaluated, which is the scissors angle. Observations of investigation on various scissors angle are summarized;

- Integrated aerodynamic performance slightly affected by scissors angle. However, lower rotor leading configurations have better performance than upper rotor leading configurations at hover condition.

- Scissors tail rotor aerodynamic behavior is directly related with the scissors angle at forward flight, hover and quartering flight conditions.
- Oscillatory thrust is highly affected by the scissors angle for flight conditions. Peak-to-peak thrust values increase when scissors angle moves away from 90 degree at forward and quartering flight conditions.
- Scissors angle changes the frequency of the generated acoustic pressure. Smaller angle between two rotors give a behavior of two-bladed tail rotor. Scissors angle causes modulated effect and directly affects characteristic of the noise.
- Best acoustic signature of the scissors tail rotor differs from flight condition to flight condition. There may exist an optimal scissors angle between 30 degree and 75 degree for flight conditions on horizontal plane.

Different scissors tail rotor configurations offer lower noise level than conventional tail rotor for analyzed flight conditions. Therefore, the scissors angle might be optimized due to type and usage spectrum of the helicopter using proposed coupling methodology.

The current implementation of the methodology covers only a few flight conditions and few configurations. The developed approach might be used in the following cases;

- A design optimization might be implemented with extra flight conditions and extra scissors tail rotor configurations.
- An adaptive scissors angle might be investigated.
- Two different twist angles might be given to two rotors, and performance and noise characteristic might be evaluated.

REFERENCES

[1] W. Wiesner and G. Kohler, "Tail rotor design guide," tech. rep., BOEING VERTOL CO PHILADELPHIA PA, 1974.

[2] W. Johnson, *Rotorcraft aeromechanics*, vol. 36. Cambridge University Press, 2013.

[3] G. J. Leishman, *Principles of helicopter aerodynamics with CD extra*. Cambridge university press, 2006.

[4] A. Ellin, *An in-flight experimental investigation of helicopter main rotor/tail rotor interactions*. PhD thesis, University of Glasgow, 1993.

[5] B. Edwards, C. Cox, and E. R. Booth Jr, "Revolutionary concepts for helicopter noise reduction: Silent program," tech. rep., NASA Langley Research Center, 2002.

[6] M. Mosher and R. PETERSON, "Acoustic measurements of a full-scale coaxial helicopter," in *8th Aeroacoustics Conference*, p. 722, 1983.

[7] N. L. Schatzman, "Aerodynamics and aeroacoustic sources of a coaxial rotor," tech. rep., NATIONAL AERONAUTICS AND SPACE ADMINISTRATION MOFFETT FIELD CA AMES RESEARCH CENTER, 2018.

[8] D. A. Wachspress and T. R. Quackenbush, "Impact of rotor design on coaxial rotor performance, wake geometry and noise," in *ANNUAL FORUM PROCEEDINGS-AMERICAN HELICOPTER SOCIETY*, p. 41, AMERICAN HELICOPTER SOCIETY, INC, 2006.

[9] J. Davidson, C. Havey, and H. Sherrieb, "Fan-in-fin antitorque concept study," tech. rep., VOUGHT HELICOPTER INC DALLAS TX, 1972.

[10] J. Yin, A. Dummel, D. Falchero, M. Pidd, J. Prospathoulous, A. Visingardi, and S. G. Voutsinas, "Analysis of tail rotor noise reduction benefits using

helinovi aeroacoutics main/tail rotor test and post-test prediction results," 2006.

[11] T. M. Fletcher, K. Duraisamy, and R. E. Brown, "Aeroacoustic analysis of main rotor and tail rotor interaction," 2008.

[12] J. Yin, B. G. van der Wall, and S. Oerlemans, "Representative test results from helinovi aeroacoustic main rotor/tail rotor/fuselage test in dnw," 2005.

[13] M. M. Atalay, A. Yücekayalı, M. Şenipek, and Y. Özyörük, "Main rotor - tail rotor interactional noise," in *8th Asian/Australian Rotorcraft Forum*, (Ankara), 2019.

[14] A. R. George and S.-T. Chou, "A comparative study of tail rotor noise mechanisms," *Journal of the American Helicopter Society*, vol. 31, no. 4, pp. 36–42, 1986.

[15] E. Greenwood and F. H. Schmitz, "Separation of main and tail rotor noise from ground-based acoustic measurements," *Journal of Aircraft*, vol. 51, no. 2, pp. 464–472, 2014.

[16] K. B. Amer and R. W. Prouty, "Technology advances in the ah-64 apache advanced attack helicopter," in *American Helicopter Society, Annual Forum, 39 th, St. Louis, MO, Proceedings*, 1983.

[17] M. G. Rozhdestvensky, "Scissors rotor concept- new results obtained," in *AHS, Annual Forum, 52 nd, Washington, DC*, pp. 1231–1241, 1996.

[18] G. H. Xu, "An experimental and analytical investigation of scissors rotor aerodynamics in hover," in *60th Annual Forum Proceedings - American Helicopter Society*, vol. 1, pp. 54–62, 2004.

[19] G.-H. Xu, S.-C. Wang, and J.-G. Zhao, "Effects of the scissors configuration on rotor aerodynamic characteristics," in *27th European Rotorcraft Forum*, (Moscow), 2001.

[20] G.-H. Xu, Q.-J. Zhao, and Y.-H. Peng, "Study on the induced velocity and noise characteristics of a scissors rotor," *Journal of aircraft*, vol. 44, no. 3, pp. 806–811, 2007.

[21] F. Fan, Y. J. Shi, G. H. Xu, and Z. Ye, "Analysis on aerodynamic and acoustic characteristics for scissors tail-rotors in forward flight," in *American Helicopter Society International - 2nd Asian/Australian Rotorcraft Forum, ARF 2013 and the 4th International Basic Research Conference on Rotorcraft Technology 2013, IBRCRT 2013*, pp. 105–117, 2013.

[22] Z. Zhu and Q. Zhao, "Numerical analyses for aerodynamic and noise characteristics of helicopter scissors tail rotor," in *Pro-ceedings of the 70th Annual Forum of ttle American Hell-copter Society, Quebec, Canada*, vol. 1, pp. 1186–1198, 2014.

[23] M. Xiao-wei, S. Yong-jie, and X. Guo-hua, "An Analytical Investigation on Helicopter Scissors Tail-rotor Aeroacoustics in Hover and Forward Flight," in *4th Asian/Australian Rotorcraft Forum*, 2015.

[24] D. A. Wachspress, T. R. Quackenbush, and A. H. Boschitsch, "First-principles free-vortex wake analysis for helicopters and tiltrotors," in *59th ANNUAL FORUM PROCEEDINGS-AMERICAN HELICOPTER SOCIETY*, AMERICAN HELICOPTER SOCIETY, INC, 2003.

[25] D. A. Wachspress, T. R. Quackenbush, and A. H. Boschitsch, "Rotorcraft interactional aerodynamics with fast vortex/fast panel methods," *Journal of the American Helicopter Society*, vol. 48, no. 4, pp. 223–235, 2003.

[26] U. Saetti, "Rotorcraft simulations with coupled flight dynamics, free wake, and acoustics," Master's thesis, The Pennsylvania State University, 8 2016.

[27] W. Villafana, "Rotorcraft noise abatement procedures development," Master's thesis, The Pennsylvania State University, 12 2016.

[28] E. W. Quon, M. J. Smith, G. R. Whitehouse, and D. Wachspress, "Unsteady reynolds-averaged navier-stokes-based hybrid methodologies for rotor-fuselage interaction," *Journal of aircraft*, vol. 49, no. 3, pp. 961–965, 2012.

[29] A. Yücekayalı, M. Şenipek, Y. Ortakaya, and Y. Özyörük, "Taco: Helicopter noise predictions," in *7th Asian/Australian Rotorcraft Forum*, (Jeju Island), 2018.

[30] M. Şenipek, A. Yücekayalı, Y. Ortakaya, and Y. Özyörük, "Comprehensive rotorcraft aeroacoustics: Investigtion of surface pressure distribution methods for rotor noise," in *45th European Rotorcraft Forum*, (Warsaw), 2019.

[31] Y. Li, "Tools for development and analysis of rotorcraft noise abatement," Master's thesis, The Pennsylvania State University, 2015.

[32] T. R. Quackenbush, D. B. Bliss, D. A. Wachspress, A. H. Boschitsch, and K. Chua, "Computation of rotor aerodynamic loads in forward flight using a full-span free wake analysis," tech. rep., National Aeronautics and Space Administration, 1990.

[33] T. R. Quackenbush, C.-M. G. Lam, D. A. Wachspress, and D. B. Bliss, "Computational analysis of high resolution unsteady airloads for rotor aeroacoustics," *National Aeronautics and Space Administration*, 1994.

[34] B. G. van der Wall and C. L. Burley, "2nd hhc aeroacoustic rotor test (hart ii)-part i: Test documentation," tech. rep., German Aerospace Center Institute, 2003.

[35] P. M. Shinoda, "Full-scale s-76 rotor performance and loads at low speeds in the nasa ames 80-by 120-foot wind tunnel. volume 1.," tech. rep., NATIONAL AERONAUTICS AND SPACE ADMINISTRATION MOFFETT FIELD CA AMES RESEARCH CENTER, 1996.

[36] D. Jepson, R. Moffitt, K. Hilinger, and J. Bissel, "Analysis and correlation of test data from an advanced technology rotor system," tech. rep., NATIONAL AERONAUTICS AND SPACE ADMINISTRATION CR 3714, 1983.

[37] L. Horace, "Hydrodynamics," 1932.

[38] G. H. Vatistas, V. Kozel, and W. Mih, "A simpler model for concentrated vortices," *Experiments in Fluids*, vol. 11, no. 1, pp. 73–76, 1991.

[39] M. Scully, *Computation of helicopter rotor wake geometry and its influence on rotor harmonic airloads*. PhD thesis, Massachusetts Institute of Technology, 1975.

[40] G. Vatistas, S. Lin, and C. Kwok, "Theoretical and experimental studies on vortex chamber flows," *AIAA journal*, vol. 24, no. 4, pp. 635–642, 1986.

[41] Anonymous, *Technical Manual Operator's Manual for Army AH64D Helicopter. U.S. Army TM 1-1520-251-10.* U.S. Army Headquarters, 2002.

[42] R. JanakiRam, R. Smith, B. Charles, and A. Hassan, "Aerodynamic design of a new affordable main rotor for apache helicopter," in *ANNUAL FORUM PROCEEDINGS-AMERICAN HELICOPTER SOCIETY*, vol. 59, pp. 526–542, AMERICAN HELICOPTER SOCIETY, INC, 2003.

[43] M. H. Mansur, "Development and validation of a blade-element mathematical model for the ah-64a apache helicopter," tech. rep., National Aeronautics and Space Administration, 1995.

[44] T. R. Norman, P. Shinoda, R. L. Peterson, and A. Datta, "Full-scale wind tunnel test of the uh-60a airloads rotor," in *The American Helicopter Society 67th Annual Forum*, 2011.

[45] E. M. Lee-Rausch and R. T. Biedron, "Fun3d airloads predictions for the full-scale uh-60a airloads rotor in a wind tunnel," *Journal of the American Helicopter Society*, vol. 59, no. 3, pp. 1–19, 2014.

[46] H. Yeo and E. A. Romander, "Loads correlation of a full-scale uh-60a airloads rotor in a wind tunnel," *Journal of the American Helicopter Society*, vol. 58, no. 2, pp. 1–18, 2013.

[47] Y. Ozyoruk, A. Unal, and A. O. Yuksel, "Noise predictions of helicopter rotors in hover and forward flight," in *23rd AIAA/CEAS Aeroacoustics Conference*, p. 3529, 2017.

[48] B. G. van der Wall and C. L. Burley, "2nd hhc aeroacoustic rotor test (hart ii)-part ii: Representative results," tech. rep., German Aerospace Center Institute, 2005.

[49] J. Lim, M. Smith, S. Jung, J. Bailly, J. Baeder, D. Boyd Jr, and B. van der Wall, "An assessment of comprehensive code prediction state-of the-art using the hart ii international workshop data," in *Proceedings of the American Helicopter Society 68th Annual Forum Technology Display*, 2012.

[50] H. Heller, H. Buchholz, K. Schultz, S. Ahmed, and W. Splettstoesser, "Helicopter rotor blade aeroacoustics: A comparison of model-scale wind tunnel with full-scale flight test results," in *ICAS PROCEEDINGS*, vol. 20, pp. 1741–1757, 1996.

[51] K. S. Brentner and F. Farassat, "Modeling aerodynamically generated sound of helicopter rotors," *Progress in Aerospace Sciences*, vol. 39, no. 2-3, pp. 83–120, 2003.

[52] J. A. Pritchard and D. L. Kunz, "A redesigned tail rotor for improvement of ch-53e high-altitude performance," *Journal of the American Helicopter Society*, vol. 51, no. 3, pp. 266–274, 2006.

[53] K. Brentner, B. Edwards, R. Riley, and J. Schillings, "Predicted noise for a main rotor with modulated blade spacing(helicopter noise)," in *AHS International, 58 th Annual Forum Proceedings-*, vol. 2, pp. 1563–1572, 2002.